Charge Transfer and Photovoltaics with Inorganic Semiconductor Nanoparticles

by

Yang Wang

B. S., Renmin University of China, 2008

Submitted to the Graduate Faculty of the
Dietrich School of Arts and Sciences in partial fulfillment
of the requirements for the degree of
Doctor of Philosophy

University of Pittsburgh
2014

UNIVERSITY OF PITTSBURGH

Dietrich School of Arts and Sciences

This dissertation was presented

by

Yang Wang

It was defended on

October 22, 2013

and approved by

Dr. Geoffrey Hutchison, Assistant Professor, Department of Chemistry

Dr. Jung-kun Lee, Associate Professor, Departmental of Mechanical Engineering and Materials Science

Dr. Alexander Star, Associate Professor, Department of Chemistry

Dissertation Advisor: Dr. David Waldeck, Professor, Department of Chemistry

Charge Transfer and Photovoltaics with Inorganic Semiconductor Nanoparticles

Yang Wang, PhD

University of Pittsburgh, 2014

Charge Transfer and Photovoltaics with Inorganic Semiconductor Nanoparticles

Yang Wang, PhD

University of Pittsburgh, 2014

Colloidal semiconductor nanoparticles (NP) are emerging as a new class of solution-processable materials for low-cost, flexible, thin-film photovoltaic devices. The NP quantum size effect allows researchers to selectively tune the NP's absorption coverage across a broad range of the solar spectrum. Recent advances have led to a power conversion efficiency of 7% for NP-based solar cells. However, exciton generation, separation, and recombination processes in these devices are not well-understood, which largely limit further improvement of the efficiency. Thus, this dissertation studies the underlying processes that control the kinetics for photogenerated charges in the NP-based devices. The first work in this dissertation addresses how the size-tunable energetics of the NPs change once they are electronically coupled with a conductive substrate. The second study focuses on the energy architecture and alignment for the NP with respect to the energy levels of electron and hole transporting media. The third study explores the donor-acceptor interfacial charge transfer between a conjugated copolymer and a NP with the goal of driving efficient charge separation for inorganic/organic hybrid solar cells. The last study investigates the effect of thermal annealing on the photovoltaic performance for PbS NP/TiO_2 depleted heterojunction solar cells. The findings in these studies provide a deeper understanding of charge transfer kinetics for the NP, and may facilitate the development of the NP-based photovoltaics for use in next generation solar cells.

TABLE OF CONTENTS

LIST OF TABLES

LIST OF FIGURES

LIST OF SCHEMES

Dedication

This dissertation is dedicated to the important people in my life:

My parents: Thank you so much for all of your love and support. I am sorry I have been so far away from home, but I miss you every day.

My wife: Shuying, you mean the world to me. Thanks for always believing in me and encouraging me to do my best.

Acknowledgement

I feel truly grateful to many people who help me achieve my professional goals.

Professor David Waldeck has been a wonderful advisor. Thanks for the guidance, support, and opportunities he has given me. I have enjoyed the five years I spent in his research group. I am also grateful to current and former labmates of mine, including Prof. Prasun Mukherjee, Prof. Kuan Liu, Prof. Kathryn Davis, Dr. Emil Wierzbinski, Dr. Matthew Kofke, Dr. Mingyan Wu, Dr. Lei Wang, Daniel Lamont, Xing Yin, Brian Bloom, Robin Sloan, Madu Mendis, Hao Lu, Brittney Graff, Liubin Zhao, and Miles Batson.

Thanks to all the collaborators I have worked with, including Professor Ron Naaman and his group (Weizmann Institute, Israel), Professor Jung-Kun Lee and his group (Pitt), Professor Nathaniel Rosi and his group (Pitt), and Professor Prashant Kamat and his group (University of Notre Dame).

I thank my dissertation committee members, including Professor Geoffrey Hutchison, Professor Jung-Kun Lee, Professor Alex Star, and Professor David Waldeck. I appreciate their help throughout my graduate school process.

I also feel grateful for the instrumental training and help I received from Peterson Institute for Nanoscience and Engineering. And I thank all the staff in the chemistry department. Lastly, I would like to thank US Department of Energy for funding my research for the past 5 years.

1.0 INTRODUCTION

Inorganic semiconductor nanoparticles (NPs) are a new class of semiconductor materials with nanoscale dimensions (2-10 nm in diameter), that exhibit a wide range of size-dependent properties.[1] Recent advances in our experimental and theoretical understanding of their properties have allowed rapid developments in NP-based electronic and optoelectronic devices.[2] Compared to inorganic bulk semiconductors, the bandgap of the semiconductor NPs can be simply tuned by varying the NP size in synthesis. This feature allows the use of a single material with different bandgaps to harvest a broad range of the solar spectrum. In addition, semiconductor NPs can be synthesized and crystallized in solution at a low temperature. Hence, they are compatible with the solution-processing technologies, which makes the inexpensive roll-to-roll production possible for the NP-based devices.[3] Also because of the solution-processibility, NPs can be integrated into different types of devices, such as p-n junction solar cells, bulk heterojunction solar cells, or NP-sensitized solar cells.

The extinction coefficients of the NPs at the bandgap transition range from 10^4 to 10^6 M^{-1} cm^{-1}, up to 100 times larger than that for ruthenium(II) tris(bipyridine) dyes used in most dye-sensitized solar cells.[4] Furthermore, NPs are more photostable than organic chromophores with comparable extinction coefficients. For instance, when used as fluorescent labels for biological samples, CdSe/ZnS core/shell NPs maintained their quantum yield under continuous UV irradiation up to 4000 times longer than a fluorescein dye.[5]

Although significant challenges remain, semiconductor nanoparticles are a promising material for use in the next-generation solar cells,[6] because their unique features offer a simple and novel avenue for efficient thin-film photovoltaics and cost-effective solar electricity at the utility scale. This chapter starts by discussing the fundamental quantum theories and the synthesis of the semiconductor NPs, and it is followed by a review of recent progresses for the NP-based photovoltaic technologies. The next section addresses the current challenges and future outlooks for the NP-based photovoltaic application. This chapter ends by providing an outline of the scope and important findings in this dissertation.

1.1 QUANTUM CONFINEMENT EFFECT

Semiconductor NPs demonstrate size-dependent bandgaps and bandedges, which are normally termed as the quantum confinement effect. This effect can be semi-empirically modeled by the effective mass approximation (EMA):[7]

$$\Delta \mathrm{E}_{\mathrm{gap}} = \mathrm{E}_{\mathrm{gap}}^{\mathrm{NP}} - \mathrm{E}_{\mathrm{gap}}^{\mathrm{Bulk}} = \frac{h^2}{2d^2}\left[\frac{1}{m_e^*} + \frac{1}{m_h^*}\right] - \frac{3.6e^2}{4\pi\epsilon_0\epsilon_\infty d} \qquad \textbf{Equation 1}$$

in which $\Delta \mathrm{E}_{\mathrm{gap}}$ is the bandgap difference between the NP ($\mathrm{E}_{\mathrm{gap}}^{\mathrm{NP}}$) and the bulk semiconductor ($\mathrm{E}_{\mathrm{gap}}^{\mathrm{Bulk}}$), h is the Planck constant, d is the NP's diameter, m_e^* and m_h^* are the effective mass of the electron and hole, respectively, e is the electron charge, $\epsilon_0$and ϵ_∞ are dielectric constant of the vacuum and the semiconductor. Because the bandedge values for the bulk semiconductors are well-known, the EMA can also estimate those for the NPs by using Equation 2 and 3:

$$\mathrm{E}_{\mathrm{CBM}} = \mathrm{E}_{\mathrm{CBM}}^{\mathrm{Bulk}} + \Delta \mathrm{E}_{\mathrm{gap}}\left[\frac{m_h^*}{m_h^* + m_e^*}\right] \qquad \textbf{Equation 2}$$

$$\mathrm{E_{VBM}} = \mathrm{E_{VBM}^{Bulk}} + \Delta\mathrm{E_{gap}}\left[\frac{m_e^*}{m_h^* + m_e^*}\right] \qquad \textbf{Equation 3}$$

in which, VBM and CBM stand for the valence band maximum and conduction band minimum. Figure 1.1 shows the EMA results for various sizes of CdSe and CdTe NPs. It demonstrates the quantum confinement effect, namely, 1) the bandgaps and bandedges (VBM and CBM) of the NPs are strongly size-dependent; and 2) they gradually approach the bulk values as the NP size increases.

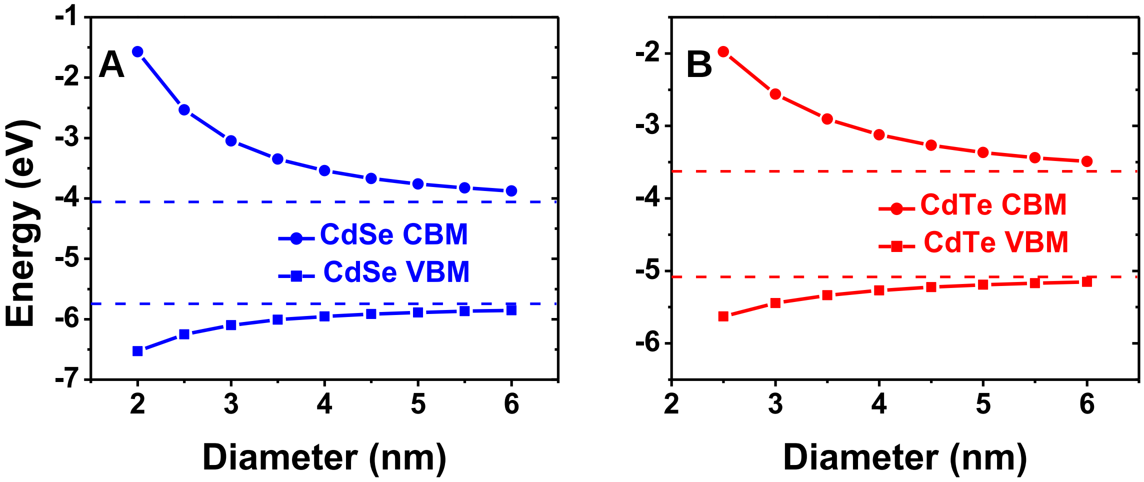

Figure 1-1. Panels A and B show the CBM and VBM values for CdSe and CdTe NPs that the thesis author calculated by using EMA. The dash lines indicate the bulk CBM and VBM values. For CdSe, $\mathrm{E_{gap}^{Bulk}} = 1.74$ eV, $m_e^* = 0.13$, and $m_h^* = 0.44$, and $\epsilon_\infty = 4.86$. For CdTe, $\mathrm{E_{gap}^{Bulk}} = 1.44$ eV, $m_e^* = 0.11$, $m_h^* = 0.35$, and $\epsilon_\infty = 10.20$.

1.2 SYNTHESIS OF SEMICONDUCTOR NANOPARTICLES

The quantum confinement effect can be demonstrated in experiment by synthesizing NPs with different sizes and monitoring their spectroscopic features. The wet synthesis is one of the important advantages for the semiconductor NPs.[1] After years of development for the precursors, surface ligands, solvents, reaction mechanisms, etc.,[8] researchers now are able to easily and precisely control NP synthesis. Recently, an automated NP synthesis robot has become commercially available, which is a key step towards cheap and large-scale production for NP-based devices.[9] To date, multiple different types of semiconductor materials, including II-VI group (CdS, CdSe, CdTe), III-V group (InP, InAs), IV-VI group (PbS, PbSe, PbTe), and so on,[10] have been synthesized into nanoparticle form.

1.2.1 Standard synthetic protocol

In this dissertation, the hot-injection method is primarily used for synthesizing semiconductor NPs.[11] Typically for the synthesis of CdTe NPs, the cadmium precursor is prepared by decomposing CdO powder in a solvent (such as octadecene (ODE)) with surface capping ligands (e.g., alkylphosphonic acid or oleic acid) at 300 °C. The tellurium precursor is normally prepared by dissolving elemental tellurium powders in trioctylphosphine (TOP). Then, the tellurium precursor is injected into the cadmium precursor at 300 °C to start the NP nucleation. The size of the NP is primarily controlled by the precursor concentration, reaction temperature, and the growth time. After reaching the desired size, the reaction is quenched by removing the heating mantle. The NP synthesis can also be carried out in the aqueous phase by using water-soluble precursors (e.g., $CdCl_2$ and NaHTe) and ligands, such as 3-mercaptopropionic acid.[12]

Figure 1.2 shows the steady-state absorbance and photoluminescence spectra for the CdTe NPs synthesized in ODE by following the above procedure. The red-shifting of the spectra as the time grows demonstrates the size evolution for the CdTe NPs; namely, the quantum confinement effect.

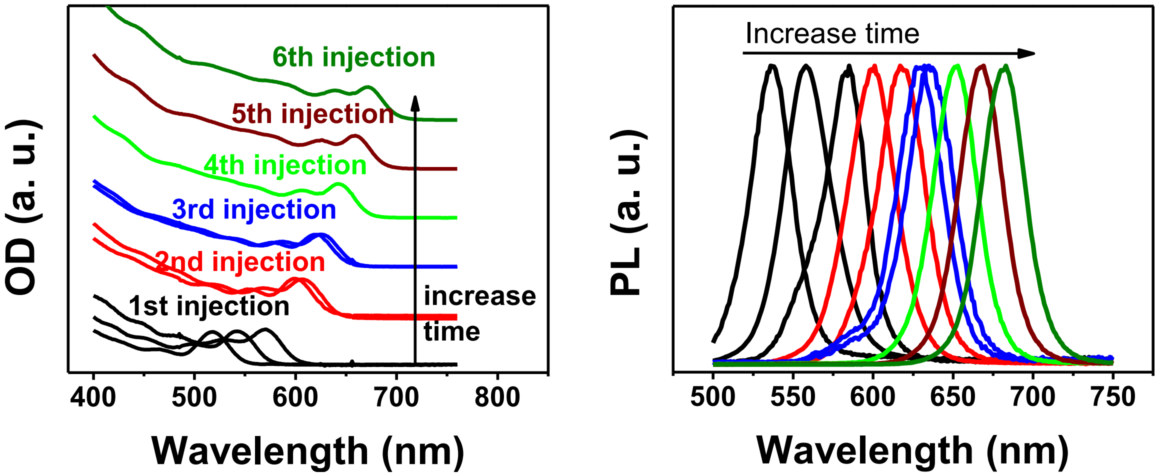

Figure 1-2. Panels A and B show that the absorbance (OD) and photoluminescence (PL) spectra of CdTe NPs.

Because of the size-tunable energetics of the NP, researchers are able to optimize the energy alignment in devices by tuning the energy offsets between the NP and the electrode. This feature can be used to achieve an optimal charge separation driving force, while maintaining efficient light harvesting. For example, Kamat et al[13] have reported for a CdSe-NP-sensitized TiO_2 solar cell that different electron transfer rates can be obtained by using NPs with different sizes, because varying the NP size also changes the CBM energy offset between the NP and the TiO_2 layer, namely, the electron transfer driving force.

1.2.2 Shape-controlled NP synthesis

The shape of the NP can also be controlled by carefully selecting surface ligands, precursor concentration, and precursor/ligand molar ratio.[10e,14] Figure 1.3 shows that spherical CdSe NPs are formed by using oleic acid (OA) as the ligand at a low precursor concentration, while elongated nanostructures, such as rods, are prepared with tetradecylphosphonic acid (TDPA) as the ligand and a high precursor concentration. Alivisatos et al[10e,14] reported that the elongated

NPs are created because different NP facets have different surface energy, and the ones with higher surface energy tend to grow faster. Thus, the key for kinetic shape control is to use a facet-selective surface ligand, such as TDPA, that densely binds to the low-surface-energy facets while exposing the high-surface-energy facets and leading to anisotropic NP growth.

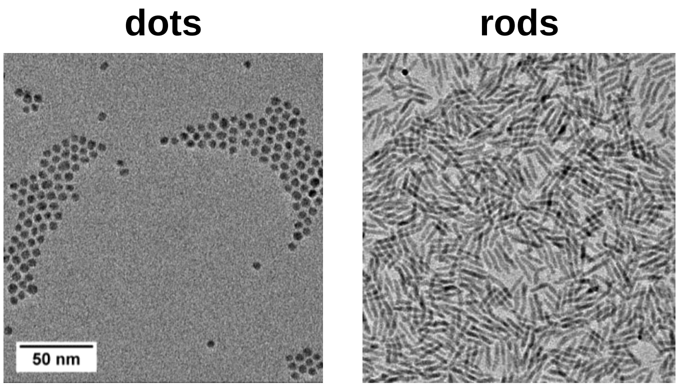

Figure 1-3. It shows two transmission electron microscopy (TEM) images for the CdSe NPs with different shapes.

1.2.3 Ligand exchange

Semiconductor NPs normally have an inorganic core that is stabilized by a layer of organic surface capping ligands. Ligand exchange can be used to modify and functionalize the NP surface in the post-synthesis stage without affecting the inorganic core. For instance, water-soluble and highly photoluminescent CdTe NPs can be prepared by replacing the initial fatty ligands (e.g., oleic acid (OA)) with water-soluble ligands, such as 3-mercaptopropionic acid (MPA). Figure 1.4 show the steady-state absorbance (solid lines) and photoluminescence (dash lines) spectra for hydrophobic OA-CdTe NPs (black), which are ligand-exchanged to hydrophilic MPA-CdTe NP (red) without significant changes of the NP size. In addition, this ligand exchange significantly enhances the quantum yield of the CdTe NPs, because thiol ligands are able to remove the surface trap states from the CdTe NP and thus enhance the radiative exciton recombination.[15] Similar ligand exchange methods have been used to make pyridine/thiophene capped NPs;[16] halide capped NP;[17] conjugated oligomer grafted NPs;[18] NPs with bio-compatible polymer coatings;[19] NPs with inorganic capping,[20] and even naked NPs.[21] Furthermore, the ligand exchange can also be carried out in the solid-state with NP thin films. Several group have used short bidentate linkers, such as 1,2-ethanedithiol[10h] or hydrazine,[22] to treat NP thin films. This treatment replaces the initial long insulating ligands on the NP surface, reduces the inter-NP distance, and enhances the photoconductivity of the NP films.

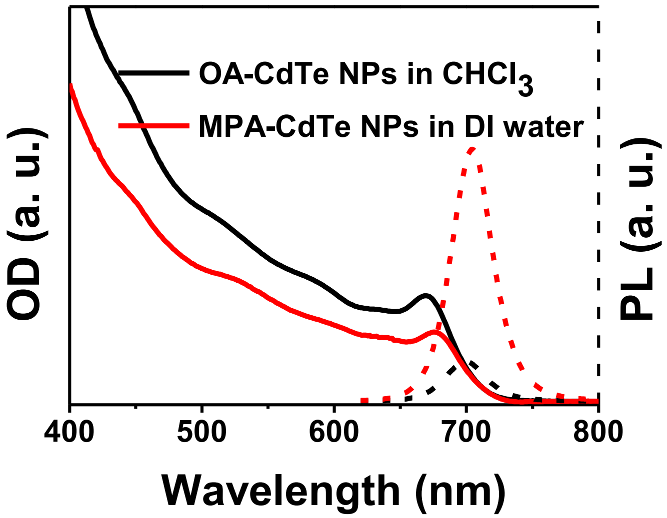

Figure 1-4. This plot compares the steady-state absorbance (OD, solid lines) and OD-corrected photoluminescence (dash lines) spectra for OA-CdTe NPs (black) in chloroform and MPA-CdTe NP (red) in DI water.

1.3 NP-BASED PHOTOVOLTAICS

As briefly mentioned above, semiconductor NPs have some unique photovoltaic properties that can be utilized to develop next-generation solar cells. First of all, the NP solutions or their hybrids with organic semiconductors are wet-processable and can be directly used as a photovoltaic ink to print large-scale, low-cost, and flexible thin film solar cells.[10g,23] Moreover, NPs with different sizes can be integrated into the same device to enhance light harvesting and solar energy conversion by employing a synergy of electron transfer and energy transfer from the small NP to the large one because of the energy cascade.[24] The large NP collectively concentrates and converts the solar energy into photo-generated carriers (electron and hole) that are further injected into the charge transport layers. Additionally, multiple exciton generation (MEG) or hot electron transfer is another important feature of semiconductor NPs that holds the promise for overcoming the Schockley-Queisser limit.[25] Recent studies for Pb-chalcogenide NPs have proven the feasibility of this concept by showing an external quantum efficiency larger than 100% at wavelengths below 400 nm.[26] This section will review the latest advances for several different types of NP-based photovoltaic devices, and also discuss their challenges and outlooks.

1.3.1 Hybrid organic/inorganic bulkheterojunction (BHJ) solar cells

Hybrid organic/inorganic bulkheterojunction (BHJ) solar cells, normally consisting of p-type conductive polymers (CP) and n-type semiconductor NPs, are a rapidly growing area for developing next-generation solar cells,[18,27] because they combine the complementary advantages of both CPs and NPs.[8,28] Figure 1.5 shows that hybrid BHJ cells normally have a PEDOT:PSS coated ITO electrode as the hole transport layer, on top of which a blended layer of NP and CP are spin-coated from their mixed solution. A shallow work function metal (e.g. Al) is then evaporated as the back contact for electron collection. Although the hybrid cells have a similar working principle as the organic BHJ cells, such as CP/C_{60} systems, using semiconductor NPs as the electron acceptor (instead of C_{60}) can enhance the light harvesting because of their high extinction coefficient and good absorption coverage in the solar spectrum. The NPs can also lower the exciton binding energy by providing a higher dielectric constant.[29] However, the power conversion efficiencies[30] (~ 5%) reported for organic/inorganic hybrid devices, such as P3HT/CdSe NP BHJ cells, are significantly lower than that for inorganic devices and organic devices. Such a low efficiency is believed to arise largely because of rapid charge recombination at the hybrid interface.[31] Thus, the challenge is to enhance the charge transfer and charge separation at the organic/inorganic donor-acceptor (D-A) heterojunction.[18,27]

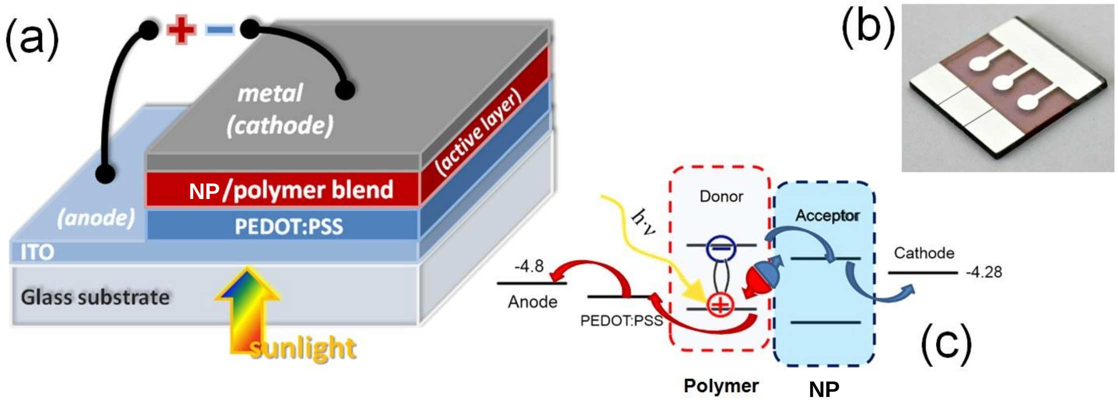

Figure 1-5. Panel (a) illustrates the general device structure for the hybrid BHJ solar cells. Panel (b) and Panel (c) shows a real device and an energy diagram for the device in Panel (a). Figures adapted from reference 32.[32]

1.3.2 NP-sensitized solar cells

Similar to dye-sensitized solar cells (DSCs),[33] semiconductor NP sensitized solar cells (NPSC) (Panel c in Figure 1.6) operate by a similar principle but replace organic dye molecules with NPs as the sensitizer. Most of the NPSC devices reported to date use cadmium chalcogenide NPs as the sensitizer.[6] Figure 1.6C shows that the NPSC generally has a NP-decorated TiO_2 layer on a fluorine-doped tin oxide electrode (FTO), an electrolyte with the hole scavenger redox couple (e.g., polysulfide), and a Pt-based counter electrode. Under illumination, an electron-hole pair is generated in the NP, which then separately injects the photogenerated electron and hole into the TiO_2 layer and the redox couple in the electrolytes. Recent development of NPSCs has increased their efficiency to above 5%,[34] which is still much lower than that (~ 14 %) of the DSCs.[35] Several groups[36] suggested that this difference is caused by the sluggish hole transfer at the NP/electrolyte interface, including the hole injection rate, the redox couple diffusion rate and regeneration rate, which leads to multiple charge recombination processes because of the back electron transfer. Thus, increasing the hole transfer rate is the key step to improve the efficiency for the NPSCs. Besides, the anodic corrosion of the NP by the electrolytes also plays a role in the overall performance of the NPSC.[37]

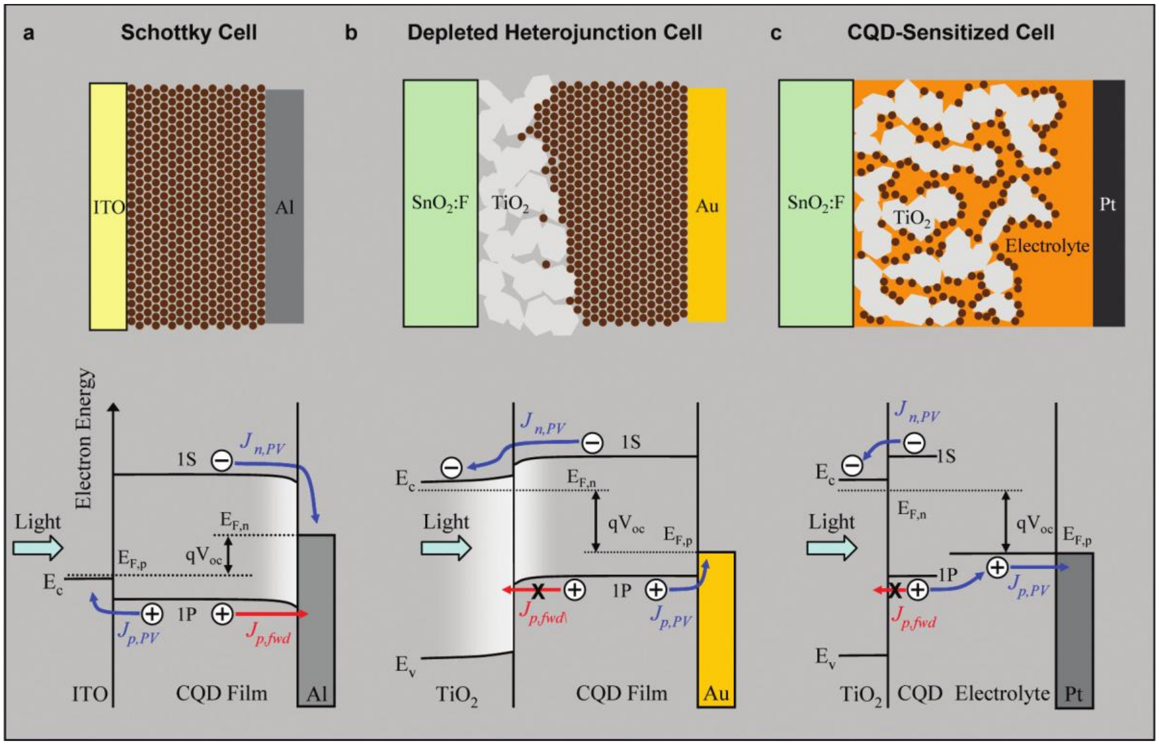

Figure 1-6. A schematic representation of the device structure and working principle for NP-based Schottky cell (Panel a), depleted heterojunction cell (Panel b), and sensitized cell (Panel C). Figure taken from reference 38.[38]

1.3.3 Depleted heterojunction solar cells

Solid-state depleted heterojunction solar cells (Panel b in Figure 1.6) are the most efficient NP-based photovoltaic technology to date.[39] Lead chalcogenide NPs are the most used materials in this type of cell because of their low bandgaps, high exciton Bohr radius, and low exciton binding energy.[25,40] A recent work by Sargent's group[39b] achieved an efficiency of 7 % for a PbS-NP depleted heterojunction cell. Similar to the NPSC, Figure 1.6 (Panel b) shows that the depleted heterojunction cells also have a FTO/TiO_2 electrode as the electron transport layer, above which a thin film (~200-400 nm) of the NP is spin- or dip-coated from the solution. The

Au back contact evaporated on top of the NP layer provides an ohmic contact to the hole transfer. The advantages of the depleted heterojunction cell over the NPSC are: 1) eliminating the corrosion of the NP by employing a solid-state approach; 2) simplifying the hole transfer process, and thus enhances hole transfer rate and inhibits charge recombination; and 3) accelerating the charge separation by using both donor-acceptor energy offsets and a built-in electric filed in the depletion region.

1.3.4 Schottky cells

Compared to the depleted heterojunction cells, the Schottky cells (Panel a in Figure 1.6) have a thin film of NPs sandwiched between a transparent conductive electrode (e.g., ITO) and a shallow work function metal back contact, such as Al. The photoinduced charge separation occurs at the NP/Al Schottky junction in which the Schottky barrier favors the extraction of electrons from the NP film, while blocking the hole transfer.[2a,10h] However, the largest limitation for the Schottky solar cells is that the charge separation interface is far away from the illumination front side (ITO/NP interface), which indicates that the excitons generated by the highest light intensity at the ITO/NP interface have to diffuse through the entire NP film before they reach the Schottky junction. This process significantly increases the probability for charge recombination. Moreover, the open circuit voltage (V_{oc}) of the Schottky cell is normally limited by Fermi-level pinning because of the presence of NP surface traps.[2a,10h]

1.4 CHALLENGES AND OUTLOOKS

Despite the rapid improvement for the efficiency, NP-based photovoltaics still have to overcome many challenges in order to meet the requirement of large-scale commercialization and long-term usage. Reducing the photovoltaic cost can be potentially achieved by using solution-processing methods, flexible substrates, and earth-abundant semiconductor materials, such as Pb(S, Se), PbI_2, and In(Sb, As), etc.[41] Further improvement for the efficiency has to reply on some transformative research breakthroughs, especially in a few largely unexplored areas as discussed below.

1.4.1 Trap states

Better surface-passivation and film-packing strategies are needed for making trap-free NPs and their PV devices.[42] To exceed power-conversion efficiencies of 10% in a single-junction planar cell, a material's electron and hole mobility should exceed 1 $cm^2\ V^{-1}\ s^{-1}$ and its bandgap should be as trap-free as possible ($< 10^{14}\ cm^{-3}$).[43] This requirement demands a deep understanding of the electronic coupling between the NP and its surface ligands. Much progress has been made towards this objective by using different bidentate ligands (or linker), such as ethanedithiol (EDT), benzenedithiol, and 3-mercaptopropionic acid (MPA). Sargent et al[39b] have recently reported that hybrid passivation with atomic chloride ligands and the MPA linkers reached an efficiency of 7% for a PbS-NP depleted heterojunction device, which is the highest reported to date. Time-resolved infrared spectroscopy revealed that the high efficiency was reached because the hybrid passivation reduced the density of trap states to a scale of $10^{16}\ cm^{-3}$, which is still two orders of magnitude higher than the desired value, however.

1.4.2 Device architectures

Novel device architectures are needed to enhance light absorption and charge extraction for semiconductor NPs.[43] Because of the size-tunable bandgap and bandedge, various sizes (or types) of the NPs can be integrated into a tandem cell, which has the ability of capturing a wide range of light. Researchers recently reported a tandem cell[44] comprising a visible-absorbing front cell (with 2 nm diameter PbS NP) and an infrared-absorbing back cell (with 4 nm diameter PbS NP). A recombination layer placed between these two cells provided a favorable energy alignment for hole current from the front cell and electron current from the back cell, while adding their open-circuit voltages without causing significant loss. Compared to the single junction device, the tandem cell showed a 40% improvement in the power conversion efficiency.

In addition, nanostructured electrodes can be used to enhance the charge extraction efficiency for the NP-base devices by providing a larger charge-separating interface.[23c,43] For instance, it has been recently demonstrated for a depleted heterojunction cell that a n-type TiO_2 layer with nanopillar structures can infiltrate into the PbS-NP film and form a "depleted bulk heterojunction",[45] which extends the volume of the depletion region into the NP film and enhances the charge separation and extraction efficiency. Moreover, the depleted bulk heterojunction with extended depletion region allows the use of a thicker NP film so that more light can be captured.

1.4.3 Fundamental physics

While much progress has been made in terms of the device optimization, many fundamental physical aspects remain largely unexplored for the NP-based photovoltaics. For example, despite the well-reported size-dependent energetics for isolated semiconductor NPs, it is incorrect to assume that these quantum properties will remain the same once the NPs are incorporated into the device, because the electronic couplings between the NP and its surroundings (e.g., neighboring NPs, ligands/linkers, or charge transport media) may alter the quantum confinement of the NPs by extending or squeezing the carrier wavefunctions. Thus, accurate determination of the NP energetics with the presence of those couplings is highly important. Several workers[15b,46] have found that the electronic interaction between the NP and the conductive substrate can pin the HOMO (or LUMO) of the NP to the Fermi level of the substrate. This finding is very important because the change of the NP bandedge can strongly affect charge transfer and charge separation dynamics.

In addition, the charge separation and charge recombination dynamics are not well-understood for the NP-based devices. Conventional Si-based solar cells use a built-in electric field in a depletion region to separate charges and inhibit recombination. In contrast, most NP-based devices are excitonic so that charge separation is mostly driven by the donor-acceptor energy offset. However, their charge separation efficiency largely suffers from germinate and/or non-germinate charge recombination processes,[31,47] originating from limited exciton diffusion length,[48] back charge transfer,[23c] and surface trap states.[27c,49] One way to overcome this challenge is to optimize the energy alignment and energy architecture of the NP with respect to the other components in the device.

Another way to enhance the charge separation for NP-based photovoltaics is via robust interfacial engineering at the donor-acceptor heterojunction. Researchers[50] have found a way to create an internal electric field between a NP donor and a NP acceptor. This field has a similar function as the built-in electrical field in conventional p-n junction solar cell, namely, enhancing charge separation and inhibiting charge recombination. The internal electric field was generated by placing opposite surface charge on the ligands of the donor and acceptor NPs, which are CdTe NPs and CdSe NPs in their study. When CdTe and CdSe NPs are negatively (-) and positively (+) charged respectively, their electrostatic assemblies in solution possessed an internal electrical field with a direction from (+)CdSe NP to (-)CdTe NP. Photoluminescence quenching experiments show a rapid charge transfer across the donor-acceptor junction for this assembly, because their internal electric field drives the charge separation in the same direction as the donor-acceptor energy offset. However, no significant charge transfer can be observed under the same condition with a reversed internal field, that is, for the assembly of (+)CdTe/(-)CdSe. Their results suggest that a dual charge-separation driving force can be utilized for the NP-based devices by combining the D-A energy offsets and the internal electrical field.

1.5 SCOPE OF THE DISSERTATION

In order to gain more insights about the fundamental physics for the semiconductor NPs and advance NP-based photovoltaic technologies, the studies included in this thesis aim to systematically study 1) the NP energetics in a model system when the effect of the surroundings comes into play; 2) the relation between the energy architecture/alignment and charge transfer rate for NP-based donor-acceptor systems; 3) the effect of the internal electric field on the charge transfer rate for an organic/inorganic (polymer/NP) hybrid donor/acceptor system; and 4) the interfacial engineering for facilitating charge transfer in NP-based PV devices. The ultimate goal of this thesis is to explore new strategies for enhancing charge separation, while inhibiting charge recombination for NP-based donor-acceptor systems and devices.

Chapter 2 discusses our work on determination of the size-dependent electronic energetics for CdSe and CdTe NP assemblies on Au electrodes. It reveals that the electronic coupling between the NP and the Au substrate produces an interfacial dipole that pins the HOMO of the NP to the Fermi level. Multiple characterization methods, including electrochemical, photoelectrochemical, and single/two-photon photoemission techniques, have been used in parallel to measure the energetics for various sized CdSe and CdTe NPs. The results from different methods are in good agreement with each other, and they are helpful for the following studies in which the energy architecture and alignment for NP-based donors and acceptors becomes important.

Chapter 3 addresses the relation between the energy architecture and the charge transfer rate for a CdTe-CdSe NP donor-acceptor system. First this work optimizes the energy architecture and alignment for the NP donor and NP acceptor with respect to the electron and hole transporting medium by tuning the NP size. Then, the photocurrent generated by the NP donor and acceptor, as an indicator for the charge transfer rate, is measured in two different systems, namely, one in an electrochemical cell and the other one in a p-n junction device. The results from both systems reveal that the spatial order of the NP donor and acceptor determines overall energy alignment within the device, and thus affects the charge transfer rate. This work demonstrates an idea of electrochemically-guided photovoltaic devices, in which the results from the electrochemical cell help to optimize the energy alignment in a real device.

Chapter 4 studies the effect of an internal electric field on the charge-separation efficiency for a hybrid polymer-NP donor-acceptor system. An internal charge-separating electric field is created by placing opposite surface charges on the polymer and NP surface. Thus, the electrostatic assemblies of the polymer and NP have an internal electric field at the donor-acceptor heterojunction, whose direction can be aligned with the donor-acceptor energy offsets. The combination of the internal electric field and the energy offsets generates a dual charge-separation driving force, which can help achieve efficient charge separation and inhibit charge recombination. This work sheds light on developing “smart” donor-acceptor materials for hybrid bulkheterojunction solar cells by combining donor-acceptor energy offsets and the internal electric field.

Chapter 5 shows our recent work about the effect of thermal annealing on the heterojunction microstructure and energy conversion efficiency for a TiO_2/PbS NP depleted heterojunction solar cell. Nanoscale structure and composition analysis have revealed that thermal annealing causes intermixing of the TiO_2 and PbS NP phase at the heterojunction. This intermixing leads to the formation of a depleted bulk heterojunction (DBH) which increases the depleted volume and promotes the carrier extraction from PbS NP to TiO_2. In addition, the thermal annealing causes inter-particle necking between PbS NPs and increases the crystallinity of the PbS NP film; and thus enhances the photoconductivity. Compared to unannealed PbS/TiO_2 heterojunction solar cells, the formation of the DBH and the necking between PbS NPs led to a doubling of the short-circuit current (J_{sc}) and an improved energy conversion efficiency by 39%.

1.6 REFERENCES

(1) a) Alivisatos, A. P. *The Journal of Physical Chemistry* **1996**, *100*, 13226; b) Burda, C.; Chen, X.; Narayanan, R.; El-Sayed, M. A. *Chemical Reviews* **2005**, *105*, 1025; c) Talapin, D. V.; Lee, J.-S.; Kovalenko, M. V.; Shevchenko, E. V. *Chemical Reviews* **2009**, *110*, 389.

(2) a) Hetsch, F.; Xu, X.; Wang, H.; Kershaw, S. V.; Rogach, A. L. *The Journal of Physical Chemistry Letters* **2011**, *2*, 1879; b) Gur, I.; Fromer, N. A.; Geier, M. L.; Alivisatos, A. P. *Science* **2005**, *310*, 462; c) Nozik, A. J. *Physica E-Low-Dimensional Systems & Nanostructures* **2002**, *14*, 115.

(3) Kamat, P. V. *The Journal of Physical Chemistry C* **2008**, *112*, 18737.

(4) Knowles, K. E.; Peterson, M. D.; McPhail, M. R.; Weiss, E. A. *The Journal of Physical Chemistry C* **2013**, *117*, 10229.

(5) Sukhanova, A.; Devy, J.; Venteo, L.; Kaplan, H.; Artemyev, M.; Oleinikov, V.; Klinov, D.; Pluot, M.; Cohen, J. H. M.; Nabiev, I. *Analytical Biochemistry* **2004**, *324*, 60.

(6) Kamat, P. V. *The Journal of Physical Chemistry Letters* **2013**, *4*, 908.

(7) Bawendi, M. G.; Steigerwald, M. L.; Brus, L. E. *Annual Review of Physical Chemistry* **1990**, *41*, 477.

(8) Talapin, D. V.; Lee, J. S.; Kovalenko, M. V.; Shevchenko, E. V. *Chemical Reviews* **2010**, *110*, 389.

(9) Chan, E. M.; Xu, C.; Mao, A. W.; Han, G.; Owen, J. S.; Cohen, B. E.; Milliron, D. J. *Nano Letters* **2010**, *10*, 1874.

(10) a) Cao, Y. W.; Banin, U. *Angewandte Chemie-International Edition* **1999**, *38*, 3692; b) Battaglia, D.; Peng, X. G. *Nano Letters* **2002**, *2*, 1027; c) Vossmeyer, T.; Katsikas, L.; Giersig, M.; Popovic, I. G.; Diesner, K.; Chemseddine, A.; Eychmuller, A.; Weller, H. *Journal of Physical Chemistry* **1994**, *98*, 7665; d) Rogach, A. L.; Kornowski, A.; Gao, M. Y.; Eychmuller, A.; Weller, H. *Journal of Physical Chemistry B* **1999**, *103*, 3065; e) Yu, W. W.; Wang, Y. A.; Peng, X. G. *Chemistry of Materials* **2003**, *15*, 4300; f) Rogach, A.; Kershaw, S.; Burt, M.; Harrison, M.; Kornowski, A.; Eychmuller, A.; Weller, H. *Advanced Materials* **1999**, *11*, 552; g) McDonald, S. A.; Konstantatos, G.; Zhang, S. G.; Cyr, P. W.; Klem, E. J. D.; Levina, L.; Sargent, E. H. *Nature Materials* **2005**, *4*, 138; h) Luther, J. M.; Law, M.; Beard, M. C.; Song, Q.; Reese, M. O.; Ellingson, R. J.; Nozik, A. J. *Nano Letters* **2008**, *8*, 3488.

(11) Peng, Z. A.; Peng, X. G. *Journal of the American Chemical Society* **2001**, *123*, 183.

(12) Rogach, A. L.; Franzl, T.; Klar, T. A.; Feldmann, J.; Gaponik, N.; Lesnyak, V.; Shavel, A.; Eychmuller, A.; Rakovich, Y. P.; Donegan, J. F. *Journal of Physical Chemistry C* **2007**, *111*, 14628.

(13) a) Tvrdy, K.; Frantsuzov, P. A.; Kamat, P. V. *Proceedings of the National Academy of Sciences* **2011**, *108*, 29; b) Kongkanand, A.; Tvrdy, K.; Takechi, K.; Kuno, M.; Kamat, P. V. *Journal of the American Chemical Society* **2008**, *130*, 4007.

(14) a) Peng, X. G.; Manna, L.; Yang, W. D.; Wickham, J.; Scher, E.; Kadavanich, A.; Alivisatos, A. P. *Nature* **2000**, *404*, 59; b) Manna, L.; Scher, E. C.; Alivisatos, A. P. *Journal of the American Chemical Society* **2000**, *122*, 12700; c) Yin, Y.; Alivisatos, A. P. *Nature* **2005**, *437*, 664.

(15) a) Wuister, S. F.; Donega, C. D.; Meijerink, A. *Journal of Physical Chemistry B* **2004**, *108*, 17393; b) Wang, Y.; Xie, Z.; Gotesman, G.; Wang, L.; Bloom, B. P.; Markus, T. Z.; Oron, D.; Naaman, R.; Waldeck, D. H. *The Journal of Physical Chemistry C* **2012**, *116*, 17464.

(16) Ji, X. H.; Copenhaver, D.; Sichmeller, C.; Peng, X. G. *Journal of the American Chemical Society* **2008**, *130*, 5726.

(17) Owen, J. S.; Park, J.; Trudeau, P. E.; Alivisatos, A. P. *Journal of the American Chemical Society* **2008**, *130*, 12279.

(18) He, M.; Qiu, F.; Lin, Z. *The Journal of Physical Chemistry Letters* **2013**, 1788.

(19) Liu, W. H.; Greytak, A. B.; Lee, J.; Wong, C. R.; Park, J.; Marshall, L. F.; Jiang, W.; Curtin, P. N.; Ting, A. Y.; Nocera, D. G.; Fukumura, D.; Jain, R. K.; Bawendi, M. G. *Journal of the American Chemical Society* **2010**, *132*, 472.

(20) Nag, A.; Kovalenko, M. V.; Lee, J. S.; Liu, W. Y.; Spokoyny, B.; Talapin, D. V. *Journal of the American Chemical Society* **2011**, *133*, 10612.

(21) Dong, A. G.; Ye, X. C.; Chen, J.; Kang, Y. J.; Gordon, T.; Kikkawa, J. M.; Murray, C. B. *Journal of the American Chemical Society* **2011**, *133*, 998.

(22) Law, M.; Luther, J. M.; Song, O.; Hughes, B. K.; Perkins, C. L.; Nozik, A. J. *Journal of the American Chemical Society* **2008**, *130*, 5974.

(23) a) Koleilat, G. I.; Levina, L.; Shukla, H.; Myrskog, S. H.; Hinds, S.; Pattantyus-Abraham, A. G.; Sargent, E. H. *Acs Nano* **2008**, *2*, 833; b) Klem, E. J. D.; MacNeil, D. D.; Cyr, P. W.; Levina, L.; Sargenta, E. H. *Applied Physics Letters* **2007**, *90*; c) Graetzel, M.; Janssen, R. A. J.; Mitzi, D. B.; Sargent, E. H. *Nature* **2012**, *488*, 304.

(24) a) Santra, P. K.; Kamat, P. V. *Journal of the American Chemical Society* **2013**, *135*, 877; b) Kramer, I. J.; Levina, L.; Debnath, R.; Zhitomirsky, D.; Sargent, E. H. *Nano Letters* **2011**, *11*, 3701.

(25) Nozik, A. J.; Beard, M. C.; Luther, J. M.; Law, M.; Ellingson, R. J.; Johnson, J. C. *Chemical Reviews* **2011**, *110*, 6873.

(26) a) Semonin, O. E.; Luther, J. M.; Choi, S.; Chen, H. Y.; Gao, J. B.; Nozik, A. J.; Beard, M. C. *Science* **2011**, *334*, 1530; b) Beard, M. C. *Journal of Physical Chemistry Letters* **2011**, *2*, 1282.

(27) a) Zhao, L.; Lin, Z. Q. *Advanced Materials* **2012**, *24*, 4353; b) Reiss, P.; Couderc, E.; De Girolamo, J.; Pron, A. *Nanoscale* **2011**, *3*, 446; c) Martinez-Ferrero, E.; Albero, J.; Palomares, E. *Journal of Physical Chemistry Letters* **2010**, *1*, 3039; d) Milliron, D. J.; Gur, I.; Alivisatos, A. P. *Mrs Bulletin* **2005**, *30*, 41.

(28) Liang, Y.; Yu, L. *Accounts of Chemical Research* **2010**, *43*, 1227.

(29) Gregg, B. A.; Chen, S. G.; Cormier, R. A. *Chemistry of Materials* **2004**, *16*, 4586.

(30) Ren, S.; Chang, L.-Y.; Lim, S.-K.; Zhao, J.; Smith, M.; Zhao, N.; Bulović, V.; Bawendi, M.; Gradečak, S. *Nano Letters* **2011**, *11*, 3998.

(31) a) ten Cate, S.; Schins, J. M.; Siebbeles, L. D. A. *Acs Nano* **2012**, *6*, 8983; b) Ohkita, H.; Cook, S.; Astuti, Y.; Duffy, W.; Tierney, S.; Zhang, W.; Heeney, M.; McCulloch, I.; Nelson, J.; Bradley, D. D. C.; Durrant, J. R. *Journal of the American Chemical Society* **2008**, *130*, 3030.

(32) http://www.meh.uni-freiburg.de/research/currentresearch/fieldB/B2.

(33) Oregan, B.; Gratzel, M. *Nature* **1991**, *353*, 737.

(34) Santra, P. K.; Kamat, P. V. *Journal of the American Chemical Society* **2012**, *134*, 2508.

(35) Lee, M. M.; Teuscher, J.; Miyasaka, T.; Murakami, T. N.; Snaith, H. J. *Science* **2012**, *338*, 643.

(36) a) Hodes, G. *The Journal of Physical Chemistry C* **2008**, *112*, 17778; b) Hod, I.; González-Pedro, V.; Tachan, Z.; Fabregat-Santiago, F.; Mora-Seró, I.; Bisquert, J.; Zaban, A. *The Journal of Physical Chemistry Letters* **2011**, *2*, 3032; c) Kamat, P. V. *Accounts of Chemical Research* **2012**, *45*, 1906.

(37) a) Bang, J. H.; Kamat, P. V. *ACS Nano* **2009**, *3*, 1467; b) Chakrapani, V.; Baker, D.; Kamat, P. V. *Journal of the American Chemical Society* **2011**, *133*, 9607.

(38) Pattantyus-Abraham, A. G.; Kramer, I. J.; Barkhouse, A. R.; Wang, X. H.; Konstantatos, G.; Debnath, R.; Levina, L.; Raabe, I.; Nazeeruddin, M. K.; Gratzel, M.; Sargent, E. H. *Acs Nano* **2010**, *4*, 3374.

(39) a) Kramer, I. J.; Sargent, E. H. *Acs Nano* **2011**, *5*, 8506; b) Ip, A. H.; Thon, S. M.; Hoogland, S.; Voznyy, O.; Zhitomirsky, D.; Debnath, R.; Levina, L.; Rollny, L. R.;

Carey, G. H.; Fischer, A.; Kemp, K. W.; Kramer, I. J.; Ning, Z. J.; Labelle, A. J.; Chou, K. W.; Amassian, A.; Sargent, E. H. *Nature Nanotechnology* **2012**, *7*, 577.

(40) Talapin, D. V.; Murray, C. B. *Science* **2005**, *310*, 86.

(41) Wadia, C.; Alivisatos, A. P.; Kammen, D. M. *Environmental Science & Technology* **2009**, *43*, 2072.

(42) a) Tang, J.; Kemp, K. W.; Hoogland, S.; Jeong, K. S.; Liu, H.; Levina, L.; Furukawa, M.; Wang, X. H.; Debnath, R.; Cha, D. K.; Chou, K. W.; Fischer, A.; Amassian, A.; Asbury, J. B.; Sargent, E. H. *Nature Materials* **2011**, *10*, 765; b) Jeong, K. S.; Tang, J.; Liu, H.; Kim, J.; Schaefer, A. W.; Kemp, K.; Levina, L.; Wang, X. H.; Hoogland, S.; Debnath, R.; Brzozowski, L.; Sargent, E. H.; Asbury, J. B. *Acs Nano* **2012**, *6*, 89.

(43) Sargent, E. H. *Nature Photonics* **2012**, *6*, 133.

(44) Wang, X. H.; Koleilat, G. I.; Tang, J.; Liu, H.; Kramer, I. J.; Debnath, R.; Brzozowski, L.; Barkhouse, D. A. R.; Levina, L.; Hoogland, S.; Sargent, E. H. *Nature Photonics* **2011**, *5*, 480.

(45) a) Kramer, I. J.; Zhitomirsky, D.; Bass, J. D.; Rice, P. M.; Topuria, T.; Krupp, L.; Thon, S. M.; Ip, A. H.; Debnath, R.; Kim, H. C.; Sargent, E. H. *Advanced Materials* **2012**, *24*, 2315; b) Barkhouse, D. A. R.; Debnath, R.; Kramer, I. J.; Zhitomirsky, D.; Pattantyus-Abraham, A. G.; Levina, L.; Etgar, L.; Gratzel, M.; Sargent, E. H. *Advanced Materials* **2011**, *23*, 3134.

(46) a) Xie, Z. T.; Markus, T. Z.; Gotesman, G.; Deutsch, Z.; Oron, D.; Naaman, R. *Acs Nano* **2011**, *5*, 863; b) Markus, T. Z.; Itzhakov, S.; Akotzer, Y. I.; Cahen, D.; Hodes, G.; Oron, D.; Naaman, R. *Journal of Physical Chemistry C* **2011**, *115*, 13236; c) Markus, T. Z.; Wu, M.; Wang, L.; Waldeck, D. H.; Oron, D.; Naaman, R. *Journal of Physical Chemistry C* **2009**, *113*, 14200; d) Timp, B. A.; Zhu, X. Y. *Surface Science* **2010**, *604*, 1335; e) Carlson, B.; Leschkies, K.; Aydil, E. S.; Zhu, X. Y. *Journal of Physical Chemistry C* **2008**, *112*, 8419.

(47) a) Credgington, D.; Jamieson, F. C.; Walker, B.; Nguyen, T.-Q.; Durrant, J. R. *Advanced Materials* **2012**, *24*, 2135; b) Groves, C.; Blakesley, J. C.; Greenham, N. C. *Nano Letters* **2010**, *10*, 1063.

(48) Shaw, P. E.; Ruseckas, A.; Samuel, I. D. W. *Advanced Materials* **2008**, *20*, 3516.

(49) a) Zhou, R.; Xue, J. *ChemPhysChem* **2012**, *13*, 2471; b) Noone, K. M.; Subramaniyan, S.; Zhang, Q.; Cao, G.; Jenekhe, S. A.; Ginger, D. S. *The Journal of Physical Chemistry C* **2011**, *115*, 24403.

(50) Wu, M. Y.; Mukherjee, P.; Lamont, D. N.; Waldeck, D. H. *Journal of Physical Chemistry C* **2010**, *114*, 5751.

2.0 DETERMINATION OF THE ELECTRONIC ENERGETICS OF SEMICONDUCTOR NANOPARTICLE

This work has been published as Wang, Y.; Xie, Z.; Gotesman, G.; Wang, L.; Bloom, B. P.; Markus, T. Z.; Oron, D.; Naaman, R.; Waldeck, D. H. *The Journal of Physical Chemistry C* **2012**, 116, 17464. The thesis author prepared all the samples, conducted electrochemical and photocurrent measurements, analyzed data, and prepared the manuscript. The supporting information for this chapter is provided in Appendix A.

This work explores the electronic states of CdTe semiconductor nanoparticles (NPs) that are immobilized on a polycrystalline Au film through an organic linker (dithiol). The HOMO and LUMO energies of the CdTe NPs were determined by using photoelectron spectroscopy and cyclic voltammetry. The results from these measurements show that the HOMO energy is independent of the nanoparticle size and is pinned to the Fermi level, while the LUMO energy changes systematically with the size of the NP. Studies with different capping ligands imply that the dithiol ligand removes surface states and enhances the optoelectronic properties of the NPs.

2.1 INTRODUCTION

The electronic structure of semiconductor nanoparticles (NPs) is important for their use in optoelectronics,[1] photovoltaics,[2] and photocatalysis.[3] In order to optimize performance of the NP in these applications, it is necessary to understand and control the alignment between the energy levels of the NPs and the substrates (or electrodes), e.g., at the interface of NPs and a TiO_2 substrate in a quantum dot sensitized solar cell,[4] or at the interface of NPs and a back metal contact in a Schottky photovoltaic device.[5] Although much is known from the solid-state physics literature about semiconductor and metal-semiconductor interfaces, relatively few works have addressed the metal-semiconductor nanoparticle interface. This work uses photoelectron spectroscopy and electrochemistry methods to probe the electronic states of CdTe NPs that are assembled into a monolayer film on a polycrystalline Au film by a dithiol linker.

In an earlier study, we used photoelectron spectroscopy and cyclic voltammetry to investigate the electronic states of CdSe NPs that were adsorbed on a polycrystalline Au film via a dithiol (DT) organic linker.[6] That study showed that the HOMO energy of the CdSe NP was independent of its size (for sizes greater than 2.8 nm diameter), and it was pinned at ∼1.25 eV below the Fermi level of the Au. In contrast, the LUMO energy of the CdSe NP changed systematically with its size. A similar effect was reported by us for the case of CdSe/ZnS core/shell NPs.[7] Also, in the case of CdSe[8] and PbSe[9] NPs, it has been reported that the HOMO is 'pinned' to the Fermi level of a ZnO semiconductor substrate, when a short organic linker, such as 3-mercaptopropionic acid or ethanedithiol, is used to tether them. Presumably, the pinning results from a high density of interfacial states at the metal-nanoparticle interface.[6,10]

Given these reports for the Fermi level pinning of CdSe NPs and the chemical similarities of CdSe and CdTe, it is interesting to explore the nature of the CdTe NP interaction with Au and whether the HOMO of CdTe NPs are pinned relative to the Fermi level of Au. Two earlier studies have examined the electronic states of CdTe NPs at electrode interfaces. Haram et al[11] used cyclic voltammetry to determine the HOMO and LUMO energies of CdTe NPs diffusing in solution. Under these conditions, the electrochemical and optical determinations of the HOMO-LUMO gap were in excellent agreement, and they found that the HOMO energy changed with the size of the NP – presumably because it was not immobilized on the electrode. Jasieniak et al.[12] used a photoelectron spectroscopy in air method to examine the electronic states of CdSe and CdTe NPs in drop cast films on indium-tin oxide electrodes. Their data suggest a weak dependence of the HOMO energy on the particle size for both CdSe and CdTe NPs. The HOMO and LUMO energies that were assigned to the CdTe NPs in these two studies differ by 0.5 to 1.0 eV. Part of this energy difference may be caused by the different capping ligands on the NPs used in those two works; it has been reported that the dipole moment of the ligand can affect the energetics of the NPs.[13] Another complicating feature of the comparison is the different substrate/electrode that was used in these two studies.[9]

This work examines the electronic states of CdTe NPs on Au electrodes by photoemission and cyclic voltammetry. The same substrate, the same capping ligand, and the same sample preparation method are used for the photoelectron spectroscopy and cyclic voltammetry measurements to ensure that the two systems are quantitatively comparable. This work provides a rigorous determination of the HOMO and LUMO energies of CdTe NPs and demonstrates consistency between the photoelectron and cyclic voltammetry methods. This study finds that the HOMO of the CdTe NPs is pinned with respect to the Fermi level and that the capping ligands affect the exciton lifetime of the CdTe NPs.

2.2 EXPERIMENTAL METHODS AND MATERIALS

2.2.1 Materials

Cadmium oxide and trioctyl phosphine (TOP) were purchased from Strem Chemicals. Tetradecylphosphonic acid (TDPA) was purchased from PolyCarbon Industries. All of the other chemicals were purchased from Sigma Aldrich and were used without further purification, unless mentioned otherwise.

2.2.2 Synthesis of NPs

TDPA-CdTe nanoparticles (NPs) were synthesized by using previously published methods.[14] Briefly, a solution of the tellurium precursor (0.2 mmol Te/ 1 ml TOP) was hot-injected into a solution of the cadmium precursor (0.4 mmol CdO/ 0.8 mmol TDPA/ 5 ml 1-octadecene) at 300 °C. The sizes of the NPs were controlled by the duration of the reaction and by extra injections of the cadmium and tellurium precursors. Figures 2.1A and 2.1B show the steady-state absorption and photoluminescence spectra measured in toluene for the small (S), medium (M), and large (L) CdTe NPs used in this work. By inputting the wavelength of the first excitonic peak into an established model,[15] the average size of the NPs is calculated to be about 3.71 nm for S, 4.15 nm for M, and 6.00 nm for L NPs.

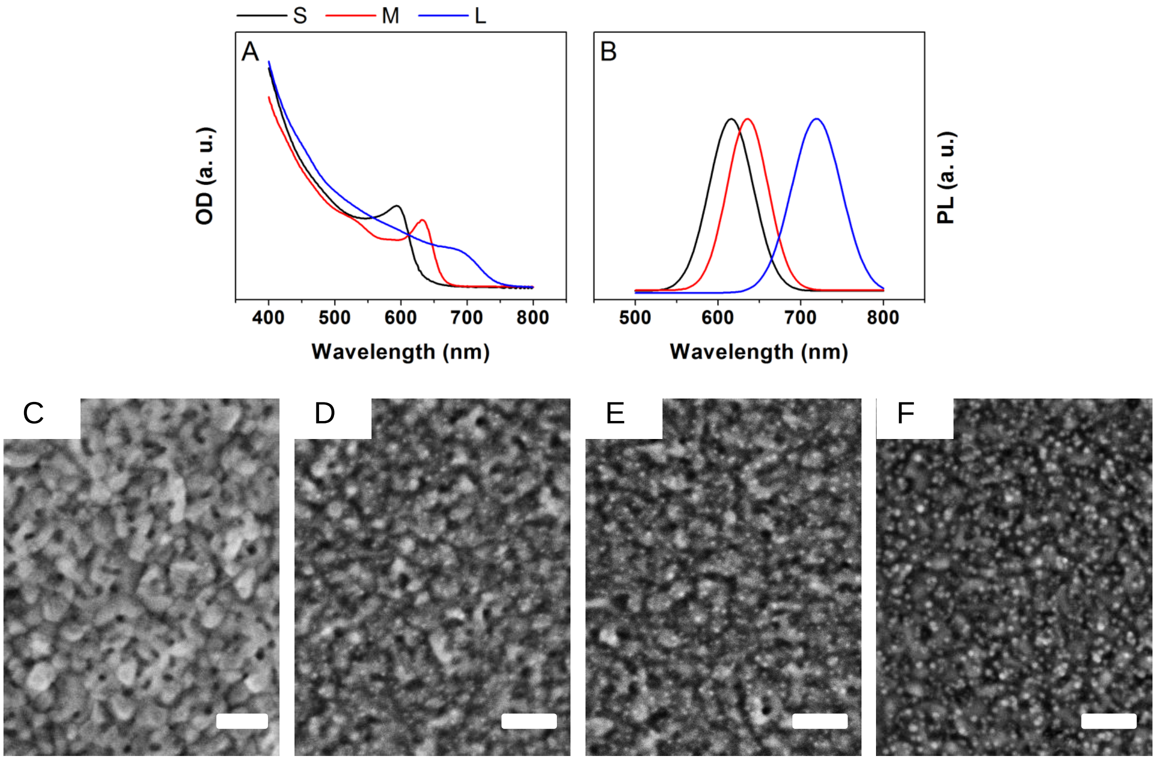

Figure 2-1. Panels A and B show the steady-state absorption (OD) and photoluminescence (PL) spectra for the small (S, black), medium (M, red), and large (L, blue) CdTe NPs in toluene. Panels C to F show the SEM images for the bare Au substrate (C), Au/DT/S-NP (D), Au/DT/M-NP (E), and Au/DT/L-NP (F). All scale bars are 100 nm.

2.2.3 Sample preparation

The Au substrate was either 150 nm thick Au films on silicon (100) for photoelectron spectroscopic measurements, or it was Au ball electrodes for cyclic voltammetry and photocurrent measurements in an electrochemical cell. The same procedure was used to make NP assemblies in both cases. Namely, the clean Au substrate was immersed overnight in a methanol solution of 1 mM 1,9-nonanedithiol (DT) to create a monolayer of DT on the Au surface. The Au-dithiol substrate (Au/DT) was then placed into a toluene solution of CdTe NPs (optical density around 0.2) for 0.5 to 3 h to immobilize the NPs on the surface, creating a Au/DT/NP assembly. This assembly process was characterized by scanning electron microscopy (SEM). Panels C through F of Figure 2.1 show SEM images for the bare Au substrate, the small NPs on Au (Au/DT/S-NP), the medium NPs on Au (Au/DT/M-NP), and the large NPs on Au (Au/DT/L-NP). These images reveal the roughness features of the evaporated Au film and illustrate that different NP sizes are adsorbed onto the Au/DT substrate in the three cases. Based on the SEM images, the surface coverage of the NPs on Au is estimated to be about 750/μm^2 for the S-NPs, 1250/μm^2 for the M-NPs, and 2500/μm^2 for the L-NPs. For studies requiring a capping layer of DT on the CdTe NPs, the Au/DT/NP assemblies were immersed into the DT solution again to create an assembly of Au/DT/NP/DT.

2.2.4 Photoelectron spectroscopy

Both single photon and two photon photoelectron techniques were used to determine the band-edge energies of CdTe NPs. The Au/DT/NP assemblies were placed in an ultrahigh vacuum chamber (<10^{-8} Torr) where an incident laser pulse excited the samples and the energy of the photoelectron was measured by a time-of-flight spectrometer. More details of the apparatus can be found in reference 18. Because the Au substrate is grounded and the laser intensity and repetition rate (10 Hz) are kept low, the samples do not retain any significant amount of net charge between laser pulses. This was verified by observing a stable electron energy spectrum which does not vary with time.

For the single-photon low-energy photoelectron transmission spectroscopy (LEPET, Scheme 2.1A), the photon energy is higher than the work function of the sample, so that the photoelectrons are directly ejected from states below the Fermi level to above the vacuum level and transmitted to the detector. This measurement provides information on the sample's density of states below the Fermi level, including the HOMO of the NP and surface states of the substrate and the NPs.[16]

The two-photon photoelectron spectroscopy (TPPE, Scheme 2.1B) uses photons with an energy lower than the work function of the sample. The first photon, the "pump" photon, excites electrons from below the Fermi level to unoccupied states (i.e., the "intermediate" states) above the Fermi level but below the vacuum level. Although most of the electrons relax fully to the Fermi level, some fractions are captured by the lowest unoccupied state (the LUMO) of the nanoparticle where they can be trapped for a longer time. If a second laser photon (the 'probe' photon) arrives on the sample before all of the trapped electrons recombine back into the metal substrate, then some fraction of these electrons can be excited to above the vacuum level. Thus, the measured kinetic energy of these photoelectrons provides information about the energy of the metastable state, LUMO of the NPs.

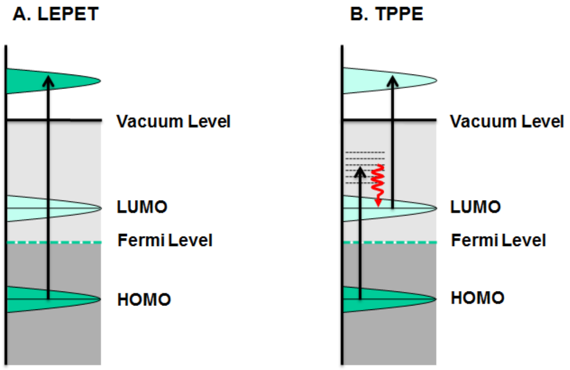

Scheme 2-1. A schematic description of the photoelectron spectroscopic techniques used in this study. A) The low energy photoelectron transmission spectroscopy (LEPET) for measuring the HOMO. B) The two photon photoelectron spectroscopy (TPPE) for measuring the LUMO.

2.2.5 Cyclic voltammetry

The cyclic voltammetry was performed in a three electrode electrochemical cell with a CHI 618B potentiostat. A chemically modified Au ball electrode (e.g., Au/DT/NP) was used as a working electrode, a Pt wire was used as a counter electrode, and $Ag/AgNO_3$ was used as a reference electrode (0.54 V vs. NHE). The supporting electrolyte was a 100 mM acetonitrile solution of tetrabutylammoniumhexafluorophosphate ($TBAPF_6$). The scan rate was 0.05 V/s.

2.2.6 Photocurrent measurement

Photocurrent measurements at a controlled bias potential were performed in the same electrochemical cell. In these studies triethanolamine (TEA) was added into the supporting electrolyte solution at a concentration of 20 mM to act as a hole scavenger and ensure a stable photocurrent. The illumination was provided by a 75 W Xe arc lamp coupled with a multimode optical fiber. At a working distance of 2.54 cm, this setup provided an illumination area of 7 mm^2. The illumination was chopped at 1 Hz by a motorized shutter. See reference 3 for more details.

2.3 RESULTS

2.3.1 Photoemission Studies

LEPET. Figure 2.2A shows LEPET spectra for the dithiol coated gold electrodes (Au/DT) and three different gold/dithiol/nanoparticle (Au/DT/NP) assemblies when excited by 6.42 eV photons. Because the LEPET method measures the density of states below the Fermi level, the high kinetic energy cutoff (3.05 ± 0.05 eV) corresponds to the photoelectrons ejected from just below the Fermi level. For the Au/DT reference substrate, the work function is $\Phi = 4.6 \pm 0.1$ eV (given by the photon energy minus the total width of the spectrum, ~ 1.8 eV). The Au/DT/NP assemblies exhibited a strong peak at a kinetic energy of about 1.3 eV, which is not present in the Au/DT reference sample. The photoelectron signal of this peak increases as the surface coverage of the NP increases (see Figure A1 in Appendix A). Thus, the peak at 1.3 eV is assigned to photoelectrons ejected from the filled levels of the NPs. Figure 2.2B shows the photoelectron signal of the Au/DT/NP assemblies after the signal from the Au/DT reference has been subtracted, and Figure 2.2C shows a plot in which the resultant spectra are rescaled to the same peak height. Using the rescaled spectra in Figure 2.2C, the HOMO (or band edge) energy of the NP was determined by linearly extrapolating on the high kinetic energy side to determine a cutoff energy. For all three sizes of NPs, the photoelectron distribution has the same cut-off kinetic energy of 2.25 ± 0.05 eV. This value is 0.80 ± 0.05 eV below the Au/DT Fermi level and is assigned to the HOMO energy of the CdTe NPs. In Figures 2.2A and 2.2B, the size-dependent variations in the spectral intensity and width are likely caused by the difference in the NP surface coverage on Au and/or the NP absorption cross-section.

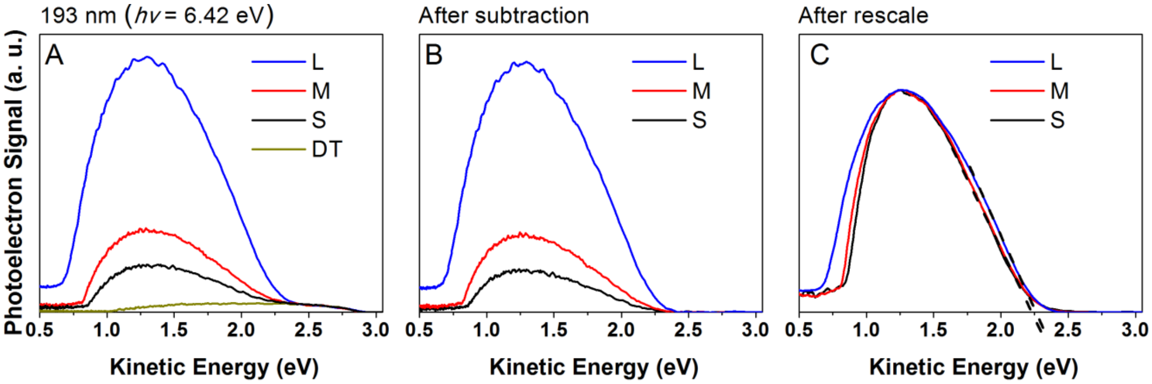

Figure 2-2. Panel A shows the LEPET spectrum for Au/DT (dark yellow), Au/DT/S-NP (black), Au/DT/M-NP (red), and Au/DT/L-NP (blue). L, M, and S indicate the nanoparticle size – large, medium, and small, respectively. Panel B shows the corresponding spectra after the subtraction of the Au/DT spectrum. Panel C shows the spectra in Panel B after scaling them to the same signal height, and it shows the extrapolation to the high kinetic energy cutoff.

The LEPET data in Figure 2.2 demonstrate that the HOMO energy of the CdTe NPs does not change over the NP size range of 3.7 nm to 6.0 nm. Although differing in details, these data are similar to that reported earlier for CdSe NPs immobilized on Au electrodes.[6-7] A quantitative comparison with the previous CdSe NP result shows that the HOMO energy of CdTe NPs assembled on Au/DT is about 0.4 ± 0.1 eV higher than that of CdSe NPs. This difference is similar to that reported by Jasiniek[12] for drop cast films of CdSe NPs and CdTe NPs on ITO.

TPPE. Because the HOMO/LUMO bandgap changes with the NP size and the HOMO energy is not changing with the NP size, one expects that the LUMO energy should shift with the size of the NPs.[6] Unfortunately, the TPPE spectra (see Figure A2 in the Appendix A) for the assemblies of Au/DT/NP do not show a clear signal from the LUMO of the NP. This result suggests that the excited electron on the LUMO level recombines too rapidly for a sufficient population of metastable electrons to be created. Attempts to increase the population by increasing the laser intensity were not successful because of the onset of direct non-linear photoemission. In order to increase the population of trapped electrons in the nanoparticle's LUMO, the organic capping ligand was exchanged in order to change the surface state distribution on the NP and decrease the surface recombination rate.[17] Because thiol ligands are known to extend the exciton lifetime for the CdTe NPs,[17a] a second monolayer of dithiol (DT) molecules was used to replace the TDPA from the immobilized NPs (Scheme 2.2).

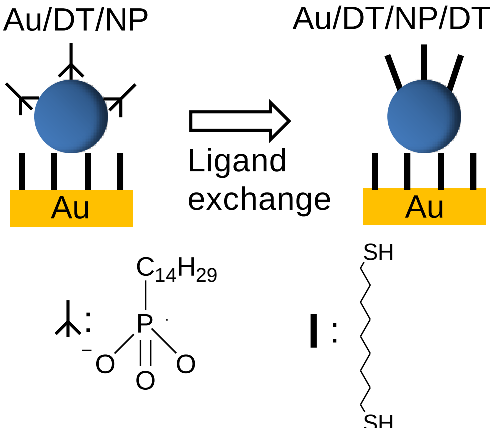

Scheme 2-2. This scheme shows the ligand exchange process from Au/DT/NP to Au/DT/NP/DT.

After replacing the TDPA ligand with a thiol ligand, the TPPE spectra showed a clear spectral signature from metastable electronic states. Figure 2.3 compares the normalized TPPE spectrum of Au/DT/M-NP (the black line) with that of Au/DT/M-NP/DT (the red solid line). These data show that a shoulder appears at a high kinetic energy for the assembly of Au/DT/M-NP/DT after the ligand exchange. If one subtracts the signal of Au/DT/M-NP from that of Au/DT/M-NP/DT, the shoulder can be separated; it is shown as the red dashed line in Figure 2.3. It has a peak located at 1.00 ± 0.05 eV above the Fermi level.

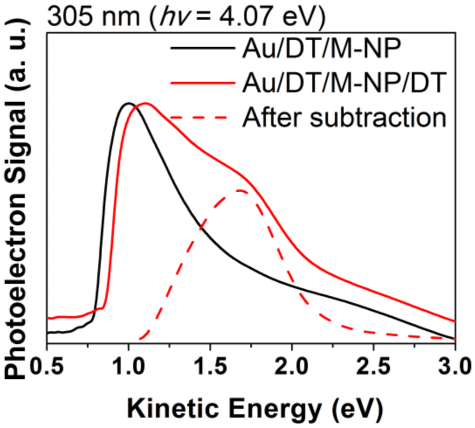

Figure 2-3. This figure compares the TPPE spectra for M-NP assemblies before (black solid) and after (red solid) the ligand exchange. The red-dashed line is generated by subtracting the black solid line from the red solid one.

As discussed elsewhere,[8] the kinetic energy of the photoelectrons, which arise from the LUMO in the TPPE measurement, should shift one-fold with the change of the probe photon's energy. As can be seen in Figure 2.4B, the separated peak shifts linearly with the probe photon's energy, and thus it is assigned to the LUMO of the M-NP. The TPPE spectra for Au/DT/S-NP/DT and Au/DT/L-NP/DT assemblies show the same general behavior, namely a shoulder arising at a high kinetic energy that shifts linearly with the probe photon energy, see Figures 2.4A and 4C. From these data, the LUMO energies are determined to be 1.07 ± 0.05 eV for S-NPs, 1.00 ± 0.05 eV for M-NPs, and 0.88 ± 0.05 eV for L-NPs, above the Fermi level of the Au substrate. Details of this calculation are provided in the supplemental information (see Figures S2.2 and S2.3). In Figure 2.4, the spectral width for the L-NPs is narrower than that of the M-NPs or S-NPs. This difference is attributed to the low kinetic energy peak in the TPPE spectra being more dominant for the L-NPs than for the S- or M-NPs. As a result it is more difficult to observe the high kinetic energy shoulder in the L-NPs TPPE spectra after the subtraction and the normalized spectrum appears narrower.

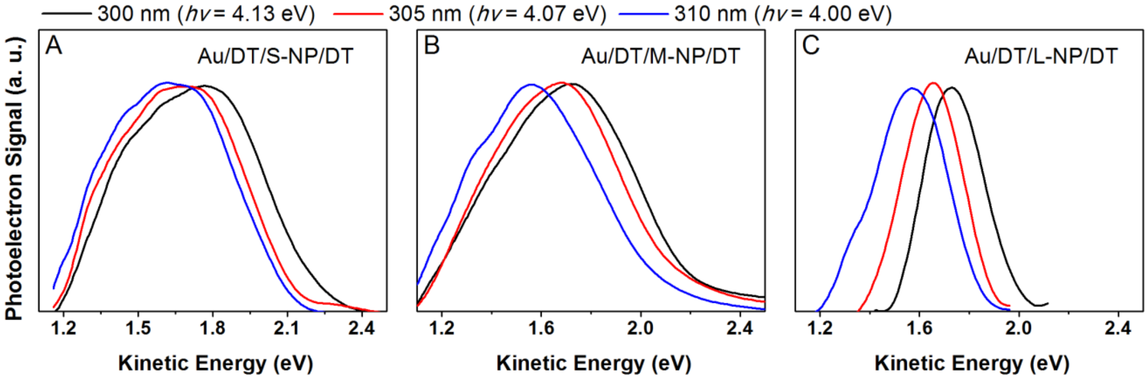

Figure 2-4. Panels A to C present the TPPE spectra for the assemblies of Au/DT/S-NP/DT, Au/DT/M-NP/DT, and Au/DT/L-NP/DT; the black (4.13 eV), red (4.07 eV), and blue line (4.00 eV) are the three different second photon energies used in the TPPE measurements (see legend).

The ligand exchange with DT was found to increase the exciton lifetime of the NPs, as well as the lifetime of trapped electrons in the NPs LUMO. This fact was demonstrated by comparing surface photoluminescence (PL) spectra for the assemblies of Au/DT/NP and Au/DT/NP/DT. While a significant photoluminescence signal from the assemblies of Au/DT/NP/DT could be obtained (see Figures S2.4), no measurable signal could be collected from the Au/DT/NP assemblies. This result supports the hypothesis that the DT ligands change the surface state distribution in a way that extends the exciton lifetime. The peak energies of the photoluminescence spectra provide a direct measure of the optical band gap of the NPs. A comparison of this optical band gap with the band gap computed from the LUMO and HOMO energy assignments are in excellent agreement (see Table 2.1). This latter observation substantiates the assignment of the HOMO and LUMO energies to the features in the photoelectron spectra.

Table 2.1. The band gap of the NPs measured by PL and PES

NP	Bandgap (eV)	
	Δ_{PL}	Δ_{PES}
S-NP	1.94	1.87
M-NP	1.86	1.80
L-NP	1.69	1.68

Δ_{PES} has an error of $\pm$ 0.1 eV.

Despite its effect on the recombination rate and the energy distribution of surface states, the DT ligand exchange does not affect the HOMO energies of the NPs. LEPET spectra were collected for the Au/DT/NP/DT assemblies and the HOMO energies were determined to be the same as those for the Au/DT/NP assemblies. Note that the ligand exchange did change the work function for the NP assemblies from 4.2 $\pm$ 0.1 eV (for Au/DT/NP) to 4.3 $\pm$ 0.1 eV (Au/DT/NP/DT). These data are provided in the Supplemental Information (see Figure A5). This fact indicates that the HOMO level pinning is controlled by the dithiol linker between the NPs and the Au substrate. Figure 2.5 plots the density of electronic states distributions obtained by PES for the three different sizes of Au/DT/NP/DT assemblies as a function of the electron binding energy. The procedure used for obtaining the density of states has been described elsewhere.[18] The zero of energy is set at the Fermi level. These data provide the density of electronic states for the NPs, and show that the HOMO is pinned at 0.80 $\pm$ 0.05 eV below the Fermi level, while the LUMO is size-dependent.

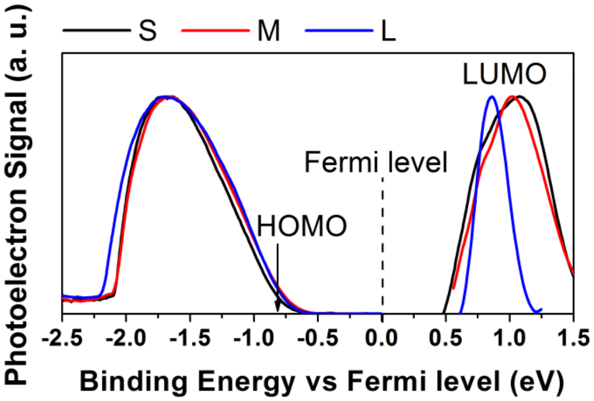

Figure 2-5. This figure plots the LEPET and TPPE spectra together as a function of binding energy versus the Fermi level, for the three assemblies of Au/DT/NP/DT.

2.3.2 Voltammetry studies

Because oxidation and reduction potentials can be directly related to the HOMO and LUMO energies of NPs,[6,19] cyclic voltammetry was used to determine the energy of the HOMO for the TDPA-capped CdTe NPs. Figure 2.6A shows cyclic voltammograms for the Au/DT/S-NP (black), Au/DT/M-NP (red), Au/DT/L-NP (blue), and Au/DT (SAM, dark yellow) assemblies. All of the assemblies, including the Au/DT reference system, show a weak peak near 1.0 V vs Ag/AgNO$_3$, and it is assigned to oxidation of the Au/DT. Each of the three assemblies with CdTe NPs show two strong oxidation peaks: one at ~ 0.50 V vs Ag/AgNO$_3$ (O1) and one at ~ 0.75 V vs Ag/AgNO$_3$ (O2). The peak potentials do not shift with the size of the NP, but the magnitude of the current varies significantly with size. In fact, the signal increases as the size of the NP increases, which correlates to the increase in NP surface coverage with increasing the NP size that was observed in the SEM data (see Fig 2.1).

Because the strength of the peak at 0.50 V vs Ag/AgNO$_3$ (O1) varied significantly with the particular batch of NPs and the surface ligand, it is assigned to surface states of the CdTe

NPs. This peak was not observed in cases where thiol-capped CdTe NPs[20] were directly synthesized with thiol ligands and used in the voltammetry studies (see Figure A6), rather than ligand exchange from TDPA capped NPs. Ligand exchange (Scheme 2.2) from TDPA to DT does not remove this peak, and likely indicates that the ligand exchange may not be complete. It is important to note that the ligand exchange and different syntheses gave the same peak potential for O2. These observations are consistent with the view that thiol ligands suppress the interband surface states of the CdTe NPs. A similar observation and assignment was reported by Gaponik and coworkers.[21] Lastly, we note that the separation of 0.25 V between the peaks O1 and O2 agrees well with the energy separation (~ 0.30 eV) between the surface states and the valence band for CdTe NPs that was reported by Bawendi et al.[17b]

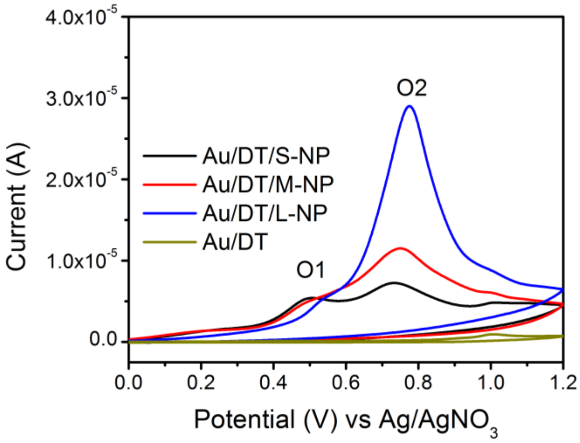

Figure 2-6. This figure shows the voltammetry measurement in acetonitrile for the assembly of Au/DT/S-NP, Au/DT/M-NP, Au/DT/L-NP, and Au/DT.

The peak at 0.75 V vs Ag/AgNO$_3$ (O2) is assigned to the oxidation of the filled valence band of the NPs, and its onset oxidation potential probes the HOMO level of the NPs. Because the HOMO is the valence band maximum (or edge), it should be the first state oxidized in the voltammetry measurement, in the absence of surface states.[22] Because that the onset potential for the peak O2 overlaps with the peak O1 from the surface states, three steps were performed to determine it. First, the peaks O1 and O2 were extracted from the measured voltammogram by subtracting a simulated baseline from the oxidation wave of Au/DT/NP (see Figure A7 for details). The subtraction results are shown as the solid curves in Figure 2.7A-C for the three Au/DT/NP assemblies. Second, the energy distribution of the surface states O1 were assumed to be Gaussian-distributed. This assumption allowed a Gaussian distribution function (dash-dotted line in Figure 2.7A-C) to be fit to the peak O1, and then subtracted from the voltammogram to isolate the peak O2 (dashed curve in Figure 2.7). These data reveal a sharp onset for the O2 wave (see Figures 2.7D-F), which allowed the onset potential to be determined by a linear extrapolation (green lines) to zero current. The results in Fig. 2.7D-F show that the oxidation for the three sizes of the NPs all start at about 0.5 ± 0.1 V; thus, their HOMO is pinned at about 0.5 V vs. Ag/$AgNO_3$. By taking the absolute electrode potential of Ag/$AgNO_3$ in acetonitrile to be 4.7 eV,[23] the onset oxidation potential ($\mathrm{E_{ox}}$) can be converted to the HOMO energy versus vacuum ($\mathrm{E_{HOMO}}$) by way of the equation: $\mathrm{E_{HOMO}} = -[\mathrm{E_{ox}} + 4.7]$ eV. The HOMO pinning energy, relative to the vacuum level, that is derived from the voltammetry measurement is -5.2 ± 0.1 eV, and it is in good agreement with that measured from PES (-5.1 ± 0.1 eV). The ~ 0.1 eV difference may be caused by solvation and other interfacial effects that are present in the voltammetry measurement, but not in the PES measurement.

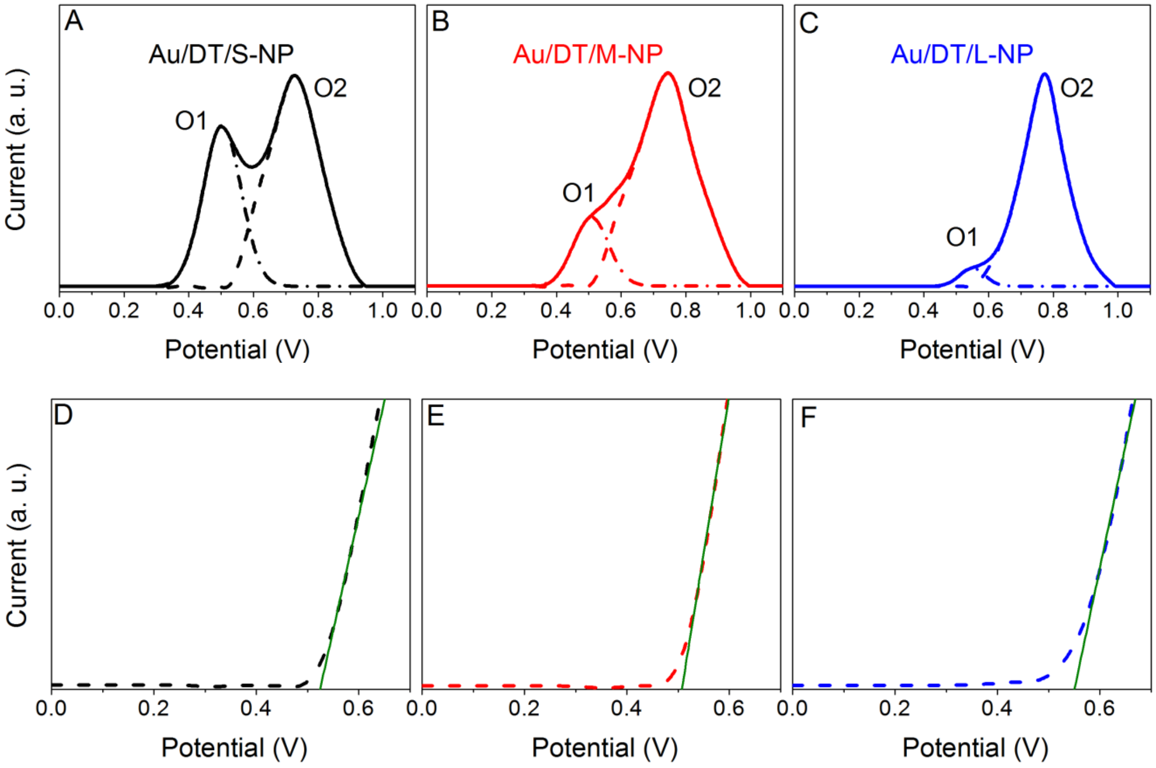

Figure 2-7. Panels A to C show the extraction of peak O2 from the oxidation wave for the assembly of Au/DT/S-NP (black), Au/DT/M-NP (red), and Au/DT/L-NP (blue). The solid curves are the oxidation wave after subtracting the simulated baseline (see Figure A7); the dash-dotted curves are the Gaussian distribution used to fit peak O1; the dashed curves are the results after subtracting the dash-dotted curve from are normalized to the corresponding peak current of the O2.

Attempts to measure the NP reduction potential proved challenging and somewhat irreproducible. Several other groups have also reported the absence of reduction signal in their voltammetry experiments for CdSe NPs.[24] We also note that the oxidation of the NP is very irreversible even when a hole scavenger, such as triethanolamine, is present in the solution.

2.3.3 Photocurrent studies

If DT ligand exchange reduces the charge recombination rates in the NPs, then it should enhance the charge transfer through NP films. The impact of the DT ligand exchange on the charge carrier transport was assessed by photocurrent measurements of the monolayer assemblies in an electrochemical cell. Figures 2.8A and 2.8B show the current density-time (*J*-t) characteristics for the Au/DT/M-NP and Au/DT/M-NP/DT assemblies. It is apparent that the photocurrent produced by Au/DT/M-NP/DT is much higher than that of Au/DT/M-NP under the same bias voltage. In Figure 2.8C, the light-off current (dark current) is subtracted from each corresponding *J*-t characteristic in Figures 2.8A and 2.8B to obtain the photocurrent density-voltage (*J*-V) characteristic. These data show that the photocurrent for the Au/DT/M-NP/DT assemblies is at least four times higher than that for the corresponding Au/DT/M-NP assemblies. Similar results were reproduced for different NP coverages on the Au electrode (see Fig S2.8). This observation further supports the conclusion that the DT molecules extend the NP exciton lifetime, and therefore improve the photoconductivity of the NP film.

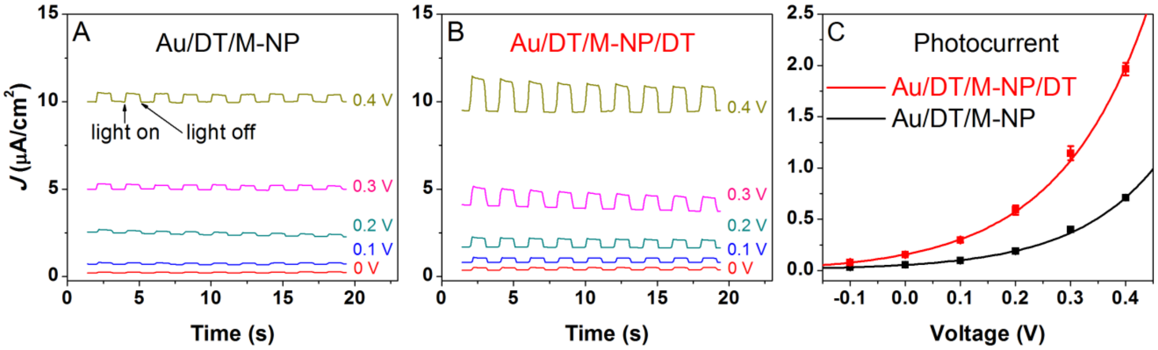

Figure 2-8. Panels A and B compare the current-time (*J*-t) characteristics for the assemblies of Au/DT/M-NP and Au/DT/M-NP/DT at various voltages (3h incubation time for the NP). Panel C shows the photocurrent-voltage (*J*-V) characteristics of Au/DT/M-NP (black points) and

Au/DT/M-NP/DT (red points). Lines connecting points serve a guide for the eyes. Some error bars are smaller than the symbol.

A simple Schottky barrier (diode) model was able to fit the photocurrent data (see Fig S2.9) for the assemblies of Au/DT/M-NP and Au/DT/M-NP/DT. The Schottky barrier heights ($\Delta\phi$) that were extracted from the fitting (see in Table A1) indicate that the ligand exchange from TDPA to DT slightly reduces the Schottky barrier height for electron transfer from the NP to the Au electrode.

2.4 DISCUSSION

2.4.1 Why is the HOMO pinned?

When a semiconductor and a metal substrate are brought into contact, charge rearranges until the Fermi levels of the semiconductor and the metal coincide. This charge rearrangement creates an electrical field across the interface.[6] For realistic systems with a high density of surface states this charge rearrangement can be dominated by changes in charge population of the surface states over a narrow band of energies. Thiol-coated gold electrodes have a high density of surface states at energies of about 1.2 to 1.6 eV below the Fermi level.[6,25] We postulate that these surface states couple strongly with the nanoparticle states and set the final energy position for the HOMO with respect to the Au Fermi level. A quantitative model for this effect should account for the electric field that is generated between the NP and the Au, and it should account for the electronic coupling between the NP and the Au, which can affect the NPs electronic confinement. If the HOMO couples more strongly to the substrate than the LUMO, then the

LUMO states of the NP remain more localized. As Brus[26] has pointed out this implies an increase of the effective mass of the hole (electrons) in the HOMO (LUMO). Thus, the effective mass of the electron is smaller than what one might expect from comparing the effective mass of the electron and the hole in the unbound NPs.

2.4.2 Why onset potential?

Because the semiconductor nanoparticle (NPs) assemblies do not display reversible redox waves, the averaging of oxidation and reduction waves to determine the formal potential of the NP cannot be used. The often asymmetric voltammograms of the NPs indicate that their redox reaction is highly irreversible. In addition, it has been noted by Bard and coworkers[22a] that the oxidation of the NPs can be a multi-charge transfer process, in which the second charge injected into the NPs from the electrode must overcome the “Coulomb blockade” from the first charge injected. Given these constraints, the onset oxidation potential provides a reasonable and clear method for estimating the energy required for the first charge injected into the HOMO level of the NPs in the ground state. Another important reason for using the onset potential for the HOMO is the poor electrochemical stability of the NPs. Several groups have reported that the electrochemical charge injected into the NPs, subsequently undergoes a fast coupled chemical reaction (an EC reaction) related to NP decomposition,[19,27] such as, $\mathrm{CdTe} \rightarrow \mathrm{Cd}^{2+} + \mathrm{Te}^{0} + 2\mathrm{e}^{-}$. This fact can be visualized by comparing the LEPET energy distribution with the voltammogram for the CdTe NPs used in this work, as shown in Figure 2.9. It is apparent that these two distributions do not agree with each other except near the onset region. Comparing the width of these two distributions suggests that the voltammetry does not reveal the full distribution of the electronic states in the NPs. For these reasons, the onset oxidation potential was used to quantify the HOMO energy of the NPs.

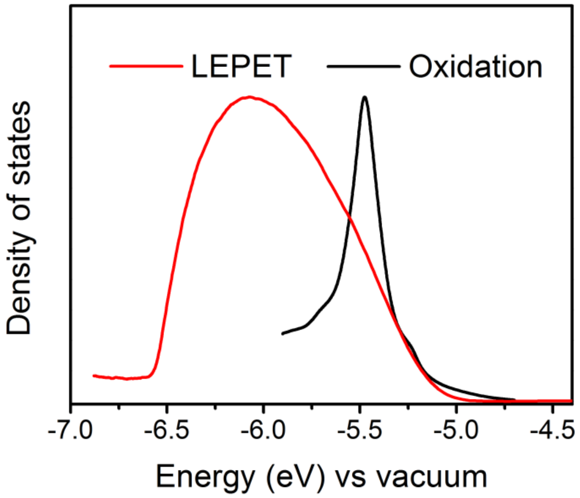

Figure 2-9. The comparison of approximated density of electronic states obtained from LEPET (red line) and the voltammetry (black line) measurements for the large CdTe NPs used in this work. Using the data for the medium/small CdTe NPs or the CdSe NPs will give similar results.

In our earlier report on CdSe NPs,[6] the peak oxidation potential was used to calculate the HOMO energy, and this choice created a difference of ~ 0.3 eV between the PES and voltammetry results. However, if the onset oxidation potential is used rather than the peak potential, the agreement between the PES and voltammetry measurements of the HOMO energy is much better. Figure 2.10 shows that the HOMO pinning level measured from the onset oxidation potentials (black open circles) is only about 0.1 eV lower than that from the PES (black filled squares) for the CdSe NPs. Figure 2.10 also compares the band edge energies (HOMO/LUMO) for CdSe (data in black) and CdTe (data in red) NPs. These data demonstrate the good agreement between the PES (filled squares) and voltammetry (open circles) measurements. These data reveal that the HOMO energies of the immobilized CdSe and CdTe NPs are independent of the NP size (for sizes greater than 2.8 nm and less than 6 nm), while the

LUMO energies shift systematically with the NP size over this same size range. The solid curves are fits of the data to a power law (see supplemental information), which can be helpful for predicting the LUMO/HOMO energies and band gaps for the CdSe and CdTe NPs.

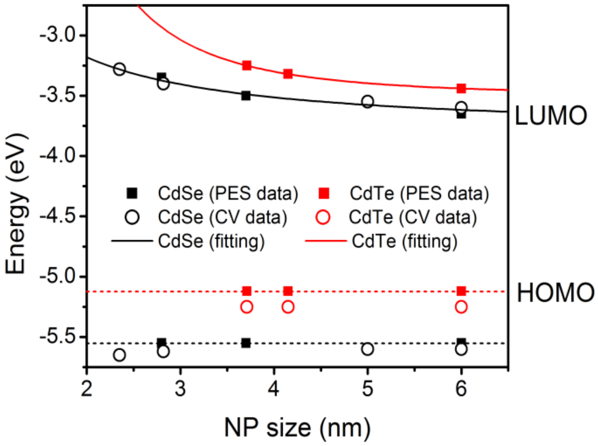

Figure 2-10. This figure shows the comparison of the energetics (HOMO/LUMO) for the CdSe (data in black) and CdTe NPs (data in red). The filled squares are results from the PES measurements, and the open circles are ones from the voltammetry. The dash lines are the HOMO pinning level determined from PES; and the solid lines are the fitting to the LUMO energies.

The data in Fig 2.10 reveal that CdSe NPs and CdTe NPs can be used to form a type-2 heterojunction. This fact is in agreement with earlier reports.[2a,2b,12,28] While the results in Figure 2.10 agree with the photoemission data in reference 14 for CdSe NPs, we note that they indicate that the HOMO (-5.55 eV) for the CdSe NPs is higher than CdSe bulk valence band edge (-5.7 eV). In addition, the band edge positions for the CdSe and CdTe NPs do not show a similar behavior with respect to their bulk energetics. This feature of the observations poses a challenge for theoretical models and calculations.

2.5 CONCLUSION

This work used photoelectron spectroscopy (PES) and electrochemistry to measure the electronic states of CdTe NP assemblies on Au electrodes. The measurements revealed that the HOMO energy of the NPs is fixed while the LUMO energy of the NPs changes with NP size, over a range from 3.7 nm to 6.0 nm. The electrochemical and photoelectron determinations of the HOMO energies were found to agree with one another to within ~ 100 mV. Two photon PES measurements and photocurrent measurements were used to show that thiol capping ligands reduce the recombination rate of charge carriers in CdTe NPs.

2.6 REFERENCES

(1) Anikeeva, P. O.; Halpert, J. E.; Bawendi, M. G.; Bulovic, V. *Nano Letters* **2007**, *7*, 2196.

(2) a) Gur, I.; Fromer, N. A.; Geier, M. L.; Alivisatos, A. P. *Science* **2005**, *310*, 462; b) Wang, Y.; Wang, L.; Waldeck, D. H. *Journal of Physical Chemistry C* **2011**, *115*, 18136; c) Huynh, W. U.; Dittmer, J. J.; Alivisatos, A. P. *Science* **2002**, *295*, 2425.

(3) Burda, C.; Chen, X. B.; Narayanan, R.; El-Sayed, M. A. *Chem. Rev.* **2005**, *105*, 1025.

(4) Buhbut, S.; Itzhakov, S.; Tauber, E.; Shalom, M.; Hod, I.; Geiger, T.; Garini, Y.; Oron, D.; Zaban, A. *Acs Nano* **2010**, *4*, 1293.

(5) Luther, J. M.; Law, M.; Beard, M. C.; Song, Q.; Reese, M. O.; Ellingson, R. J.; Nozik, A. J. *Nano Letters* **2008**, *8*, 3488.

(6) Markus, T. Z.; Wu, M.; Wang, L.; Waldeck, D. H.; Oron, D.; Naaman, R. *Journal of Physical Chemistry C* **2009**, *113*, 14200.

(7) Xie, Z. T.; Markus, T. Z.; Gotesman, G.; Deutsch, Z.; Oron, D.; Naaman, R. *Acs Nano* **2011**, *5*, 863.

(8) Carlson, B.; Leschkies, K.; Aydil, E. S.; Zhu, X. Y. *Journal of Physical Chemistry C* **2008**, *112*, 8419.

(9) Timp, B. A.; Zhu, X. Y. *Surface Science* **2010**, *604*, 1335.

(10) Sze, S. M. N., K. K. *Physics of Semiconductor Devices*; 3rd ed.; Wiley, 2007.

(11) Haram, S. K.; Kshirsagar, A.; Gujarathi, Y. D.; Ingole, P. P.; Nene, O. A.; Markad, G. B.; Nanavati, S. P. *Journal of Physical Chemistry C* **2011**, *115*, 6243.

(12) Jasieniak, J.; Califano, M.; Watkins, S. E. *Acs Nano* **2011**, *5*, 5888.

(13) Soreni-Hararl, M.; Yaacobi-Gross, N.; Steiner, D.; Aharoni, A.; Banin, U.; Millo, O.; Tessler, N. *Nano Letters* **2008**, *8*, 678.

(14) Yu, W. W.; Wang, Y. A.; Peng, X. G. *Chemistry of Materials* **2003**, *15*, 4300.

(15) Yu, W. W.; Qu, L. H.; Guo, W. Z.; Peng, X. G. *Chemistry of Materials* **2003**, *15*, 2854.

(16) Naaman, R.; Sanche, L. *Chem. Rev.* **2007**, *107*, 1553.

(17) a) Wuister, S. F.; Donega, C. D.; Meijerink, A. *Journal of Physical Chemistry B* **2004**, *108*, 17393; b) Geyer, S.; Porter, V. J.; Halpert, J. E.; Mentzel, T. S.; Kastner, M. A.; Bawendi, M. G. *Physical Review B* **2010**, *82*, 155201.

(18) Markus, T. Z.; Daube, S. S.; Naaman, R. *The Journal of Physical Chemistry B* **2010**, *114*, 13897.

(19) Haram, S. K.; Quinn, B. M.; Bard, A. J. *Journal of the American Chemical Society* **2001**, *123*, 8860.

(20) Rogach, A. L.; Franzl, T.; Klar, T. A.; Feldmann, J.; Gaponik, N.; Lesnyak, V.; Shavel, A.; Eychmuller, A.; Rakovich, Y. P.; Donegan, J. F. *Journal of Physical Chemistry C* **2007**, *111*, 14628.

(21) Poznyak, S. K.; Osipovich, N. P.; Shavel, A.; Talapin, D. V.; Gao, M. Y.; Eychmuller, A.; Gaponik, N. *Journal of Physical Chemistry B* **2005**, *109*, 1094.

(22) a) Ding, Z. F.; Quinn, B. M.; Haram, S. K.; Pell, L. E.; Korgel, B. A.; Bard, A. J. *Science* **2002**, *296*, 1293; b) Zhong, H. Z.; Lo, S. S.; Mirkovic, T.; Li, Y. C.; Ding, Y. Q.; Li, Y. F.; Scholes, G. D. *Acs Nano* **2011**, *4*, 5253; c) Li, Y. C.; Zhong, H. Z.; Li, R.; Zhou, Y.; Yang, C. H.; Li, Y. F. *Advanced Functional Materials* **2006**, *16*, 1705.

(23) By using the work function of ferrocene (4.8 eV) and the redox potential (0.1 V) of Ag/$AgNO_3$ vs. ferrocene, the work function of Ag/$AgNO_3$ is calculated to be 4.7 eV.

(24) a) Myung, N.; Ding, Z. F.; Bard, A. J. *Nano Letters* **2002**, *2*, 1315; b) Zotti, G.; Vercelli, B.; Berlin, A.; Chin, P. T. K.; Giovanella, U. *Chemistry of Materials* **2009**, *21*, 2258.

(25) Alloway, D. M.; Hofmann, M.; Smith, D. L.; Gruhn, N. E.; Graham, A. L.; Colorado, R.; Wysocki, V. H.; Lee, T. R.; Lee, P. A.; Armstrong, N. R. *The Journal of Physical Chemistry B* **2003**, *107*, 11690.

(26) Brus, L. E. *Journal of Chemical Physics* **1984**, *80*, 4403.

(27) Chen, S. W.; Truax, L. A.; Sommers, J. M. *Chemistry of Materials* **2000**, *12*, 3864.

(28) Wu, M. Y.; Mukherjee, P.; Lamont, D. N.; Waldeck, D. H. *Journal of Physical Chemistry C* **2010**, *114*, 5751.

(29) Sze, S. M. *Physics of Semiconductor Devices*; 2nd ed.; Wiley, 1981.

(30) a) Shah, J. M.; Li, Y. L.; Gessmann, T.; Schubert, E. F. *Journal of Applied Physics* **2003**, *94*, 2627; b) Kroon, M. A.; van Swaaij, R. *Journal of Applied Physics* **2001**, *90*, 994.

3.0 ELECTROCHEMICALLY-GUIDED PHOTOVOLTAIC DEVICES

This work has been published as Wang, Y.; Wang, L.; Waldeck, D. H. *Journal of Physical Chemistry C* **2011**, 115, 18136. The thesis author conducted all the experiments and prepared the manuscript.

This work reports on the energy level alignment and charge transfer in organized assemblies of CdTe and CdSe nanoparticles (NPs), for both electrochemical systems and in solid state photovoltaic devices. This work shows how control over the energy level alignment by manipulation of the size and surface ligands of the CdTe and CdSe NPs, can be combined with control over the NPs spatial arrangement, either by sequential self-assembly onto a Au working electrode of an electrochemical cell or spin-coating onto an ITO substrate of a photovoltaic device, to facilitate photoinduced charge separation (photocurrent). By combining spatial and energetic hierarchy of the assemblies the charge transfer direction and its efficiency can be optimized.

3.1 INTRODUCTION

Compared to the traditional silicon solar cells, bulk heterojunction (BHJ) solar cells offer advantages of low cost, easy fabrication, and good portability. To date, the organic BHJ solar cells have been able to achieve the power conversion efficiency (PCE) around ~8 % [1]. For organic semiconductors, polymeric electron donors, such as P3HT (poly(3-hexylthiophene)), are generally used with the fullerene electron acceptors, like PC61BM (Phenyl C61 butyric acid methyl ester), to fabricate bulk heterojunction (BHJ) solar cells [2]. Organic BHJ solar cells typically suffer from high bandgap, a large energy offset between the electron donor and electron acceptor conduction band levels, and low carrier mobility [3]. Nanocrystal semiconductor (NCS) based solar cells and/or NCS/polymer composite solar cells offer possible solutions to the above problems. Because the bandgap of NCSs are strongly dependent on composition and are size-tunable, they can be adjusted to minimize the energy offset between the electron donor and electron acceptor conduction band levels. At the same time they can be adjusted to maximize the light absorption. In addition, similar to organic semiconductors, NCSs can also be fabricated into thin film devices by solution casting methods [4].

Among the various NPs, cadmium chalcogenides (CdS, CdSe, CdTe) are one of the most well-studied families. Their synthesis, size/shape control, and optoelectronic properties are better established than those of other families. By using different sizes of CdSe nanoparticles NPs (small, medium, and large), Bawendi and Whitesides et al reported that the photocurrent contribution from each size of the NPs was highly dependent on their relative spatial arrangement because of their energy gradient[5]. More interestingly, CdTe and CdSe NPs can form an electron donor and electron acceptor pair, i.e., a type-II heterojunction, that facilitates charge separation and reduces the charge recombination between the NPs. Their electron donor/acceptor relationship has been reported by several groups[6]. By using surface photovoltage spectroscopy, Rogach et al reported that the spatial arrangement between the CdTe and CdSe NPs can also affect their charge transfer directionality[6b]. To our knowledge, however, no direct photocurrent evidence for this directionality of charge transfer between CdTe and CdSe NPs has been reported.

This work reports on the direct measurement of the directional photocurrent generated by CdTe and CdSe NPs in two different thin film assemblies and examines its dependence on the energy level alignments. In the first system, CdTe and CdSe NPs were sequentially self-assembled onto an Au-ball electrode to form a type-II heterojunction and their photoelectrochemical properties were studied. In the second type of system, CdTe and CdSe NPs were fabricated into a thin-film photovoltaic device with a planar type-II heterojunction and its photocurrent performance was characterized by their current-voltage (I-V) characteristic. The two systems give qualitatively similar results and their comparison clearly demonstrates the importance of the energy level alignment through space (NP order) for enabling efficient photocurrent generation.

3.2 EXPERIMENTS

3.2.1 Materials

Cadmium oxide and trioctyl phosphine (TOP) were purchased from Strem Chemicals. Octadecylphosphonic acid (ODPA) was purchased from PCI synthesis. All of the other chemicals were purchased from Sigma Aldrich without further purification unless mentioned otherwise.

3.2.2 NP synthesis

All syntheses were conducted by the method developed by Zhang [7] and Peng [8]. CdTe and CdSe NPs were made separately by the well-known hot-injection method. Briefly, for oleylamine capped CdSe (OA-CdSe) NPs, the cadmium precursor was prepared by dissolving 0.3 mmol CdO in 0.5 ml oleic acid and 2.5 ml 1-octadecene (ODE) at 250 °C. The selenium precursor was prepared by dissolving 0.315 mmol Se in 0.15 ml TOP, to which 3 ml oleylamine (OA) was added. At 300 °C, the selenium precursor was quickly injected into the cadmium precursor to start the reaction. After the injection, the reaction temperature was lowered to 280 °C for the NP growth. Similarly, ODPA-CdTe NPs were synthesized by hot-injecting a tellurium precursor (0.2 mmol Te/ 0.28 ml tributyl phosphine (TBP)/ 3 ml ODE) into the cadmium precursor (0.3 mmol CdO/ 0.6 mmol ODPA/ 2.5 ml ODE) at 300 °C. Then, its reaction temperature was lowered to 260 °C for the NPs growth. The sizes of NPs were controlled by the duration of the reaction. After reaching the desired size, the reaction vessel was removed from the heating mantle and allowed to cool down to room temperature. Subsequently, the NPs/ODE mixture was moved into an Ar-filled glove box for purification. To the mixture, excess acetone was added to precipitate the NPs. After centrifugation and decantation, the NP precipitate was re-dissolved in toluene, precipitated by methanol, and then obtained again by centrifugation and decantation. This process was repeated once and the final NPs were dried by Ar. For device fabrication, the reactions were scaled up by a factor of five.

3.2.3 Ligand exchange to pyridine

If ligand exchange was necessary, the as-prepared NPs were refluxed in 15 ml pyridine overnight. Next morning, the pyridine-NPs were precipitated by excess hexane, washed by toluene once, and dried under Ar. Then, they were re-dissolved in 1-2 ml pyridine and made ready for use.

3.2.4 Electrochemical measurement

A Au ball electrode was made by heating the tip of an Au wire in the H_2/O_2 flame. Its surface area was ~3 mm^2. To immobilize NPs on the surface of the Au ball electrode, the electrode was incubated overnight in a 5 mM ethanol solution of 1,10-decanedithiol (-) to form a dithiol self-assembled monolayer (SAM). The next morning, the SAM-modified electrode (Au-) was rinsed with ethanol and dried under Ar. Then, it was placed into an as-prepared NP solution for 6 hours to form a Au electrode-NPs assembly (Au-NPs). After that, the electrode was rinsed with the solvent and dried by Ar. If a bilayer sample was needed, the electrode was put into the dithiol solution again under the same condition to grow another layer of dithiol SAM on the top of the first NP layer (Au-NPs-). After the same rinsing/drying, this electrode was immersed into another NP solution to get the second layer of NPs (Au-NPs-NPs). The chemically modified Au ball electrode served as the working electrode in a 3-electrode cell, which also included a Pt counter electrode and an $Ag/AgNO_3$ reference electrode (0.54 V vs NHE). The supporting electrolyte was 100 mM acetonitrile solution of tetrabutylammoniumhexafluorophosphate ($TBAPF_6$). For the photocurrent measurement, trienthanolamine (TEA), a hole scavenger, was added into the supporting electrolyte solution with a concentration of 20 mM. The illumination was provided by a 75 W Xe arc lamp that was coupled with a multimode optical fiber. This fiber offered an illumination area of 7 mm^2. This illumination was chopped at 0.1 Hz by a motorized shutter. The working distance was fixed at 2.54 cm.

3.2.5 Device fabrication and characterization

Before thin film fabrication, every NP/pyridine solution was well sonicated and passed through Millipore Teflon syringe filters with a 450nm pore size. Next, a poly(3,4-ethylenedioxythiophene):poly(styrenesulfonate) (PEDOT:PSS) was spin coated onto the patterned ITO (the anode, purchased from Ossila) at 4000 rpm and baked at 120 °C for 2 min. Then, in a glove box, CdTe or CdSe NP/pyridine solutions were separately spin coated directly on top of the PEDOT:PSS layer at 1500 rpm and baked at 150 °C for 10 min. The spin coating order was either CdTe-CdSe or CdSe-CdTe. The AFM thickness measurement showed that the incoming NP layer did not re-dissolve the pre-spun NP layer. A 100 nm thick Al film (the cathode) was deposited onto the film through a shadow mask in an Ultek E-beam Evaporator at a rate of 1 Å/s. Six active areas were made on one substrate and each of them had a surface area of 4.5 mm^2. In the end, the device was encapsulated by an UV-curable optical epoxy (procedure performed under inert atmosphere) and was then ready for testing under ambient conditions.

The optical density (O. D.) of thin films was measured by a Craic UV-Vis-NIR microspectrophotometer. The thickness of the PEDOT:PSS layers was measured by a Horiba Jobin Yvon Uvisel ellipsometer. For the films with NPs, a tapping-mode AFM (Veeco) was used to determine their thickness. The current-voltage characteristics of the devices were measured by a CHI 618B potentiostat. A 75 W Xenon arc lamp was filtered to provide an illumination of AM 1.5G (100 mW/cm^2), which was calibrated by a pre-calibrated Si photodiode (NIST traceable).

3.3 RESULTS AND DISCUSSIONS

3.3.1 Nanoparticle (NP) synthesis

The NPs of CdTe and CdSe were size-selectively synthesized by the methods developed by Zhang et al [7] and Peng et al [8]. Figure 3.1A shows the steady-state absorption and photoluminesence (PL) spectra for the CdTe and CdSe NPs used in this work. The first excitonic peak of CdTe NPs occurred at 612 nm and that for the CdSe NPs occurred at 619 nm. Their sizes were determined by analyzing more than 100 nanoparticles in the TEM images and fitting of the distribution of diameters (Figure 3.1B-E). The resultant diameter was 4.11 ± 0.30 nm for CdTe NPs and 5.24 ± 0.34 nm for CdSe NPs.

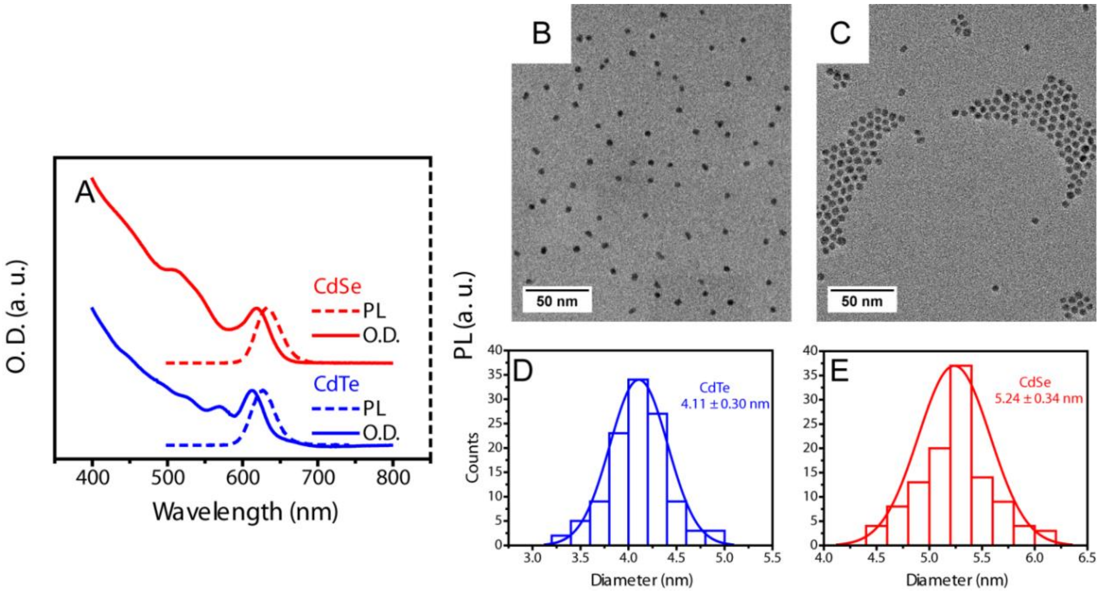

Figure 3-1. Panel A shows the steady-state absorption and photoluminesence (PL) spectra for CdTe NPs (blue) and the CdSe (red). Panels B and C show a TEM image for CdTe and CdSe NPs. Panels D and E show the size distribution for CdTe and CdSe NPs shown in Panels B and C.

3.3.2 Electrochemical system

Because the oxidation and reduction peak can be directly correlated to the charge transfer at the HOMO and LUMO of the NPs. Cyclic voltammetry (CV) was used to determine the bandgap and the energy level position of NPs [9]. Figure 3.2 shows the voltammetry measurement for single layers of NPs that were immobilized onto a Au electrode, Au-CdTe (blue solid) and Au-CdSe (red solid); the voltammograms have the dithiol SAM (Au-) background current subtracted. The oxidation peaks of the CdTe NPs and the CdSe NPs are observed at 0.89 V and 1.06 V (vs. Ag/AgNO$_3$) at a scan rate of 50 mV/s. For more details about this sort of determination, see references [10]. In the voltammetry of the Au-CdTe assembly, the broad oxidation peak from 0.4 V to 0.6 V is attributed to the trap states on the NP surface [11].

Figure 3.2 shows voltammetry results for the NP bilayer electrodes, Au-CdSe-CdTe (purple dash) and Au-CdTe-CdSe (green dash), also. Both the oxidation peak of CdTe and CdSe can be clearly observed at their typical position, regardless of the NPs order of assembly. These data prove that the bilayer architecture is successfully assembled onto the Au ball electrode. Note that a ~50 mV shift in the oxidation peak position of CdTe and a ~20 mV shift in the oxidation peak position of CdSe are observed between the two different bilayer assemblies. Compared to the oxidation peak position of the single layer assemblies, the shift occurs for NPs that are located in the inner layer (between the electrode and the outermost NP layer). This shift appears to be caused by the difference in the surface coverage of the dithiol linker on the inner and the outer NP layer. This hypothesis was verified by examining the voltammetry results for single NP layers in which the assemblies had natively terminated NPs (single layer voltammograms of Figure 3.2) and assemblies that were further exposed to dithiol in order to coat the outer surface (data are not shown). These latter assemblies showed the potential shift that is found in the bilayer studies. This result is also consistent with other findings. One expects that the inner NP layer should have a higher dithiol coverage than the outer one, and it has been shown that changing the surface ligand can affect the energetics of the NPs [12].

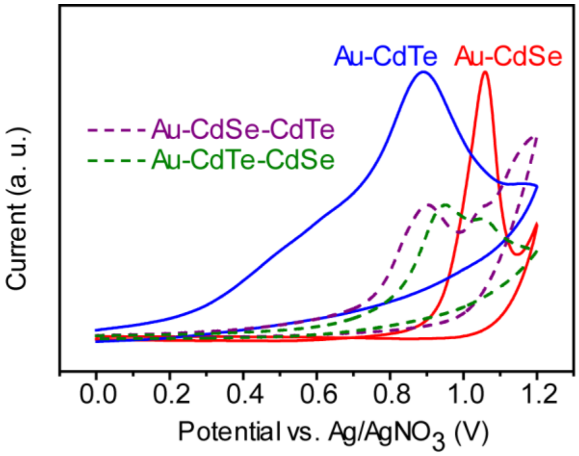

Figure 3-2. The figure shows cyclic voltammogram results for Au-CdTe (blue solid), Au-CdSe (red solid), Au-CdSe-CdTe (purple dash), and Au-CdTe-CdSe (green dash).

By using the average measured size of the NPs, the bandgaps of CdTe and CdSe NPs were calculated by a tight-binding model [13] and were found to be 2.07 eV and 2.04 eV for the CdTe and CdSe NPs, respectively. By assigning the oxidation peak position of the NPs to the HOMO energy level position, the LUMO energy level of the NPs can be calculated from the bandgap of the NPs. Using these energies, the resultant energy level positions for CdTe and CdSe NPs were calculated and used to make the plots in Figure 3.3. Panels A and B of Figure 3.3 show the energy level alignments for the two different orderings of NPs in the bilayers: Au-CdSe-CdTe and Au-CdTe-CdSe. Because it does not have the charge transfer barrier between the CdTe and CdSe NPs, it is evident that the energetic alignment of Au-CdSe-CdTe should facilitate electron transfer to the Au electrode better than the Au-CdTe-CdSe assembly does.

Triethanolamine (TEA) has a redox potential of 0.63 V vs. Ag/AgNO3 and is used here as a hole scavenger to transfer the photogenerated hole to the counter electrode. The use of TEA creates an efficient path for the hole transfer to the solution, and blocks the electron transfer to the solution.

In Figure 3.3C and 3.3D, the current-time (I-t) characteristic is shown at different potentials for the two different bilayer assemblies. By using a Xe arc lamp, the light illuminates the electrode and is chopped at a frequency of 0.1 Hz. Each measurement is run for 150 s, and the illumination time is 50 s. The same electrode was used to obtain at least five I-t characteristics at different potential values; thus, the total illumination time for each electrode was at least 250 s. During this measurement period, the bilayer assemblies showed a stable photoresponse, and both their dark current and the photocurrent increased as the potential bias increased. In Figure 3.3E, the background dark current was subtracted from each corresponding I-t characteristic in Figure 3.3C and 3.3D to obtain the photocurrent-voltage (I-V) characteristic. The curves through the data points are intended as a guide to the eye. The photocurrent generated by Au-CdSe-CdTe is three to four times higher than that of Au-CdTe-CdSe at the same potential. The results demonstrate that the Au-CdSe-CdTe bilayer assembly produces a higher photocurrent than does the Au-CdTe-CdSe bilayer assembly; presumably, because the Au-CdSe-CdTe assembly provides a more favorable energy architecture for electron transfer.

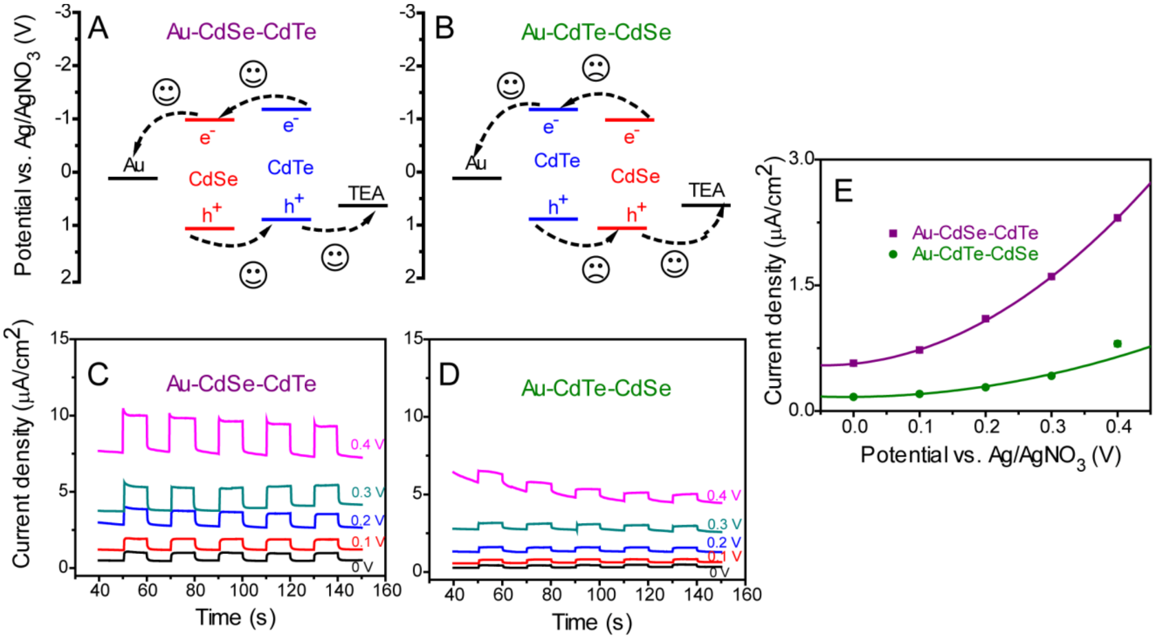

Figure 3-3. Panels A and B show the energy diagrams for the two different assembly orders. Panels C and D shows the I-t characteristics of the two different assembly orders. Panel E shows the photocurrent comparison of current-voltage characteristic of the two different assembly orders. The error bar in panel E is smaller than the symbol.

3.3.3 PV device system

The electrochemical studies of the CdTe/CdSe energy architecture indicate that the Au-CdSe-CdTe bilayer assembly is better than the reversed NP ordering for producing photocurrent. This prediction about the energy architecture was tested in an all solid-state, thin film solar cell device. Because the as-prepared CdTe and CdSe NPs are capped by long and insulating ligands that significantly increase the interparticle distance and the charge transfer resistance, the film conductance was improved by using a short and conjugated ligand, pyridine (Py). Replacement of the surface ligands was accomplished through adaptation of published procedures [14], see the experimental section. Figure 3.4C shows the absorption spectra of CdSe (red) and CdTe (blue)

NPs after ligand exchange. These spectra show that the first excitonic peaks become broader than those in Figure 3.1A. The broader spectral feature likely reflects a broader size distribution than that for the NPs materials used in the electrochemical studies. We attribute this broadening of the NP size distribution to the use of a larger-scale synthesis (by five times) for the device fabrication. In the larger batch synthesis, Ostwald ripening plays a more important role in determining the NP size-distribution during the reaction and the cooling process [15]. In addition to this effect on the distribution, it has been reported that the ligand exchange to pyridine can also broaden the absorption peak of NPs [16].

As shown in Figure 3.4A, the device fabrication starts with a patterned-ITO anode, onto which the PEDOT: PSS (PP) is spin-coated with a thickness of 40 nm. Next, NP bilayers are sequentially spin coated onto PP with the two different orders, which are PP-CdTe-CdSe and PP-CdSe-CdTe (150 nm thick in total). After spin coating, the cathode (100 nm thick Al) is deposited directly onto the NP bilayers in an e-beam evaporator. In order to avoid unnecessary oxidation on the NP surface and test the device in the air, the active areas on the device were encapsulated by an optical epoxy. In the final step, the connection legs were attached to each ITO pattern in order to make contact with the anode/cathode of the device. A photographic image of an actual device is shown in Figure 3.4B.

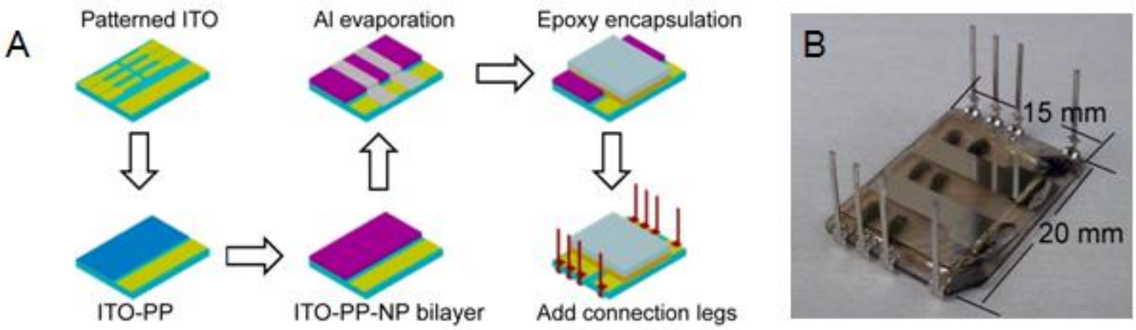

Figure 3-4. Panel (A) illustrates the procedure for the device fabrication. Panel (B) shows a photograph of the actual device with connection legs.

Absorption spectra of the devices with the two different spin coating orders were also measured, and they are presented in Figure 3.5. The devices with the PP-CdTe-CdSe (green) and the PP-CdSe-CdTe (purple) exhibit a similar absorption behavior to that of the absorption spectra of pure CdTe and CdSe NPs in solution; however, a wide absorption peak from 580 nm to 660 nm that covers the first excitonic peaks of both CdTe and CdSe NPs is apparent.

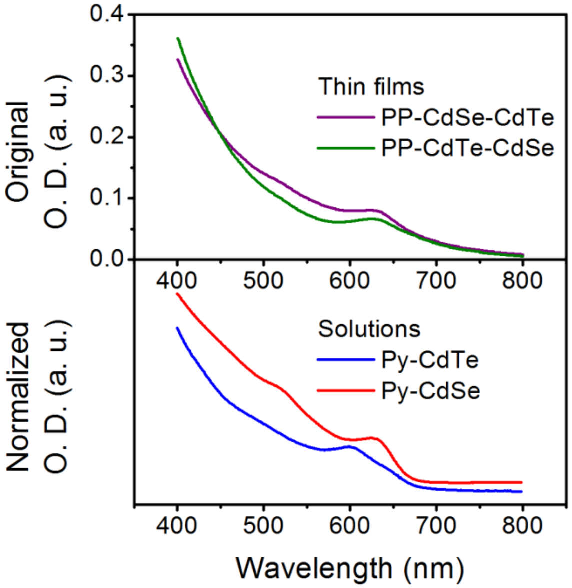

Figure 3-5. The figure shows the solution absorption spectra of CdTe and CdSe NPs after ligand exchange with pyridine in the lower graph, and the absorption spectra of the devices with the two different spin coating orders in the upper graph.

Because the PEDOT PSS (PP) is a hole-conducting (and electron-blocking) polymer, the photogenerated holes move through the PP and are collected at the ITO electrode. Concomitantly, the photogenerated electrons are transferred to the Al. The photoelectrochemical results indicate that the device with the ITO-PP-CdTe-CdSe-Al ordering (device A) should provide a better photovoltaic response than device B, which has the ITO-PP-CdSe-CdTe-Al ordering. The energy diagrams of these two devices are shown in Figures 3.6A and 3.6B. The current-voltage (I-V) characteristics of device A (green) and device B (purple), under both dark (dashed curve) and illuminated (solid curve) condition, are shown in Figures 3.6C and 3.6D. Both of the devices exhibit a photovoltaic response under illumination, but it is apparent that device A performs much better than device B. In Figure 3.6E, after the dark current subtraction, the photocurrent of device A and B are compared on the same graph and their parameters are summarized in Table 3.1. Device A produces an open circuit voltage (V_{oc}), a short circuit current (I_{sc}), and a fill factor (*FF*) that are 2, 35, and 1.3 times higher than those of device B, respectively. More importantly, the maximum power (P_{max}) generated by device A is almost 80 times higher than that of device B, as is its power conversion efficiency of 0.21%. The performance of device A exceeds the efficiency of the single-layer device consisting of CdTe or CdSe NSCs [14,17] or a CdTe/CdSe multi-branched structure[18,19].

The results for the thin film photovoltaic devices agree qualitatively with those for the electrochemical system, in how the directionality of the charge transfer between the donor, CdTe NPs ,and the acceptor, CdSe NPs, correlates with the overall charge direction of the device. The performance of the device may be improved by: 1) utilizing a short and conjugated bidentate linker, such as benzenedithiol, to shorten the inter-particle distance and to increase the film conductivity [20]; 2) annealing and sintering the NP film in the presence of $CdCl_2$ solution. It has been reported that this process can reduce the surface trap area of the NP film [14]; 3) employing a conductive polymer, like P3HT, to form a bulk heterojunction with the NP that can increase the interface for charge separation[21].

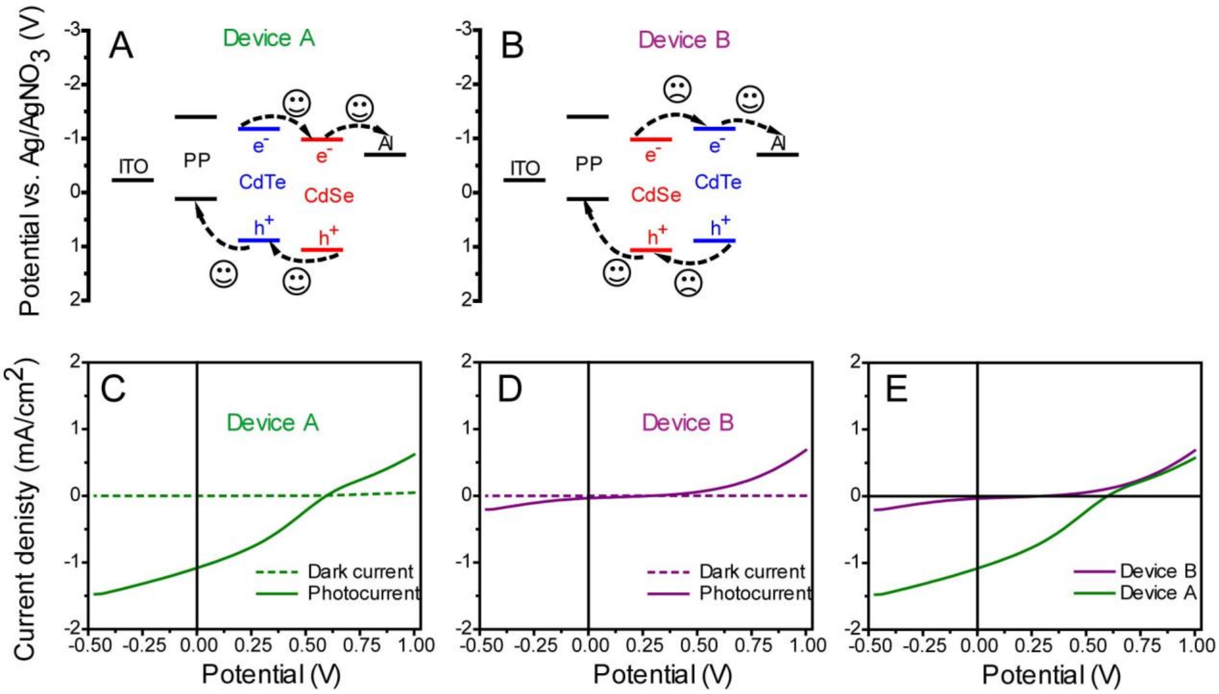

Figure 3-6. Panels A and B show the energy diagrams for Device A and B. Panels C and D show the dark current (dash) and the photocurrent (solid) of Device A and B. Panel E shows the photocurrent comparison between Device A and B after the subtraction of the dark current.

Table 3.1. PV performance of Devices A and B

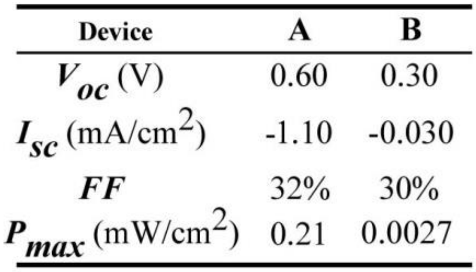

Device	A	B
V_{oc} (V)	0.60	0.30
I_{sc} (mA/cm^2)	-1.10	-0.030
FF	32%	30%
P_{max} (mW/cm^2)	0.21	0.0027

3.4 CONCLUSION

In this work electrochemical methods were used to quantify the energy level displacements in NP bilayer assemblies, and these assemblies were used as a simple model to study how the energy level alignments affect the charge transfer directionality and efficiency. The photocurrent data show that it is most favorable, for both electron and hole transfer, when the donor-CdTe was near the hole scavenger-TEA, at the film/solution interface. This model successfully guided the design of a photovoltaic device, in which the device performed much more efficiently when the donor-CdTe was near the hole-conducting polymer-PEDOT:PSS. The correspondence between these results underscore the use of photoelectrochemical assemblies for the design of photovoltaic thin film devices and provide insights into how one can control the charge transfer directionality between CdTe NPs and CdSe NPs assemblies.

3.5 References

(1) Green, M. A.; Emery, K.; Hishikawa, Y.; Warta, W. *Progress in Photovoltaics: Research and Applications* **2011**, *19*, 84.

(2) Clarke, T. M.; Durrant, J. R. *Chem. Rev.* **2010**, *110*, 6736.

(3) Gregg, B. A.; Hanna, M. C. *Journal of Applied Physics* **2003**, *93*, 3605.

(4) Nozik, A. J.; Beard, M. C.; Luther, J. M.; Law, M.; Ellingson, R. J.; Johnson, J. C. *Chem. Rev.* **2010**, *110*, 6873.

(5) Weiss, E. A.; Porter, V. J.; Chiechi, R. C.; Geyer, S. M.; Bell, D. C.; Bawendi, M. G.; Whitesides, G. M. *Journal of the American Chemical Society* **2008**, *130*, 83.

(6) a) Wu, M. Y.; Mukherjee, P.; Lamont, D. N.; Waldeck, D. H. *Journal of Physical Chemistry C* **2010**, *114*, 5751; b) Gross, D.; Mora-Sero, I.; Dittrich, T.; Belaidi, A.; Mauser, C.; Houtepen, A. J.; Da Como, E.; Rogach, A. L.; Feldmann, J. *Journal of the American Chemical Society* **2010**, *132*, 5981.

(7) Zhong, X. H.; Feng, Y. Y.; Zhang, Y. L. *Journal of Physical Chemistry C* **2007**, *111*, 526.

(8) Yu, W. W.; Wang, Y. A.; Peng, X. G. *Chemistry of Materials* **2003**, *15*, 4300.

(9) Haram, S. K.; Quinn, B. M.; Bard, A. J. *Journal of the American Chemical Society* **2001**, *123*, 8860.

(10) Markus, T. Z.; Wu, M.; Wang, L.; Waldeck, D. H.; Oron, D.; Naaman, R. *Journal of Physical Chemistry C* **2009**, *113*, 14200.

(11) Poznyak, S. K.; Osipovich, N. P.; Shavel, A.; Talapin, D. V.; Gao, M. Y.; Eychmuller, A.; Gaponik, N. *Journal of Physical Chemistry B* **2005**, *109*, 1094.

(12) Frederick, M. T.; Weiss, E. A. *Acs Nano* **2010**, *4*, 3195.

(13) a) Sapra, S.; Sarma, D. D. *Physical Review B* **2004**, *69*; b) Kissling, G. P.; Bunzli, C.; Fermin, D. J. *Journal of the American Chemical Society* **2010**, *132*, 16855.

(14) Gur, I.; Fromer, N. A.; Geier, M. L.; Alivisatos, A. P. *Science* **2005**, *310*, 462.

(15) Murray, C. B.; Norris, D. J.; Bawendi, M. G. *Journal of the American Chemical Society* **1993**, *115*, 8706.

(16) Hanrath, T.; Veldman, D.; Choi, J. J.; Christova, C. G.; Wienk, M. M.; Janssen, R. A. J. *Acs Applied Materials & Interfaces* **2009**, *1*, 244.

(17) Ginger, D. S.; Greenham, N. C. *Journal of Applied Physics* **2000**, *87*, 1361.

(18) Zhong, H. Z.; Zhou, Y.; Yang, Y.; Yang, C. H.; Li, Y. F. *Journal of Physical Chemistry C* **2007**, *111*, 6538.

(19) Lee, H.; Kim, S.; Chung, W. S.; Kim, K.; Kim, D. *Solar Energy Materials and Solar Cells* **2011**, *95*, 446.

(20) Debnath, R.; Tang, J.; Barkhouse, D. A.; Wang, X. H.; Pattantyus-Abraham, A. G.; Brzozowski, L.; Levina, L.; Sargent, E. H. *Journal of the American Chemical Society* **2010**, *132*, 5952.

(21) Huynh, W. U.; Dittmer, J. J.; Alivisatos, A. P. *Science* **2002**, *295*, 2425.

4.0 PHOTO-INDUCED HOLE TRANSFER IN CONJUGATED COPOLYMER AND SEMICONDUCTOR NANOPARTICLE ASSEMBLIES: DRIVING CHARGE SEPARATION FOR HYBRID SOLAR CELLS

This work is in preparation for submission as Yang Wang, Kuan Liu, Prasun Mukherjee, Doug Hines, Pralay Santra, Prashant Kamat, and David H. Waldeck. The thesis author synthesized the NP; conducted photoluminescence quenching, cyclic voltammetry, and spectroelectrochemical measurements; prepared the manuscript. The supporting information for this chapter is provided in Appendix B.

Organic/inorganic hybrid photovoltaics are promising for use in next-generation solar cells, however, the interfacial charge transfer and charge separation between organic conjugated polymers and inorganic semiconductor nanoparticles still remains largely unexplored. This work reports a charge transfer study for a hybrid conjugated-copolymer/semiconductor-nanoparticle assembly by using time-resolved photoluminescence and absorption spectroscopic methods in conjunction with electrochemical and spectroelectrochemical techniques. The results show that the charge transfer rate is affected by the internal electric field at the hybrid donor-acceptor heterojunction between the copolymer and the nanoparticle. These findings suggest a strategy to enhance the exciton dissociation in hybrid devices by combining donor-acceptor energy offsets and internal electric field as a dual charge-separation driving force.

4.1 INTRODUCTION

Hybrid organic/inorganic semiconductor materials, such as p-type conjugated polymer (CP)/n-type semiconductor nanoparticle (NP) composites, are promising for use in next-generation solar cells.[1] By combining the complementary advantages of both CPs and NPs,[2] these hybrid materials provide access to a larger range of electronic and morphological properties than do either all organic or all inorganic materials. Over the past decade, a considerable amount of research effort has been spent in investigating hybrid CP/NP solar cells from a variety of perspectives, including co-solvent systems for solution processing,[3] optimizing the shape of the CP and NP nanostructures,[3-4] developing CP-grafted NPs,[5] adjusting the energy band alignment between the CP and NP,[6] exploring singlet-exciton fission processes,[7] etc. The highest power conversion efficiencies[4a] (~ 5%) reported for these hybrid devices, such as P3HT/CdSe NPs bulk heterojunction cells, are significantly lower than that for all inorganic devices and all organic devices, however. A number of workers have suggested that rapid charge recombination processes originating from a limited exciton diffusion length,[8] back charge transfer,[9] poor CP/NP contact,[10] and surface trap states[1c,11] account for much of the reduced efficiency.[12] Thus, it is important to understand and enhance interfacial charge transfer and charge separation dynamics at the organic/inorganic donor-acceptor (D-A) heterojunction, if the promise of organic/inorganic hybrid materials is to be realized.

Motivated by this challenge, the current work constructs a model CP/NP system, in which systematic charge-transfer studies are performed on mixed solutions of a novel alternating donor-acceptor low-bandgap copolymer and a CdTe semiconductor nanoparticle. While a few groups have investigated bulk heterojunction devices composed of alternating copolymers and semiconductor NPs,[13] systematic charge transfer studies for these hybrid systems are few.[14] Thus, we aim to isolate and characterize the important variables that affect charge separation and recombination processes in the model system, and provide insights for improving the efficiency for hybrid solar cells.

4.2 RESULTS AND DISCUSSION

4.2.1 Organic and inorganic components

Alternating donor-acceptor low-bandgap copolymers are selected as the organic component in this system, because they have achieved impressive power-conversion-efficiency (~ 8%) in organic photovoltaics.[15] The alternating donor-acceptor (D-A) structure employs push–pull driving forces between the donor and acceptor units, to promote the photoinduced intramolecular charge transfer, to facilitate electron delocalization, and to lower the bandgap.[15b] However, synthesis of such copolymers that are highly water-soluble has not been reported to our best knowledge. By extending previous strategies for synthesizing water-soluble conjugated polymers,[16] we report the synthesis of both anionic (-) and cationic (+) alternating D-A low-bandgap copolymers consisting of a donor unit-phenylenevinylene and an acceptor unit-diketopyrrolopyrrole (see Figure 4.1). The anionic and cationic copolymers show similar absorption spectra in DI water (Figure B4A) and have similar average molecular weights (~ 25,000, see Table B1), respectively. In addition, they do not show photoluminescence in DI water, presumably because of the intramolecular charge transfer character between the two monomer units.[17] Details of synthetic procedures and characterization for these new materials are given in the Appendix B (see Figures S1 and S2).

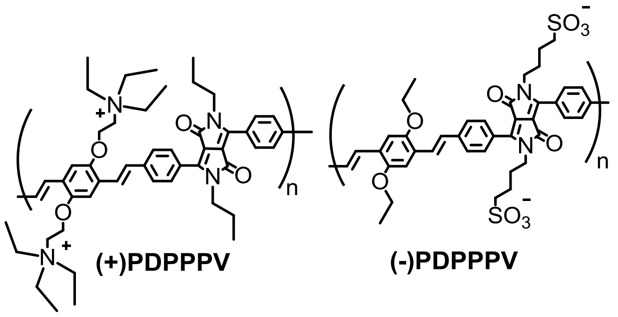

Figure 4-1. The molecular structure is shown for poly[1,4-diketo-2,5-bis(4-sulfonylbutyl)-3,6-diphenyl-pyrrolo(3,4-c)pyrrole-alt-divinyl-1,4-bis(ethyloxy)benzene sodium], denoted as, (-)PDPPPV; and Poly[1,4-diketo-2,5-dipropyl-3,6-diphenyl-pyrrolo(3,4-c)pyrrole-alt-divinyl-1,4-bis(2-(N,N,N-triethylaminium)ethoxy) benzene bromide], denoted as, (+)PDPPPV. Prefix (+) or (-) means positively or negatively charged species, respectively.

Based on previous studies and ability to control their size-dependent energetics,[18] water-soluble anionic (-) and cationic (+) CdTe semiconductor NPs were chosen to be the inorganic component in the hybrid system, The anionic and cationic NPs were prepared separately by following previously published procedures[19] (see Figure B3). Cyclic voltammetry measurements show that the CdTe NPs with optimized size-tunable energetics can form a type-II (donor-acceptor) heterojunction with the PDPPPV copolymers (Figure 4.2 and Figure B5). Interestingly, the voltammetry results show that reversing the surface charge on the NPs or the PDPPPV copolymers does not significantly change their redox potentials, within the experimental resolution. Additionally, the LUMO energy offset between the NPs and PDPPPV is around ~ 0.3 eV, which is close to an optimal difference for driving charge separation.[20]

Figure 4.2 shows that both (-)PDPPPV (blue) and (+)NPs (red) have broad absorption coverage in the visible range, which distinguishes them from the traditional organic or hybrid D-

A photovoltaic systems. Here, the energy transfer between the (-)PDPPPV and (+)NP is avoided because 1) the photoluminescence of (-)PDPPPV is quenched and 2) there is little spectral overlap between (-)PDPPPV's absorption (blue solid) and (+)NP's photoluminescence (red dash). These features allow one to exclusively study the charge transfer between the (-)PDPPPV and the (+)NP by photoluminescence (PL) quenching. Figure B4 shows that (+)PDPPPV and (-)NP, the counterpart copolymer and NP with opposite surface charges, have very similar spectra.

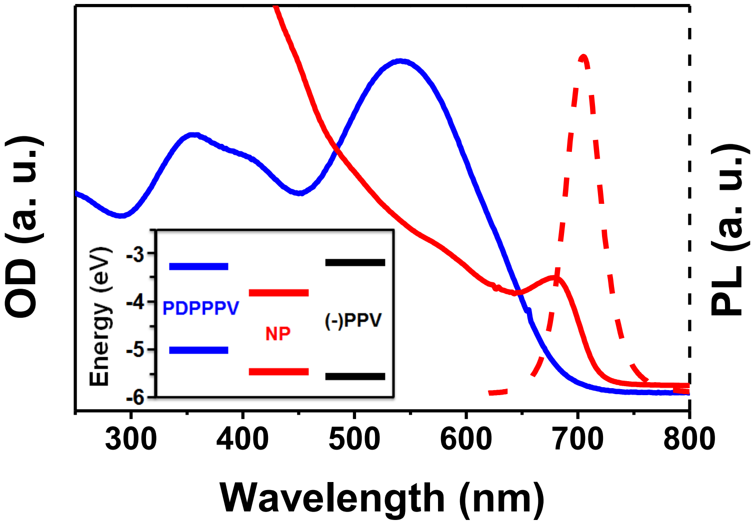

Figure 4-2. The steady-state absorbance (solid lines) and photoluminescence (dashed lines) spectra for the (-)PDPPPV (blue) and (+)NP (red) in DI water are plotted together for comparison. The inset is an energy diagram determined by cyclic voltammetry for the NPs and polymers. (-)PPV is a control polymer, vide infra.

4.2.2 Photoluminescence quenching

Figure 4.3 presents the steady-state and time-resolved PL quenching results for the assembly of (+)NP/(-)PDPPPV. Figure 4.3A shows that titrating a 3 mL pH=7 buffer solution of (+)NP (OD

~ 0.1 at 692 nm) with up to 20 μL of (-)PDPPPV solution (0.5 mg/mL) causes a 90 % PL quenching of (+)NP. The final NP/copolymer molar ratio is about 3/1. Similar quenching data were produced by using 675 nm as the excitation wavelength at which only the (+)NP was excited (see Figure 4.3B and reaction 1). Given these observations and the absence of energy transfer (see Figure 4.2), we assign this strong quenching to the hole transfer from the (+)NP to the (-)PDPPPV (see reaction 2). Similar observations and assignments have been reported for other hybrid systems.[5c,14b]

$$\text{(+)NP} + h\nu \leftrightarrow \text{(+)NP(h + e)} \qquad (1)$$

$$\text{(+)NP(h + e)} + \text{(-)PDPPPV} \rightarrow \text{(+)NP(e)} + \text{(-)PDPPPV(h)} \qquad (2)$$

Aggregation quenching is possible in this case because the opposite charges on the (-)PDPPPV and (+)NP drive their electrostatic assembly after mixing them together in solution.[19b] Thus, a control study, by using a (-)PPV polyelectrolyte (poly[5-methoxy-2-(3-sulfopropoxy)-1,4-phenylenevinylene]) of similar molecular weight, was performed to quantify the extent of aggregation quenching. (-)PPV was selected because 1) it has a similar side chain and Zeta-potential as (-)PDPPPV (see Table B2); 2) it forms a type-I heterojunction with the (+)NPs that blocks both electron and hole transfer when only the NP is excited (see Figure B5); and 3) dynamic light scattering experiments show that the (-)PPV induces a similar NP/polymer aggregation size as the (-)PDPPPV for a given concentration (see Figure B6). Figure 4.3C shows that the (-)PPV quenches only ~ 25 % of the (+)NP's PL under the same conditions. This result indicates that aggregation quenching is not strong enough to account for the efficient quenching observed for the (+)NP/(-)PDPPPV assembly.

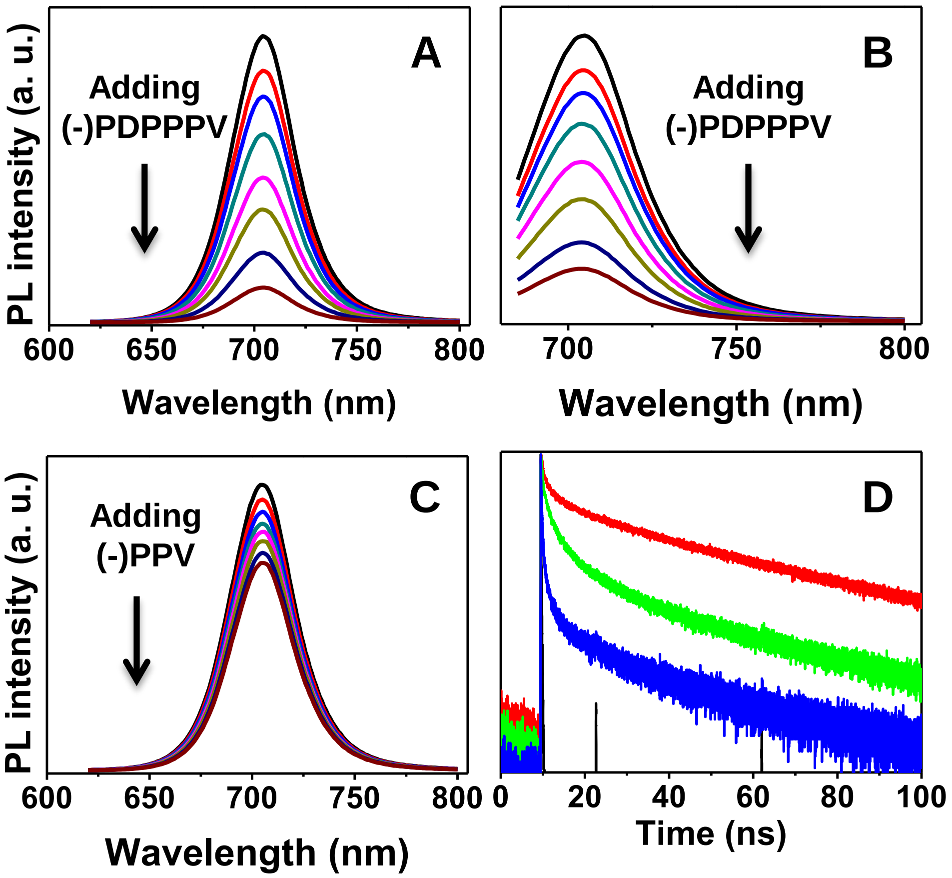

Figure 4-3. Panels A and B presents the steady-state PL quenching results (normalized) for the (+)NP/(-)PDPPPV assembly at an excitation wavelength of 600 nm and 675 nm, respectively. Panels C shows the PL quenching results for the (+)NP/(-)PPV assemblies at an excitation wavelength of 600 nm. The different colors of the spectral curves corresponds to different amounts of the (-)PDPPPV solution being added into the (+)NP solution. As the arrow indicates, the amount added is: 0, 1.2, 2.5, 5, 7.5, 10, 15, and 20 μL. Panel D presents the time-resolved PL decays (normalized) for (+)NP only (red), (+)NP/(-)PPV (green), and (+)NP/(-)PDPPPV (blue) with an excitation and emission wavelength at 660 nm and 710 nm, respectively. The black curve is the instrumental response function. 20 μL of polymer solutions were added into the NP solution in the time-revolved experiments.

Time-resolved photoluminescence spectroscopy was used to corroborate the steady-state measurements and probe the kinetics of the photoinduced charge transfer. By only exciting the NP, Figures 3D shows that (-)PDPPPV quenches the PL lifetime of (+)NP more strongly than the control, (-)PPV. These results are consistent with the data from the steady-state PL quenching. Because of the highly non-exponential slope of the fluorescence decay laws, they were fit to a distribution of lifetimes. Figure B7 plots the lifetime distributions for the PL decays and gives one short and two longer lifetime components. The short component shows the largest changes and systematically shifts to shorten to averaged lifetime when the (-)PDPPPV is added. Based on the previous work,[19b,21] the short component can be tentatively assigned to the hole transfer from (+)NP to (-)PDPPPV, while the longer ones are assigned to the electron-hole recombination. In this approximation, the hole transfer rate constant (k_{CT}) can be estimated as:

$$k_{\mathrm{CT}} = 1/\tau - 1/\tau_0$$

where τ is the short lifetime component for the (+)NP/(-)PDPPPV assembly, and τ_0 is that for the (+)NP/(-)PPV assembly as a reference system. Thus, k_{CT} is estimated to be about $10^{10}\ \mathrm{s}^{-1}$.

4.2.3 Transient absorption spectroscopy and spectroelectrochemistry

Photoinduced hole transfer from (+)NP to (-)PDPPPV can produce a (-)PDPPPV radical cation, (-)PDPPPV$^{\bullet+}$, which can be characterized by ultrafast transient absorption spectroscopy. Figures 4A and 4B show the transient absorption spectra for the (+)NP/(-)PDPPPV assembly, in which the ground-state bleaching for the (-)PDPPPV and (+)NP occurs at 550 nm and 692 nm respectively, while a positive and broad transient absorption centered at 910 nm appears. This broad feature is assigned to be the absorption of (-)PDPPPV radical cation (namely, (-

)PDPPV$^{\bullet+}$) for the following reasons. First, measurements for the (+)NP-only solution show that (+)NP does not have transient absorption in this region, indicating that the feature at 910 nm must arise from the presence of (-)PDPPPV. Figure B8 shows the kinetic traces monitored at 910 nm for the (-)PDPPPV-only and (+)NP/(-)PDPPPV solutions; and it is clear that the lifetime at 910 nm is much longer for (+)NP/(-)PDPPPV than for (-)PDPPPV-only sample. This result suggests that additional pathways in the (+)NP/(-)PDPPPV assembly to generate (-)PDPPPV$^{\bullet+}$, presumably the donor-acceptor charge transfer. Note that several groups have reported transient absorption for other D-A copolymer radical cations in a similar region.[13b,15a,21] Last, this assignment is confirmed by spectroelectrochemistry, see Figure 4.4. Figure 4.4C shows a similar absorption feature arising in the NIR region as an (-)PDPPPV film is electrochemically oxidized to produce (-)PDPPPV$^{\bullet+}$. Figure 4.4D shows that the broad feature at 910 nm cannot be attributed to (-)PDPPPV radical anion ((-)PDPPPV$^{\bullet-}$), because it only absorbs weakly around 400 nm and not in the near-IR. See Appendix B for measurement details.

Note the excitation wavelength used in this measurement is 387 nm, where both (-)PDPPPV and (+)NP are excited. Thus, (-)PDPPPV$^{\bullet+}$ can be generated in two possible ways. One is by hole transfer from the valence band of (+)NP to that of (-)PDPPPV, and the other one is by electron transfer from the conduction band of (-)PDPPPV to that of (+)NP. The limited range of excitation wavelength for our instrument prevented us from separating these two processes by only exciting the (+)NP. However, the PL quenching data suggest that the hole transfer process does not strongly depend on the excitation wavelength (see Figure 4.3). In addition, Ginger et al[14a] has recently reported for a similar hybrid copolymer/NP systems that changing the excitation wavelength from exciting both copolymer and NP to only exciting the NP does not significantly alter the transient concentration of the copolymer radical cations. Thus, it appears that the hole transfer from (+)NP to (-)PDPPPV is the primary process for the formation of (-)PDPPPV$^{\bullet +}$.

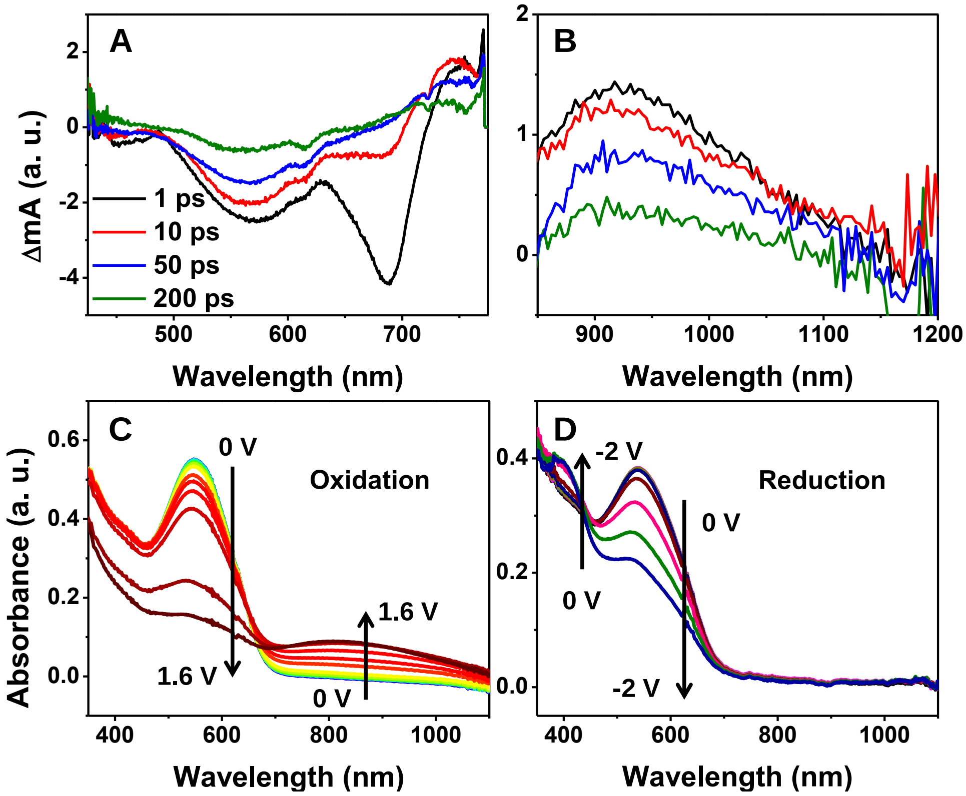

Figure 4-4. Panels A and B show the visible and NIR transient absorption spectra for (+)NP/(-)PDPPPV assemblies recorded at different delay time. Panels C and D show the spectroelectrochemical spectra for the oxidized and reduced (-)PDPPPV drop-cast films measured in a three-electrode spectroelectrochemical cell as the voltage changes with an increment of 0.2 V.

4.2.4 Effect of internal electric field

Figure 4.5 shows the steady-state and time-revolved PL quenching results for the assembly of (-)NP/(+)PDPPPV with reversed surface charge. In sharp contrast to the (+)NP/(-)PDPPPV assemblies, no significant PL quenching was observed for the (-)NP solution with the addition of (+)PDPPPV under the same conditions. The assembly of (-)NP/(+)PDPPPV has a comparable NP/polymer aggregation size as the (+)NP/(-)PDPPPV assembly (see Figure B6). In addition, the PDPPPV copolymers and CdTe NPs used in this work have a similar Zeta-potential magnitude (see Table B2). These data suggest that the difference in PL quenching between the two NP/PDPPPV combinations is not caused by differences in the electrostatic assembly.

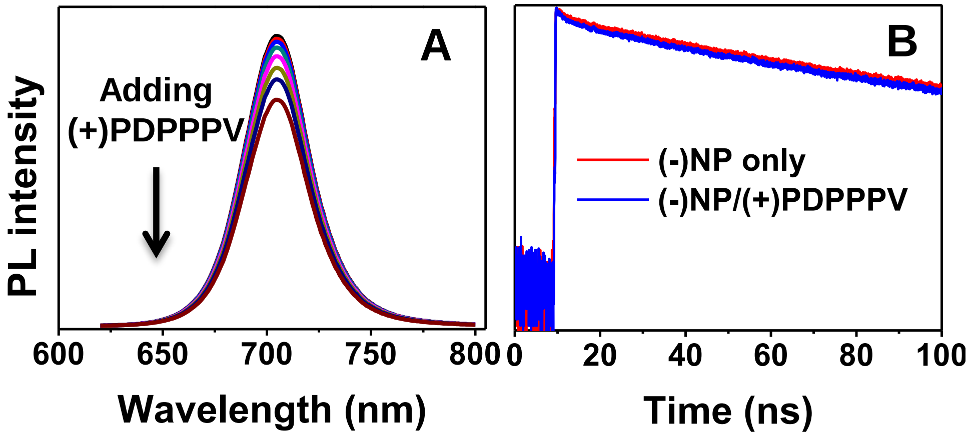

Figure 4-5. Panel A shows the steady-state PL quenching results for the (-)NP/(+)PDPPPV assembly. Panel B presents the time-resolved PL decays for (-)NP only (red) and (-)NP/(+)PDPPPV (blue) solutions. These two measurements were performed under the same condition as those in Figure 4.3.

Rather the difference correlates with the different internal electric field direction between the oppositely charged NP and PDPPPV in the two NP/PDPPPV electrostatic assemblies (see Figure 4.6). For instance, the assembly of (+)NP/(-)PDPPPV should have a favorable internal electric field that drives the hole transfer from (+)NP to (-)PDPPPV in the same direction as the valence band energy offsets. However, reversing the surface charge on both NP and PDPPPV, i.e., (-)NP/(+)PDPPPV, results in no observable hole transfer, because their internal electric field is not oriented with respect to the valence band energy offsets. Hence, generally speaking, a (-)

electron donor and a (+) electron acceptor can generate an internal electric field that favors charge separation. This observation agrees well with the findings that were reported previously for a NP/NP D-A system.[19b] In that case, the charge transfer was found to be very efficient when a (-) NP electron donor and (+) NP electron acceptor was used, but not with reversed surface charges on both NPs. The current work extends this approach to NP/polymer hybrid systems, and suggests its use for enhancing the charge separation efficiency for hybrid solar cells.

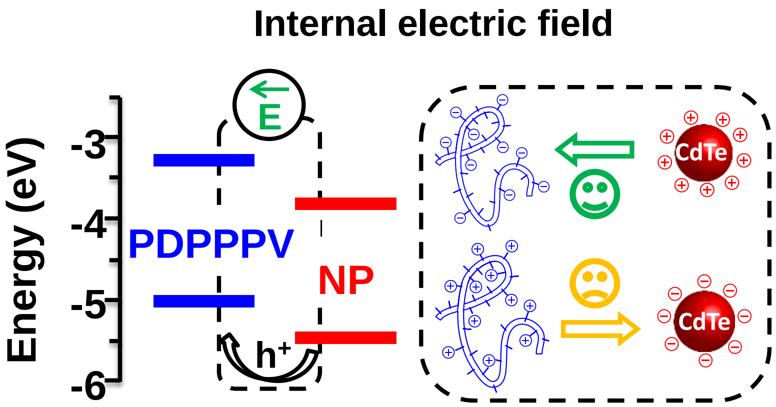

Figure 4-6. A schematic presentation for the internal electric field in the two NP/PDPPPV assemblies and its effect on the photoinduced hole transfer from the NP valence band to the PDPPPV valence band.

It is well established for conventional p-n junction solar cells that the internal electric field built-in a depletion region can efficiently separate excitons and inhibit charge recombination.[22] This feature has been employed for NP-based solar cells. As Sargent et al recently reported for a PbS-NP/TiO_2 depleted heterojunction device,[23] an internal charge-separating electric field at the PbS/TiO_2 interface can help to dissociate excitons in conjunction with the D-A energy offsets. Their devices achieved a power conversion efficiency of 7%, which is the highest for NP-based photovoltaics reported to date.[24] Thus, it may be interesting and beneficial to combine both D-A energy offsets and an internal electric field as a dual charge-separation driving force for the hybrid solar cells, with an ultimate goal of enhancing their power conversion efficiency.

4.3 CONCLUSION

In summary, this work has demonstrated a charge transfer study for a hybrid conjugated-copolymer/semiconductor-nanoparticle model system, by using a variety of spectroscopic and electrochemical characterization techniques. The most remarkable finding in this study is that, by controlling the direction of the internal electric field, one can manipulate the hole transfer rate in the copolymer/NP electrostatic assemblies. The presence of the internal field may help reduce the energy loss resulting from charge recombination and potentially increase the open circuit voltage of hybrid solar cells. Thus, this work suggests a strategy for developing better donor-acceptor materials for hybrid bulk heterojunction solar cells by employing a dual charge-separation driving force at the D-A heterojunction which can promote charge separation and inhibit charge recombination.

4.4 REFERENCES

(1) a) He, M.; Qiu, F.; Lin, Z. *The Journal of Physical Chemistry Letters* **2013**, 1788; b) Reiss, P.; Couderc, E.; De Girolamo, J.; Pron, A. *Nanoscale* **2011**, *3*, 446; c) Martinez-Ferrero, E.; Albero, J.; Palomares, E. *Journal of Physical Chemistry Letters* **2010**, *1*, 3039; d) Milliron, D. J.; Gur, I.; Alivisatos, A. P. *Mrs Bulletin* **2005**, *30*, 41; e) Greenham, N. C.; Peng, X.; Alivisatos, A. P. *Physical Review B* **1996**, *54*, 17628; f) McGehee, M. D. *MRS Bulletin* **2009**, *34*, 95.

(2) a) Thompson, B. C.; Fréchet, J. M. J. *Angewandte Chemie International Edition* **2008**, *47*, 58; b) Talapin, D. V.; Lee, J. S.; Kovalenko, M. V.; Shevchenko, E. V. *Chemical Reviews* **2010**, *110*, 389.

(3) Huynh, W. U.; Dittmer, J. J.; Alivisatos, A. P. *Science* **2002**, *295*, 2425.

(4) a) Ren, S.; Chang, L.-Y.; Lim, S.-K.; Zhao, J.; Smith, M.; Zhao, N.; Bulović, V.; Bawendi, M.; Gradečak, S. *Nano Letters* **2011**, *11*, 3998; b) Dayal, S.; Reese, M. O.; Ferguson, A. J.; Ginley, D. S.; Rumbles, G.; Kopidakis, N. *Advanced Functional Materials* **2010**, *20*, 2629.

(5) a) Mejia, M. L.; Agapiou, K.; Yang, X. P.; Holliday, B. J. *Journal of the American Chemical Society* **2009**, *131*, 18196; b) Xu, J.; Wang, J.; Mitchell, M.; Mukherjee, P.; Jeffries-El, M.; Petrich, J. W.; Lin, Z. Q. *Journal of the American Chemical Society* **2007**, *129*, 12828; c) Cai, X. C.; De, P. K.; Anyaogu, K. C.; Adhikari, R. M.; Palayangoda, S. S.; Neckers, D. C. *Chemical Communications* **2009**, 1694; d) Sudeep, P. K.; Early, K. T.; McCarthy, K. D.; Odoi, M. Y.; Barnes, M. D.; Emrick, T. *Journal of the American Chemical Society* **2008**, *130*, 2384; e) Milliron, D. J.; Alivisatos, A. P.; Pitois, C.; Edder, C.; Frechet, J. M. J. *Advanced Materials* **2003**, *15*, 58.

(6) Xiang, H. J.; Wei, S. H.; Gong, X. G. *Journal of Physical Chemistry C* **2009**, *113*, 18968.

(7) a) Ehrler, B.; Wilson, M. W. B.; Rao, A.; Friend, R. H.; Greenham, N. C. *Nano Letters* **2012**, *12*, 1053; b) Ehrler, B.; Walker, B. J.; Bohm, M. L.; Wilson, M. W. B.; Vaynzof, Y.; Friend, R. H.; Greenham, N. C. *Nature Communications* **2012**, *3*.

(8) Shaw, P. E.; Ruseckas, A.; Samuel, I. D. W. *Advanced Materials* **2008**, *20*, 3516.

(9) Graetzel, M.; Janssen, R. A. J.; Mitzi, D. B.; Sargent, E. H. *Nature* **2012**, *488*, 304.

(10) Saunders, B. R. *Journal of Colloid and Interface Science* **2012**, *369*, 1.

(11) a) Zhou, R.; Xue, J. *ChemPhysChem* **2012**, *13*, 2471; b) Noone, K. M.; Subramaniyan, S.; Zhang, Q.; Cao, G.; Jenekhe, S. A.; Ginger, D. S. *The Journal of Physical Chemistry C* **2011**, *115*, 24403.

(12) ten Cate, S.; Schins, J. M.; Siebbeles, L. D. A. *Acs Nano* **2012**, *6*, 8983.

(13) a) Dayal, S.; Kopidakis, N.; Olson, D. C.; Ginley, D. S.; Rumbles, G. *Nano Letters* **2009**, *10*, 239; b) Wang, P.; Abrusci, A.; Wong, H. M. P.; Svensson, M.; Andersson, M. R.; Greenham, N. C. *Nano Letters* **2006**, *6*, 1789.

(14) a) Strein, E.; Colbert, A.; Subramaniyan, S.; Nagaoka, H.; Schlenker, C. W.; Janke, E.; Jenekhe, S. A.; Ginger, D. S. *Energy & Environmental Science* **2013**, *6*, 769; b) Xu, Z.; Hine, C. R.; Maye, M. M.; Meng, Q.; Cotlet, M. *ACS Nano* **2012**, *6*, 4984; c) Bansal, N.; Reynolds, L. X.; MacLachlan, A.; Lutz, T.; Ashraf, R. S.; Zhang, W.; Nielsen, C. B.; McCulloch, I.; Rebois, D. G.; Kirchartz, T.; Hill, M. S.; Molloy, K. C.; Nelson, J.; Haque, S. A. *Sci. Rep.* **2013**, *3*.

(15) a) Liang, Y.; Yu, L. *Accounts of Chemical Research* **2010**, *43*, 1227; b) Li, G.; Zhu, R.; Yang, Y. *Nat Photon* **2012**, *6*, 153; c) Yuen, J. D.; Wudl, F. *Energy & Environmental Science* **2013**, *6*, 392.

(16) a) Wu, M.; Kaur, P.; Yue, H.; Clemmens, A.; Waldeck, D.; Xue, C.; Liu, H. *The journal of physical chemistry. B* **2008**, *112*, 3300; b) Kaur, P.; Yue, H.; Wu, M.; Liu, M.; Treece, J.; Waldeck, D.; Xue, C.; Liu, H. *The journal of physical chemistry. B* **2007**, *111*, 8589; c) Kaur, P.; Wu, M.; Anzaldi, L.; Waldeck, D. H.; Xue, C.; Liu, H. *Langmuir* **2007**, *23*, 13203.

(17) Hwang, I.; Beaupre, S.; Leclerc, M.; Scholes, G. D. *Chemical Science* **2012**, *3*, 2270.

(18) Wang, Y.; Xie, Z.; Gotesman, G.; Wang, L.; Bloom, B. P.; Markus, T. Z.; Oron, D.; Naaman, R.; Waldeck, D. H. *The Journal of Physical Chemistry C* **2012**, *116*, 17464.

(19) a) Yu, W. W.; Wang, Y. A.; Peng, X. *Chemistry of Materials* **2003**, *15*, 4300; b) Wu, M.; Mukherjee, P.; Lamont, D. N.; Waldeck, D. H. *The Journal of Physical Chemistry C* **2010**, *114*, 5751.

(20) Gregg, B. A. *The Journal of Physical Chemistry B* **2003**, *107*, 4688.

(21) a) Rolczynski, B. S.; Szarko, J. M.; Son, H. J.; Liang, Y.; Yu, L.; Chen, L. X. *Journal of the American Chemical Society* **2012**, *134*, 4142; b) Guo, J.; Liang, Y.; Szarko, J.; Lee, B.; Son, H. J.; Rolczynski, B. S.; Yu, L.; Chen, L. X. *The Journal of Physical Chemistry B* **2009**, *114*, 742; c) Ohkita, H.; Cook, S.; Astuti, Y.; Duffy, W.; Tierney, S.; Zhang, W.; Heeney, M.; McCulloch, I.; Nelson, J.; Bradley, D. D. C.; Durrant, J. R. *Journal of the American Chemical Society* **2008**, *130*, 3030.

(22) Kittel, C. *Introduction to Solid State Physics*; 8th ed.; Wiley, 2004.

(23) Pattantyus-Abraham, A. G.; Kramer, I. J.; Barkhouse, A. R.; Wang, X.; Konstantatos, G.; Debnath, R.; Levina, L.; Raabe, I.; Nazeeruddin, M. K.; Grätzel, M.; Sargent, E. H. *ACS Nano* **2010**, *4*, 3374.

(24) Ip, A. H.; Thon, S. M.; Hoogland, S.; Voznyy, O.; Zhitomirsky, D.; Debnath, R.; Levina, L.; Rollny, L. R.; Carey, G. H.; Fischer, A.; Kemp, K. W.; Kramer, I. J.; Ning, Z.; Labelle, A. J.; Chou, K. W.; Amassian, A.; Sargent, E. H. *Nat Nano* **2012**, *7*, 577.

(25) Egbe, D. A. M.; Tillmann, H.; Birckner, E.; Klemm, E. *Macromolecular Chemistry and Physics* **2001**, *202*, 2712.

(26) Liu, K.; Li, Y.; Yang, M. J. *Journal of Applied Polymer Science* **2009**, *111*, 1976.

(27) Xiao, S. X.; Wang, S.; Fang, H. J.; L., L. Y.; Q., S. Z.; Du, C. M.; Zhu, D. B. *Macromolecular Rapid Communications* **2001**, *22*, 1313.

(28) Lu, S. L.; Yang, M. J.; Luo, J.; Cao, Y.; Bai, F. L. *Macromolecular Chemistry and Physics* **2005**, *206*, 664.

(29) Xie, B. H.; Bagui, M.; Guo, R. R.; Li, K.; Wang, Q.; Peng, Z. H. *Journal of Polymer Science Part A: Polymer Chemistry* **2007**, *45*, 5123.

(30) Rabindranath, A. R.; Zhu, Y.; Heim, I.; Tieke, B. *Macromolecules* **2006**, *39*, 8250.

(31) Liu, K.; Li, Y.; Zhang, G. Q.; Lv, X.; Yang, M. J. *Sensors And Actuators B-chemical* **2009**, *135*, 597.

(32) Fan, Q. L.; Lu, S.; Lai, Y. H.; Hou, X. Y.; Huang, W. *Macromolecules* **2003**, *36*, 6976.

(33) a) Bronstein, H.; Chen, Z.; Ashraf, R. S.; Zhang, W.; Du, J.; Durrant, J. R.; Shakya Tuladhar, P.; Song, K.; Watkins, S. E.; Geerts, Y.; Wienk, M. M.; Janssen, R. A. J.; Anthopoulos, T.; Sirringhaus, H.; Heeney, M.; McCulloch, I. *Journal of the American Chemical Society* **2011**, *133*, 3272; b) Bijleveld, J. C.; Gevaerts, V. S.; Di Nuzzo, D.; Turbiez, M.; Mathijssen, S. G. J.; de Leeuw, D. M.; Wienk, M. M.; Janssen, R. A. J. *Advanced Materials* **2010**, *22*, E242; c) Biniek, L.; Schroeder, B. C.; Nielsen, C. B.; McCulloch, I. *Journal of Materials Chemistry* **2012**, *22*, 14803.

(34) Haram, S. K.; Quinn, B. M.; Bard, A. J. *Journal of the American Chemical Society* **2001**, *123*, 8860.

(35) a) Liu, Q.; Lü, X.; Geng, L.; Lü, C. *Polymer International* **2011**, *60*, 1514; b) Zhang, G.; Xu, H.; Liu, K.; Li, Y.; Yang, L.; Yang, M. *Synthetic Metals* **2010**, *160*, 1945; c) Haram, S. K.; Kshirsagar, A.; Gujarathi, Y. D.; Ingole, P. P.; Nene, O. A.; Markad, G. B.; Nanavati, S. P. *Journal of Physical Chemistry C* **2011**, *115*, 6243.

(36) a) Tvrdy, K.; Frantsuzov, P. A.; Kamat, P. V. *Proceedings of the National Academy of Sciences* **2011**, *108*, 29; b) Bang, J. H.; Kamat, P. V. *Acs Nano* **2011**, *5*, 9421.

5.0 FORMATION OF DEPLETED BULK HETEROJUNCTIONS IN THERMALLY ANNEALED PBS QUANTUM DOT SOLAR CELLS

This work has been submitted to **Advanced Functional Materials** as Bo Ding, Yang Wang, Po-Shun Huang, David Waldeck, and Jung-Kun Lee. The thesis author participated in PbS NP synthesis, design and fabrication of photovoltaic devices, and electrochemical measurements. The supporting information for this chapter is provided in Appendix C.

We have studied the effect of thermal annealing on the junction structure and energy conversion behavior of TiO_2/PbS heterojunction solar cells. PbS quantum dots (QDs) with a band gap of 1.67 eV were chosen to examine how thermal annealing in an inert atmosphere can influence the morphologies and optical properties of the PbS QDs film. Nanoscale structure and composition analysis have revealed that thermal annealing causes intermixing of the TiO_2 and PbS phases. This intermixing increased the junction area within the depleted bulk heterojunction (DBH) layer and promoted the carrier extraction from PbS QD to TiO_2. In addition, the thermal annealing caused inter-particle necking between PbS QDs and increased the crystallinity of the PbS QD film. Compared with un-annealed PbS/TiO_2 heterojunction solar cells, the formation of the DBH layer and the partial sintering of PbS QDs led to a doubling of the short-circuit current (J_{sc}) and an improved energy conversion efficiency, by 39%. Electric force microscopy analysis confirmed the presence of a DBH layer. The electron lifetime and fill factor (FF) of the solar cells decreased when the TiO_2/PbS mixed film was thermally annealed, and this was assigned to a lower recombination resistance in the DBH layer. Post-treatment of PbS/TiO_2 DBH films with ethanedithiol was found to increase the recombination resistance at PbS/TiO_2 interface and to enhance the energy conversion efficiency to ~4%.

5.1 Introduction

Quantum Dots (QDs) have attracted a great deal of research interest over the past few decades because of their unique optical and electronic properties.[1] Their large optical cross section, tunable band gap, and slow phonon relaxation are valuable physical properties that are driving their use in solar energy conversion devices, i.e., solar cells. In addition, QDs can be made through inexpensive solution-based synthesis, and they are proving amenable to facile and large-scale device fabrication methods. Hence, QDs have been used recently for different types of photovoltaic devices.[2] However, better device structures are needed for QD-based photovoltaics to compete with the conventional technologies which are already commercialized.

QDs of lead chalcogenide, such as PbS and PbSe, have large Bohr exciton radius, low exciton binding energy, and are considered excellent absorbers of visible and near IR light.[3, 4] Because of this promise, several groups have performed research to pave the way toward the creation of hybrid solar cells using *p*-type lead chalcogenide QDs as the photoactive component of solar cells.[5] Moreover, QD solar cells have the potential of generating multiple excitons from a single hot carrier[6, 7] Recently, the concept of multiple exciton generation (MEG) has been reported in a thin-film type solar cell.[8-11] The configuration of a so-called thin-film type colloidal quantum dot (CQD) solar cell, as proposed by Sargent[12-14] and Nozik,[15, 16] contains a Schottky barrier between the QD semiconductor film and a metal electrode, where the photogenerated carriers are collected. From the standpoint of processing, this QD layer has the strength of easy deposition using a spin coating process[14, 17] or a layer-by-layer dip coating process.[18] One main drawback of the QD/metal structure is a low open circuit voltage (V_{oc}), which is determined by the separation of the quasi-Fermi levels at the contacts to the photoactive layer.[19] To solve the problem of low V_{oc}, a layer of an *n*-type wide bandgap semiconductor such as TiO_2[19, 20] or ZnO has been inserted between the QD layer and transparent conducting layer to form a depleted heterojunction structure.[21] This heterojunction changes the electron transport direction and increases the quasi-Fermi level difference, leading to a higher V_{oc}.[19]

To date, many groups have worked on improving the energy conversion efficiency of CQD solar cells. To this end, the effect of the QD size on the injection and potential energy of electrons has been investigated. One such group explored the dependence of the solar cell efficiency as a function of QD size and found an optimum efficiency of the CQDs solar cell by employing medium size PbS QDs with a band gap of 1.53 eV. This optimal size is believed to reflect a compromise between smaller QDs, which lead to decreased light absorption and to a higher Schottky barrier, and larger QDs, which lead to poorer carrier extraction and concomitantly higher carrier recombination.[22] In addition, the rate of charge transport between QDs is influenced by the length of surface ligands. Compared with long oleic chains, shorter thiol ligands, such as 1,2-ethanedithiol (EDT),[18] mercaptocarboxylic acids (MPA),[20] and benzenedithiol (BDT),[23] have been reported to shorten the distance between adjacent QDs and facilitate carrier transport between QDs.

Thermal annealing has been considered an effective way to enhance the conductivity and carrier mobility of thiol-capped CQD films. Thermal treatment of QDs reduces the inter-CQD separation and/or facilitates particle aggregation along preferential crystallographic axes.[24-26] Zhao *et al.*[27] reported that mild thermal annealing of the PbS QD film in air greatly enhances the fill factor (FF) and V_{oc} of PbS/organic bilayer solar cells. Formation of an inert interfacial layer such as $PbSO_3$ or PbO after annealing was shown to limit current leakage and suppress charge recombination. Very recently, Gao *et al.*[28] found that the electronic coupling between the QDs and carrier transport in ZnO/PbS(QDs)/MoO_x/Al solar cells are improved during thermal annealing in an inert atmosphere.

Here, we report on the formation of a depleted bulk heterojunction (DBH) for a PbS-TiO_2 thin film in Fluorine-doped SnO_2 (FTO)/TiO_2/PbS-QD/Au solar cells, and a consequent increase in cell performance by thermal annealing. Small PbS QDs with a band gap of 1.67 eV were chosen to show how annealing can influence the morphologies and optical properties of the QDs and PbS QD film. Large PbS QDs with a band gap of 1.32 eV were employed as a control to explore the effect of QD size on cell performance during annealing. We observed that the average inter-particle distance decreases and necking between adjacent QDs occurs after thermal treatment. This partial connection between QDs enhances the carrier transport by increasing the probability of carrier hopping and decreasing the chance of carrier trapping. More importantly, we found that the QDs diffuse into the TiO_2 mesoporous film to form a DBH structure. This increases the TiO_2/PbS interface area, resulting in more efficient carrier transfer from PbS QDs to TiO_2 nanoparticles. Thus, we find that the short circuit current density (J_{sc}) of thermally annealed heterojunction solar cells can be dramatically enhanced with a minimal change in V_{oc}.

5.2 Experimental section

5.2.1 Materials

Titanium(IV) isopropoxide (TTIP, 97%), lead oxide (PbO), oleic acid (OA), octadecene (ODE), hexamethyldisilathiane (TMS), 1,2-ethanedithiol (EDT), hexane, and acetonitrile (all solvents are anhydrous) were all purchased form Aldrich and used as received. Ethanol (200 proof, anhydrous) was bought from Decon Laboratories Inc. and nitric acid (HNO_3, 70%) from J. T. Baker. Ultrapure water (18.2 MΩ resistivity) was deionized from MIlli-Q purification system (Millipore, MA).

5.2.2 Synthesis of PbS Colloidal Quantum Dots

PbS QDs with an excitonic peak at 740 nm were synthesized following a procedure developed by Hines and Scholes.[4] All the reactions were carried out using standard air-freetechniques. The lead oleate precursor was prepared by mixing 0.09 g PbO, 0.25 ml OA and 3.75 ml ODE in a three-necked flask, and it was vigorously stirred under Ar at 150 ^{o}C for 30 min. Once all the lead oxide had dissolved, heating was stopped to let the lead oleate solution cool down to 120 ^{o}C. Then 42 μL TMS in 2 ml ODE was swiftly injected into the precursor solution with a sudden drop of the reaction temperature to 100 ^{o}C. The heating mantle was then immediately restored and the reaction temperature was kept at 100 ^{o}C. The solution's color changed from transparent to brown gradually. After 30 sec, the heating mantle was removed to let the solution cool down to room temperature. The PbS QDs were washed by repeated precipitation with acetone and dispersion with toluene, and they were finally dispersed in anhydrous hexane. PbS QDs with an excitonic peak at 940 nm were synthesized in a similar manner, except at a higher reaction temperature (140 ^{o}C) and for a longer growth time (5 min).

5.2.3 Device Fabrication

The patterned fluorine-doped tin oxide (FTO) (Pilington TEC 8) coated glass substrates were submerged in an ethanol/acetone (1:1) mixture and cleaned by sonication for 10 min. In order to form a thin crystallized TiO_2 hole blocking layer on the FTO glass, 150 ml of pure ethanol and 23.04 ml of TTIP were well mixed. To this solution, another mixture containing 150 ml of pure ethanol, 2.77 ml of DI water, and 0.36 ml of HNO_3 (70% concentration) was slowly poured in. This TiO_2 sol was spin coated on the precleaned FTO glass and annealed in O_2 at 500 ^{o}C for 2 h. Another TiO_2 layer was printed by tape-casting of TiO_2 paste containing 20 nm sized TiO_2 nanoparticles.[47] Subsequently, the TiO_2 layer was annealed in air at 450 ^{o}C for 30 min to form a mesoporous film with a thickness of ~ 1 µm. On top of the TiO_2 mesoporous film, a 200 nm thick QD film was prepared using a fourteen cycle layer-by-layer dip coating method in an Ar gas filled glove box. During each cycle, typically, the substrate (TiO_2/FTO or silicon) was dipped into a PbS QDs/hexane solution (20 mg/ml) by hand. After submerging for 5 sec, the substrate was slowly dragged out of the solution at a velocity of ~0.2 cm s^{-1}. Then the substrate was dipped into 0.1 M EDT/acetonitrile for 10 sec and quickly removed. Complete drying of the QD film before each dipping cycle was necessary to keep the film smooth. Finally, a 20 nm thick gold layer was deposited onto the PbS film by electron beam evaporation to form the top electrode. Each device had an active area of 0.04 cm^2.

5.2.4 PbS QDs and PbS film Characterization

The morphologies of the PbS QDs and cross-sectional view of the Au/PbS/TiO_2 films were tested by high-resolution transmission electron microscopy (HRTEM) JEOL JEM-2100F. The Z-contrast high angle annular dark field (HADDF) cross-section images of the films were tested in STEM mode, and the elemental distribution was studied with EDS mapping. The PbS QD samples were prepared on a Cu grid, with a post ligand exchange in 0.1 M EDT/acetonitrile solution for 10 sec. The film samples were deposited on a silicon substrate and prepared by mechanical polishing and ion milling.

The optical properties of the PbS QDs and PbS film were investigated with a UV-vis spectrophotometer (Lambda 35, Perkin Elmer) attached to an integrating sphere over a wavelength range from 300 nm to 1100 nm. X-ray photoelectron spectra (XPS) were collected with monochromatic Al-Kα X-rays (1487 eV) at 150W power on a custom built multi-technique surface analysis instrument. In order to increase the accuracy and sensitivity of the analysis, surface contamination or oxidation of the PbS films were cleaned off by ion beam etching before signal collection. Data analysis was carried out using an open source code, XPSPEAK41, for background subtraction and peak fitting. The morphology and current image of the PbS film, both with and without annealing, were examined by conductive-atomic force microscopy (c-AFM, Multiview-1000, Nanonics). The electric current under bias was measured at the nanoscale using a boron-doped diamond probe.

5.2.5 Device characterization

Photovoltaic properties were measured under AM 1.5 G simulated sunlight (PV Measurements, Inc) with the aid of an electrochemical workstation (CH Instruments, CHI 660C). An electrochemical impedance spectroscopy (EIS) measurement was also performed in the frequency range of 0.1 Hz to 1 kHz with the maximum electric potential of 0.05 V. During EIS measurement, the solar cells were in the open circuit condition and exposed to simulated solar light. Incident photon to current efficiency curves (IPCE) of the solar cell were also measured by illuminating the sample with a monochromatic beam (Newport Corp.). IPCE was calculated by IPCE (λ) = 1240 ($J_{SC}/\lambda\varphi$) where λ is the wavelength of the incident beam, J_{sc} is the short-circuit current density, and φ is the incident radiative flux, which was measured by using a silicon reference photodiode. The electron lifetime was measured using an open-circuit voltage decay (OCVD) technique.[45] The light source was a laser diode (λ= 660 nm) driven by a function generator (Agilent 33220A) to provide square wave modulated illumination. The changes in the photovoltage were monitored by a digital oscilloscope (Tektronix, TDS2024B).

5.3 Results and discussions

5.3.1 Optical Properties and Morphology Evolution of PbS QDs

PbS QDs capped with an oleic acid ligand were synthesized by using a procedure developed by Hines and Scholes[4]. Figure 5.1a shows the absorbance spectra of the PbS QDs dispersed in hexane. The first excitonic absorption peak was located at 740 nm (1.67 eV) for the smaller PbS

QDs and 940 nm (1.32 eV) for the larger ones. The energy band structures of the TiO_2 nanoparticles[20] and PbS QDs are shown in Figure 5.1b. A position for the valence band edge of the QD was determined by cyclic voltammetry (see Figure C1).

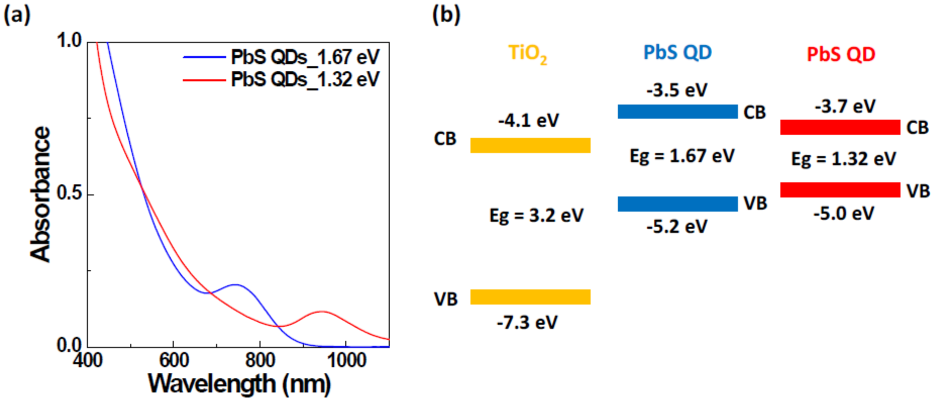

Figure 5-1. (a) Absorbance spectra are shown for PbS QDs with two different sizes in hexane. (b) The relative band gap locations are shown for the TiO_2 NPs and the PbS QDs with different sizes.

Figure 5.2 shows transmission electron microscopy (TEM) and high-resolution transmission electron microscopy (HRTEM) images of the smaller PbS QDs (E_g = 1.67 eV) that were treated at different annealing temperatures. In addition, the morphology of the larger PbS QDs (E_g = 1.32 eV) before annealing is shown in Figure C2. To address the morphology evolution of the smaller PbS QDs after annealing, the Cu grid for TEM analysis was first coated with a monolayer of PbS QDs and the ligand on the surface of the QDs was replaced by EDT in an inert atmosphere. Then the Cu grids were thermally annealed for 10 min. While the heating of QDs capped with oleic acids showed a diffusion or reaction-controlled isotropic Ostwald ripening in solution,[29] the dry annealing of QDs caused anisotropic coalescence of QDs, in particular along the <100> crystallographic axes.[25] This coalescence occurs because an extreme decrease in the QD melting temperature enables neighboring QDs to be sintered below 200 °C.[30] The average diameter of the QDs was 3.0 ± 0.3 nm, 3.6 ± 0.3 nm, and 3.8 ± 0.3 nm at room temperature, 100 °C, and 150 °C, respectively. The HRTEM (Figure 5.2 e-h) images of the 100 °C and 150 °C annealed QD layers show conspicuous crystal lattice planes continuously traversing interconnected QDs. This indicates that QDs with a band gap of 1.67 eV have high crystallinity, which is an essential condition for low defect concentration and high carrier transport in PbS films.

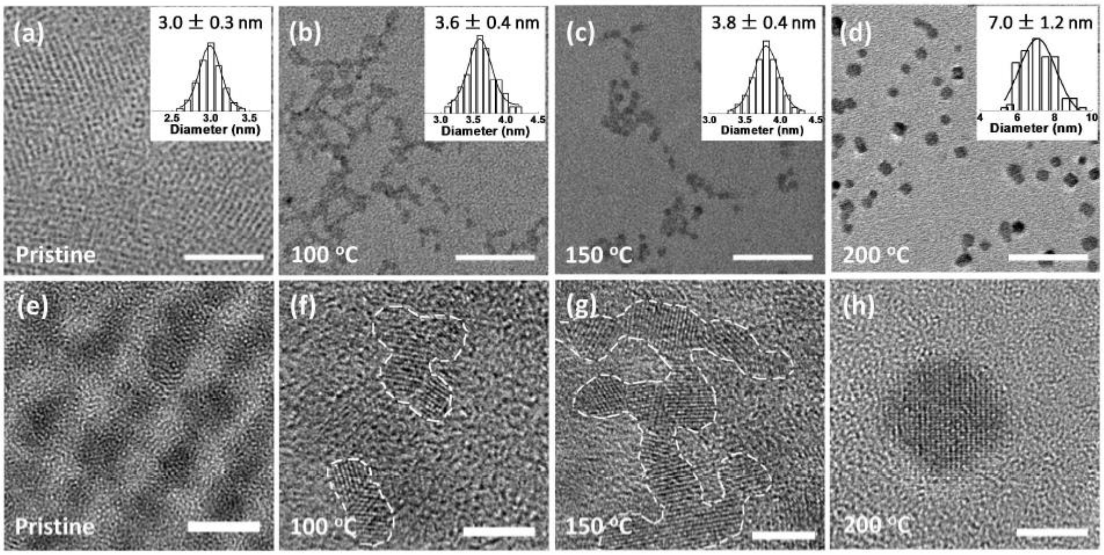

Figure 5-2. Large scale TEM and HRTEM images are shown for the PbS QDs on a Cu grid before (a, e) and after thermal annealing at 100 °C (b, f), 150 °C (c, g) and 200 °C (d, h). The scale bar in the large scale TEM images on the upper row are 50 nm and in the HRTEM images on the bottom row are 5 nm.

5.3.2 Effect of Thermal Annealing on Band Gap and Linker Molecules of PbS NP films

The PbS film of the CQDs solar cells was prepared using a layer-by-layer dip coating method. After each dipping cycle, the freshly deposited QD film was submerged in an EDT solution to replace the capping ligand. The dip coating method was chosen as a more precise way to control the thickness and surface roughness of the QD film than the spin coating method.[18, 22] In this study, dipping and ligand exchange were repeated fourteen times to reach a thickness of 200 nm. The PbS film was then annealed for 10 min in an inert atmosphere at 100 °C – 200 °C. The optical band gap of the PbS film (QD E_g = 1.67 eV) was derived from the UV-Vis diffuse reflectance spectra using the Kubelka-Munk equation, $F(R) = (1-R)^2/2R$, where R is the reflectance.[31] Figure 5.3 shows that the optical band gap of the PbS film decreased from 1.65 eV to 1.32 eV as the annealing temperature increased to 150 °C. This change in the optical band gap of the PbS film results from inter-particle necking and QD size growth. A decreased band gap is expected to cause a red shift of the absorption onset and result in more low-energy photons being collection. In addition, a decrease in the Fermi level difference between PbS and TiO_2 by thermal annealing reduces the open circuit voltage in the device.[19]

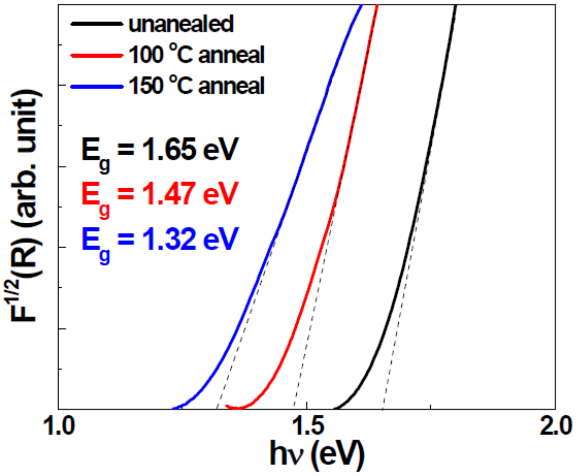

Figure 5-3. Plots of transformed Kubelka-Munk function versus the energy of the light absorbed are shown for the PbS film derived from the UV-Vis diffuse reflectance spectra.

A change in the chemical composition of the PbS film (QD E_g = 1.67 eV) during thermal annealing was investigated using X-ray photoelectron spectroscopy (XPS). Once loaded in the XPS chamber, the surface of the PbS film was cleaned by ion beam etching. Figure 5.4 shows the XPS spectra of the EDT-coated PbS films annealed in an inert atmosphere. Although the compositional change is more apparent in air,[27, 32] the XPS signal from the C-S bonds of the EDT decreases with an increase in annealing temperature under an inert atmosphere. The chemical species and corresponding atomic percentages from the S 2p doublets peak fitting were derived from the literature;[27] see Table 5.1. When the PbS film was annealed at 100 °C and 150 °C, the concentration of carbon and sulfur decreased slightly, presumably because of necking and growth of QDs and partial thermal detachment of EDT. As the annealing temperature increased to 200 °C, the peak area contributed by C-S bonds decreased by about 70%, which indicates that most of the EDT capping agent decomposed or detached from the QDs. Without the passivation of the capping ligand, the QD size can increase dramatically, as shown in Figure 5.2.

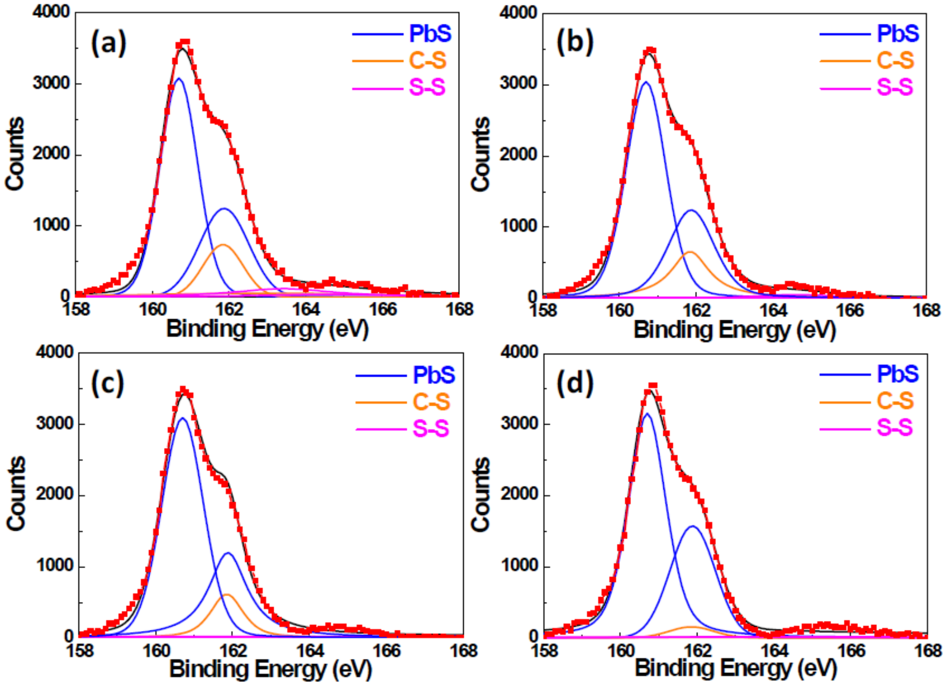

Figure 5-4. XPS spectra are shown for the S 2p peaks in (a) unannealed PbS film and films annealed at (b) 100 °C, (c) 150 °C and (d) 200 °C. The S 2p doublet with an intensity ratio of 2:1 and a splitting of 1.18 eV was applied for sulfur species fitting. The binding energies were 160.7 eV and 161.88 eV for PbS, 161.85 eV and 163.03 eV for C-S, 163.43 eV and 164.61 eV for S-S.

Table 5.1. Chemical species and corresponding atomic percentages of S 2p doublets used for peak fitting in the XPS spectra.

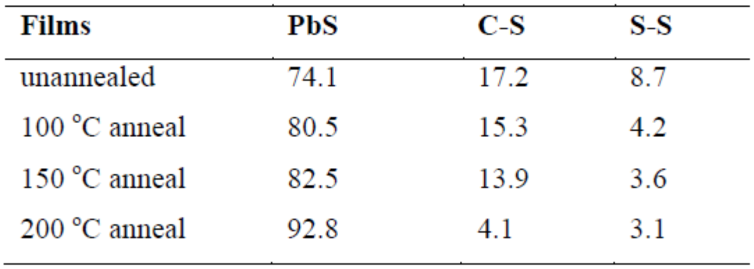

Films	PbS	C-S	S-S
unannealed	74.1	17.2	8.7
100 °C anneal	80.5	15.3	4.2
150 °C anneal	82.5	13.9	3.6
200 °C anneal	92.8	4.1	3.1

5.3.3 Performance of Solar Cells

A heterojunction structure solar cell of FTO/TiO_2/PbS/Au multilayer films was prepared. Initially, a 1 µm thick *n*-type TiO_2 hole blocking layer was spin-coated directly onto FTO film coated glass substrates. A *p*-type PbS film was prepared using the LBL dipping method; see Experimental Section. The thickness of the PbS film was controlled to be ~200 nm, which is reported to be optimal for the PbS thin film solar cell.[33] The efficiency of this device architecture is reported to be controlled by the width of the depletion region, minority diffusion length, and the light absorption.[33] A cross-section of the PbS film is shown in Figure C3. After the PbS film was annealed at various temperatures in an Ar-filled glove box, a 20 nm Au anode layer of high work function was deposited on top of the PbS film using electron beam evaporation.

The performance of devices using unannealed and annealed PbS films was tested under AM 1.5 conditions, and mostly for PbS films comprised of the smaller PbS QDs with an initial E_g of 1.67 eV. The J-V curve (Figure 5.5a) of the devices using the smaller PbS QDs reveals that an increase in the annealing temperature increased the short-circuit current, J_{sc}. Details of the device parameters are summarized in Table 5.2. The J_{sc} from the unannealed PbS QDs was 10.41

mA/cm^2, and it increased to 15.63 mA/cm^2 after 100 ^{o}C annealing, and further reached 21.72 mA/cm^2 after 150 ^{o}C annealing. We hypothesize that this two-fold enhancement in J_{sc} arises, in part, from the faster and more direct carrier transport path that is associated with the necking structure between adjacent QDs. In addition, the slightly enlarged particle size and necking structure enhances the photon collection ability in the visible range, because of the shrinkage in the band gap. On the other hand, the open-circuit voltage V_{oc} showed a slight decrease as the annealing temperature increased, probably because the hole quasi Fermi level shifts upward and the difference in the quasi-Fermi levels of the PbS film is reduced after the thermal annealing.[28] This shift of quasi-Fermi level is mainly responsible for the 23% decrease in V_{oc}. In addition, partial detachment of EDT ligand could introduce surface traps as new recombination sites for charge carriers on the QDs, leading to a lower fill factor (FF) and V_{oc}. The series resistance (R_S) and shunt resistance (R_{SH}) were calculated from $\partial V/\partial J$ at the open circuit and short circuit condition, respectively.[27] The equivalent circuit of the device is shown in Figure C4, from which the R_S and R_{SH} are extracted. As the annealing temperature increased, R_S displayed a decrease, which reflects the increase in the charge mobility in the PbS film, and R_{SH} showed a decrease, which implies that the carrier recombination increased.[27] Annealing at 200 ^{o}C caused a cell failure because the average inter-particle distance was increased and the network connectivity was reduced (*vide supra*), thus suppressing the carrier mobility. The optimal annealing condition in an Ar atmosphere was found to be 150 ^{o}C. Under this condition, the energy conversion efficiency (η) of the device was 3.57%, which is 39% better than that of the unannealed PbS film. Results for the bigger PbS QDs (QD E_g = 1.32 eV) in Figure 5.5b also show that annealing at 150 ^{o}C can enhance J_{sc} from 13.86 mA/cm^2 to 24.91 mA/cm^2. However, a significant tradeoff is evident between J_{sc} and V_{oc} during the annealing of larger PbS QD, presumably relating to the dramatically decreased band gaps.

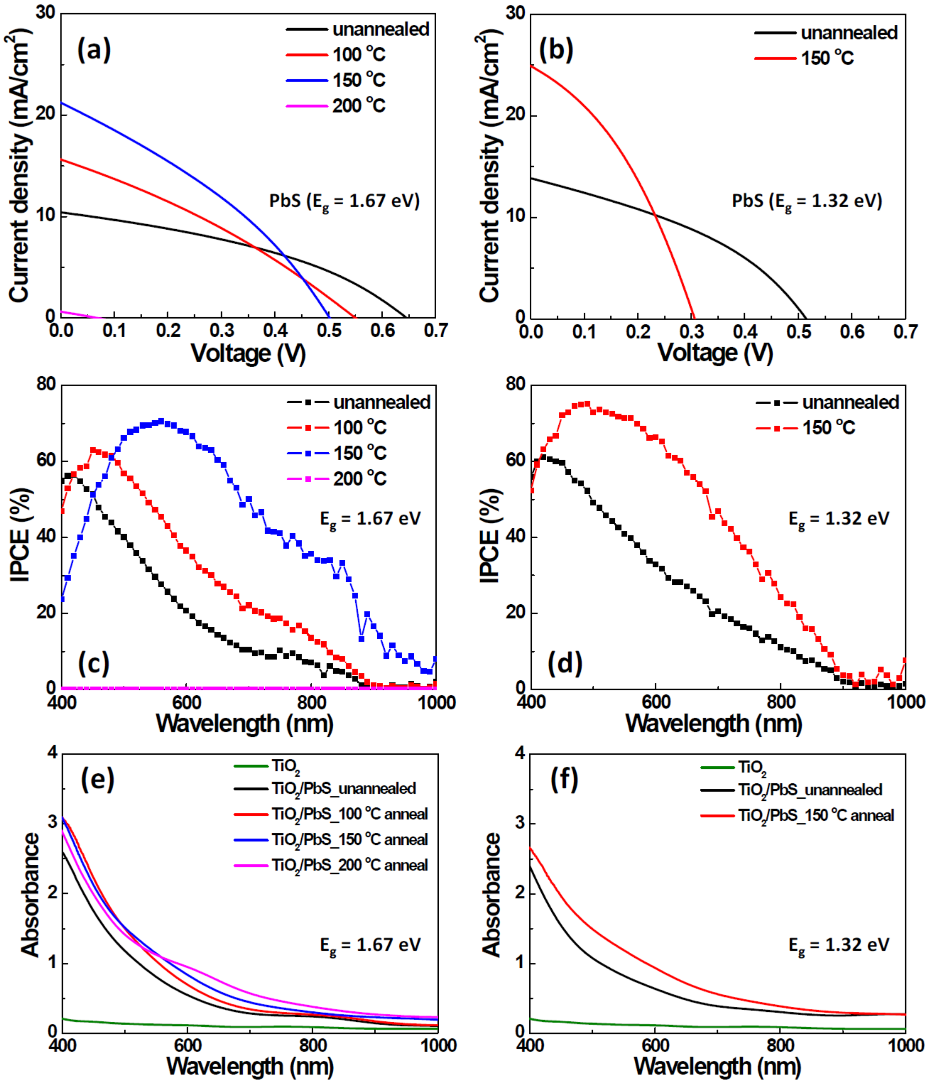

Figure 5-5. Current-Voltage (*J*-*V*) characteristics and incident photon-to-electron conversion efficiency (IPCE) spectra are shown for devices using unannealed PbS films and PbS films annealed at various temperatures. Optical absorbance spectra are shown for the TiO_2 and TiO_2/PbS films. (a, c, e) QD E_g = 1.67 eV, (b, d, f) QD E_g = 1.32 eV.

The incident photon-to-electron conversion efficiency (IPCE) curves of the solar cells are shown in Figure 5.5c. As the annealing temperature increases, a continuous redshift of the main

IPCE peak from 400 nm to 550 nm can be observed, and the hump at around 780 nm gradually broadens. Furthermore, more photons in the visible and near IR region are converted to electrons in the device after annealing. These changes correspond with the absorbance spectra of the TiO_2/PbS stack films (Figure 5.5e). The unannealed sample shows a small hump at around 780 nm, which red-shifts a little from the original first excitonic position, presumably because of coupling between neighboring QDs and the increased dielectric constant of the external environment.[34] After annealing, this hump becomes flatter and another broad absorption occurs in the visible regime from 500 nm to 700 nm. A similar behavior has been observed in one-dimensional PbS nanostructures, like nanorods.[35, 36] The IPCE and absorbance spectra (Figure 5.5d,f) of the control devices, which use PbS QDs (QD E_g = 1.32 eV) also show a comparable result, where annealing can enhance the light harvesting in the visible regime. Comparing the performance of the device using smaller PbS (QD E_g = 1.67 eV) annealed at 150 ^oC and bigger PbS (QD E_g = 1.32 eV) without annealing, it can be seen that their V_{oc} is close, which means a similar value for the film band gap. However, the shape of their IPCE curves is tremendously different, which reveals that some extra effect, besides the band gap, causes the enhancement of the photon-electron conversion efficiency.

Table 5.2. Response of FTO/TiO_2/PbS/Au Solar Cells under Simulated AM 1.5 (100 mW/cm^2).

PbS based PV	J_{sc} (mA/cm^2)	V_{oc} (V)	FF (%)	η (%)	R_S (Ω cm^2)	R_{SH} (Ω cm^2)
Unannealed (E_g = 1.67 eV)	10.41	0.65	38	2.57	25.7	151
annealed at 100 °C (E_g = 1.67 eV)	15.63	0.55	31	2.66	20.5	58.7
annealed at 150 °C (E_g = 1.67 eV)	21.23	0.50	33	3.57	13.6	39.8
annealed at 200 °C (E_g = 1.67 eV)	0.61	0.07	24	0.01	---	---
unannealed (E_g = 1.32 eV)	13.86	0.52	38	2.68	9.0	72.7
annealed at 150 °C (E_g = 1.32 eV)	24.91	0.31	36	2.79	3.8	42.6

5.3.4 DBH Structure at a PbS/TiO_2 Interface after Thermal Annealing

High-resolution transmission electron microscopy (HRTEM) was employed to examine the changes in the film's structure on the tens to hundreds of nanometer length scale (QD E_g = 1.67 eV) as a result of thermal annealing. In the bright field cross-section images of unannealed samples (Figure 5.6a), a boundary between the TiO_2 and PbS films is located at 200 nm from the PbS/Au interface, which is consistent with a previous report.[19] However, after 150 °C annealing, about 75% of the PbS QDs have moved into the TiO_2 mesoporous film and the interface between the two films has become diffuse (Figure 5.6b). This intermixing of PbS and TiO_2 implies the formation of a DBH structure. In the dark field cross-section images (Figure 5.6c-d), an intermixing region is clearly observed. Red bars are drawn to mark the width of the intermixing region. The narrow red bar on the unannealed sample arises from a slight penetration of the PbS

QDs or an overlap of TiO_2 and PbS films along the electron beam direction. The red bar of the annealed sample is as large as 300 nm, which is larger than the thickness of the pristine PbS film.

Energy dispersive X-ray spectroscopy (EDS) mapping of the 150 ^{o}C-annealed samples reveals clear evidence of the DBH structure. A rectangular area in the Z-contrast high angle annular dark field (HADDF) cross section image of Figure 5.6e was chosen for elemental distribution scanning. The red curve was drawn to roughly show the boundary between the pure PbS layer and TiO_2/PbS intermixing region. The elements Pb, S and O are traced in the selected area, which includes the zig-zag boundary. Non-uniformly dispersed Pb and S in the TiO_2 matrix indicates that the very small white dots of the HADDF image marked by yellow arrows are PbS QDs distributed in the TiO_2 film. This leads to the conclusion that the DBH of PbS QDs and TiO_2 nanoparticles was formed in the intermixing region. Because the cross-section was cleaned by ion milling, any contamination from the environment, such as dust, is very unlikely. The clean surface of the unannealed sample in Figure 5.6c verifies this assumption. In comparison, the EDS mapping of the unannealed sample indicates that no PbS diffusion is detected in the TiO_2 film (Figure C5).

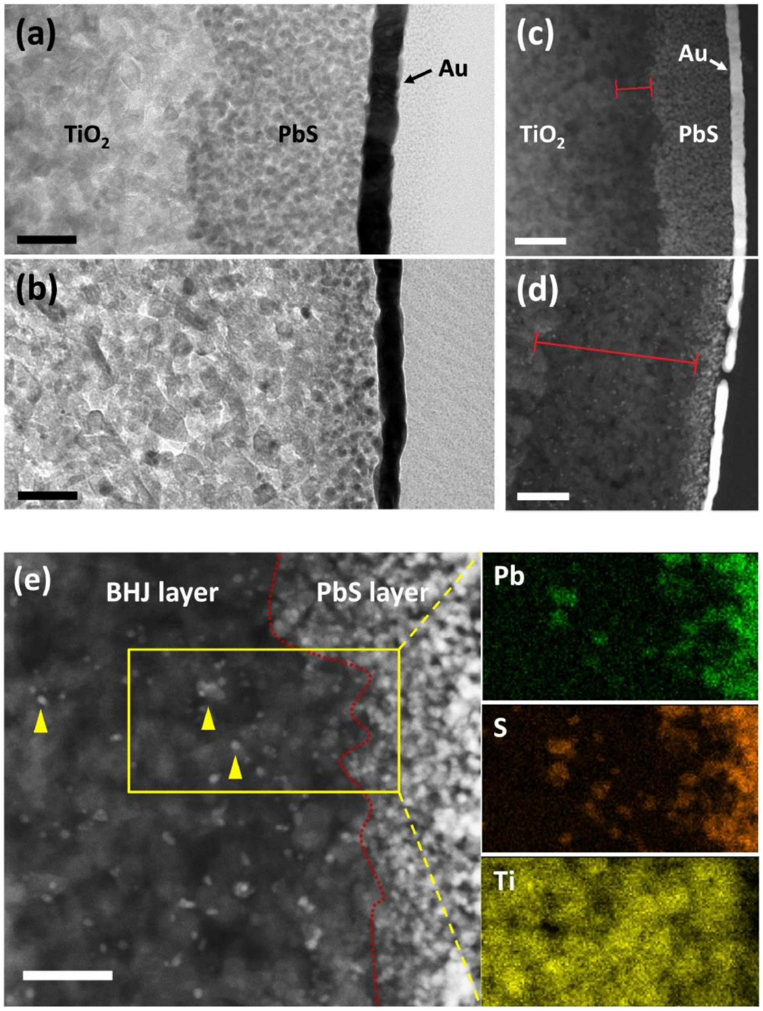

Figure 5-6. Bright field HRTEM cross-section images are shown for (a) an unannealed sample and (b) a sample annealed at 150 °C for 10 min. The scale bar is 50 nm. A Z-contrast high angle annular dark field (HADDF) cross-section image is shown for (c) an unannealed sample and (d) a sample annealed at 150 °C for 10 min. The scale bar is 100 nm. The inserted red bar shows the width of the PbS layer diffused into TiO_2 film. (e) A HADDF image and EDS mapping are shown for a sample annealed at 150 °C. The inserted yellow arrows show the individual PbS QDs in the TiO_2 mesoporous film. The red curve roughly shows the boundary between the pure PbS layer and the DBH layer. The scale bar is 50 nm.

This DBH structure is, in some sense, similar to the QD sensitized solar cell, in which photosensitizers attach on the TiO_2 NPs.[37, 38] However, in a QD sensitized solar cell, an electrolyte is needed for hole transport.[39] For this DBH device, no extra electrolyte is needed, and the residual upper pure PbS layer is in direct ohmic contact with the metallic anode. Figure 5.7 shows the schematic structures and mechanisms of the device using unannealed TiO_2/PbS films and TiO_2/PbS films annealed at 150 ^{o}C for 10 min in Ar. These reveal that after annealing, most of the PbS QDs diffuse into the TiO_2 mesoporous film along the pore channels. Inter-particle necking between QDs forms bridges for hole transport. By doing so, the active QDs layer expands.

A mechanism for charge separation and transport is shown by the diagrams in the inset. For the unannealed sample, a planar heterojunction occurs only at the TiO_2/PbS interface; and after charge separation, hole transport occurs by hopping between the adjacent QDs, which is not very efficient. For the annealed sample, however, a three-dimensional DBH with a highly folded architecture is generated such that most excitons are formed close to a junction interface. This exponentially increases the contact area between TiO_2 NPs and PbS QDs so as to enhance the generated carrier concentration. The interconnected QDs can then establish internal paths for efficient hole transfer. As a result, the light harvesting efficiency and charge injection efficiency are enhanced, leading to an improved J_{sc}.

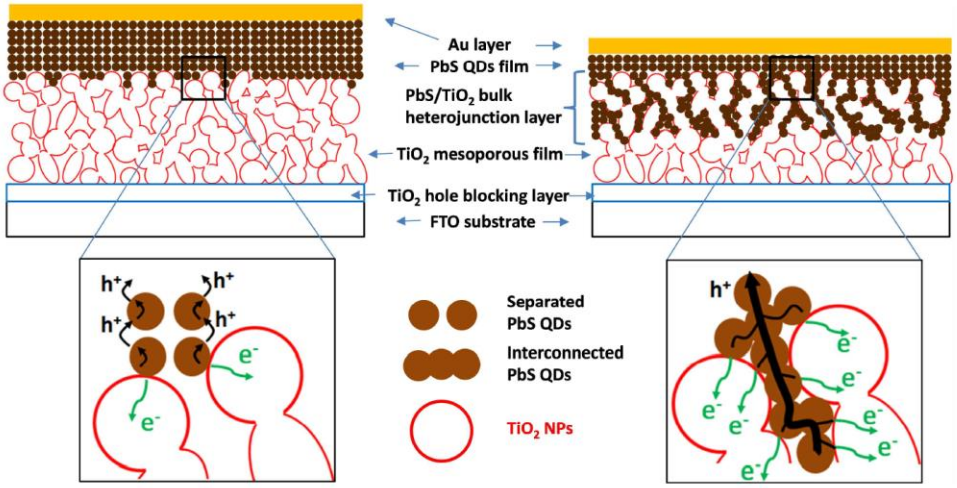

Figure 5-7. These schematic diagrams illustrate the structures and mechanisms of the devices using (left) unannealed TiO_2/PbS films and (right) TiO_2/PbS films annealed at 150 ^oC for 10 min in Ar; the PbS/TiO_2 bulk heterojunction layer was formed after annealing. Mechanisms of charge separation and transport are shown in the insets. (left) Carrier separation in the planar heterojunction proceeds by hole hopping between separated PbS QDs. (right) For the DBH structure, carrier separation is dominated by internal pathways of the interconnected PbS QDs.

5.3.5 Electric Force Microscope Analysis

Electrostatic force microscopy (EFM) is mainly devoted to detecting voltage contrasts and capacitive coupling using a force signal F_{Ω}, which is different from the surface topography.[40,41,42] In a true DBH, it is expected that a local property such as charge distribution can be used to characterize the charge transport on the nanoscale. Figure 5.8 shows the topography and charge distribution of the PbS film, which belongs to the FTO/TiO_2/PbS multilayer films, before (Figure 5.8a-b) and after (Figure 5.8c-d) annealing at 150 ^oC. The charge distribution was monitored under an electric bias of 5 V using a boron-doped diamond probe. The electric signal was amplified at a gain ratio of 10^6 A/V to increase the accuracy of the electric measurement. The images in 8c and 8d reveal that after annealing, the upper surface of the PbS film becomes smoother - presumably because of the densification of the film. It can be noted that local fluctuations at the nanoscale are found only in the EFM images of Figure 5.8d. The brighter islands with a peak signal of ~2.2 V in the annealed sample represent better hole transport and higher charge concentration in the local domain of the film. This local fluctuation of hole transport indicates that a DBH is formed in the intermixing region with an individual domain size of 50 nm to 100 nm and that holes and electrons have different transport channels underneath the PbS layer. These images should be contrasted with 8a and 8b before annealing, in which the carrier concentration is uniform and the average amplitude of 0.5 V corresponds to the planar heterojunction at the TiO_2/PbS interface.

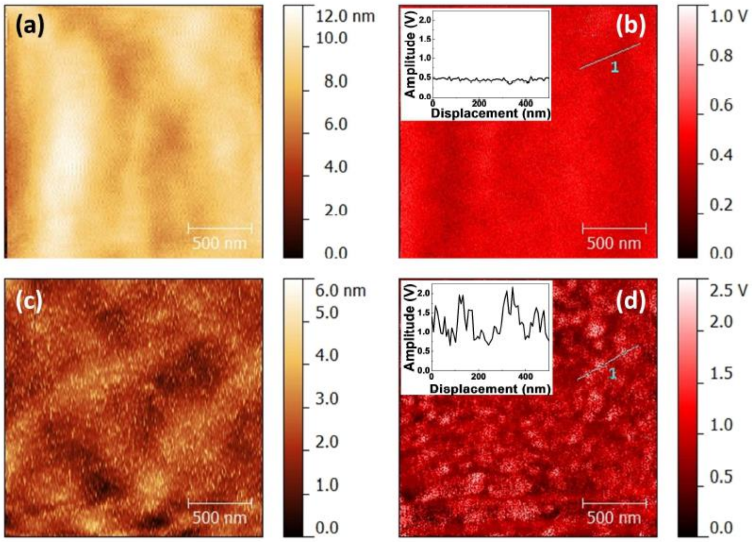

Figure 5-8. EFM data are shown for measurements of PbS/TiO_2 tandem films on FTO using a boron-doped diamond probe. (a) Topography and (b) charge distribution of unannealed sample. (c) Topography and (d) charge distribution of sample annealed at 150 ^{o}C for 10 min in Ar.

5.3.6 Electrochemical Impedance Spectroscopy and Electron Lifetime Measurement

Electrochemical impedance spectroscopy (EIS) was performed to analyze the internal electrical parameters of the devices, and the results are shown in Figure 5.9. In the thin film type PbS QD solar cells, low frequency responses ranging from ~kHz to mHz arise from the TiO_2/PbS interface.[20] The capacitance-voltage curve of the devices was measured in the dark using an impedance-potential scan.[43] The data in Figure 5.9a indicate charge transfer in the depletion layer at the TiO_2/PbS interface.[19] A larger capacitance after annealing means that more electrons are stored at the junction of the TiO_2/PbS interface. Nyquist plots of the devices are shown in Figure 5.9b and 9c. In order to study the TiO_2/PbS interface, complex impedance was measured from 0.1 Hz to 1 kHz for both dark and illuminated conditions at the open circuit voltage. As the annealing temperature increases, the radius of the semicircle decreases, indicating a decrease in the recombination resistance at the TiO_2/PbS interface. EIS data is fitted with a model of two sub-circuits that are composed of one constant phase element (CPE) in parallel with one resistance. This sub-circuit is called a ZARC element and Levenberg-Marquardt least-square data fitting program for windows (LEVMW, Chapel Hill, NC, US) was used for the fitting.[44] In Figure 5.9, the experimental (open circle) data are consistent with the fitted (solid line) one. The inset in Figure 5.9b shows a magnification of the plots in the low impedance regime. After analysis, the recombination resistances in the dark condition for the unannealed, 100 ^{o}C annealed, and 150 ^{o}C annealed samples are 42996 **Ω**, 16278 **Ω**, and 1207 **Ω**, respectively; under illumination the resistances are 518 **Ω**, 397 **Ω**, and 190 **Ω**, respectively. A monotonous decrease in the impedance with an increase in annealing temperature indicates that annealing lowers the carrier recombination resistance and shortens the carrier lifetime.

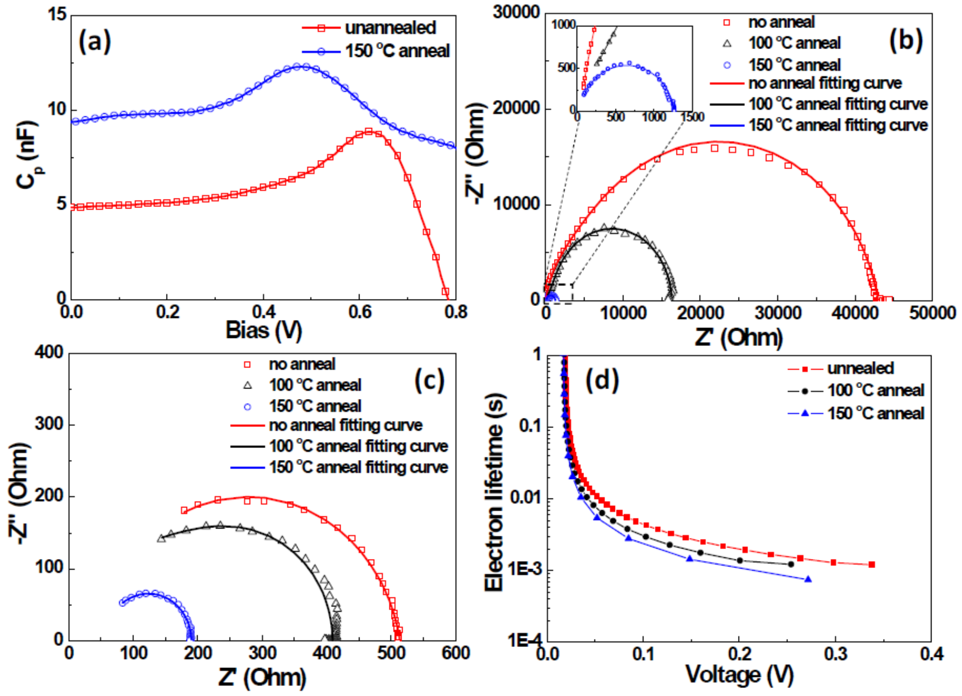

Figure 5-9. (a) A capacitance-voltage curve is shown for the FTO/TiO_2/1.67 eV QD/Au device. The capacitance (C_p) was calculated from the scanned impedance at 100 Hz with an AC signal of 25 mV in the dark. Nyquist plots of the unannealed and annealed devices tested in the low frequency regime ranging from 0.1 Hz to 1 kHz. The semi-circles were scanned in (b) dark and (c) illuminated conditions under an external bias with a magnitude of open circuit voltage. Experimental data (open circle) and fitted curve (solid line) are drawn together. The insert shows the magnified plots in the low impedance regime. (d) Electron lifetime of the devices using PbS films with and without annealing.

The electron lifetime (τ) of the devices using PbS films with or without annealing was measured using an open-circuit voltage decay (OCVD) technique.[45] The transient of V_{oc} was measured as a function of time using a 633 nm photodiode laser as the light source, and the lifetime in the different devices was calculated from the decay curves of V_{oc}. In Figure 5.9d, it is clearly shown that τ decreases with increasing annealing temperature. As the samples were thermally annealed, the τ became smaller, which is consistent with the results of the impedance measurement. The device using bigger QDs (QD E_g = 1.32 eV) had an even lower τ, with a similar temperature-dependent feature; see Figure C6.

The decrease in the recombination resistance and in the electron lifetime after annealing can be explained by an increase of the TiO_2/PbS interface area. As the interface area increases because of the thermal annealing, the probability of carrier trapping and recombination increases. This effect leads to a decrease in the carrier lifetime, which supports our model of the DBH between TiO_2 and PbS. In addition, a decrease in the bandgap of the semiconductor by the thermal annealing increases the Auger recombination rate and decreases the carrier lifetime.[46] Detachment of the short EDT ligand and insufficient surface passivation during thermal annealing is also partially responsible for a smaller carrier lifetime. This implies that a retreatment of thermally annealed PbS film in EDT should improve passivation of the QD surface, reduce the recombination sites, and improve the device performance. The *J*-*V* curves of the device using 150 ^{o}C annealed PbS film and 150 ^{o}C annealed/EDT treated PbS film are shown in Figure 5.10. When the annealed PbS film was repassivated by dipping the film in an EDT/acetonitrile solution for another 30 sec, the FF of the device improved from 0.32 to 0.36, indicating a suppressed recombination rate. The conversion efficiency then increased from 3.57% to 3.95%.

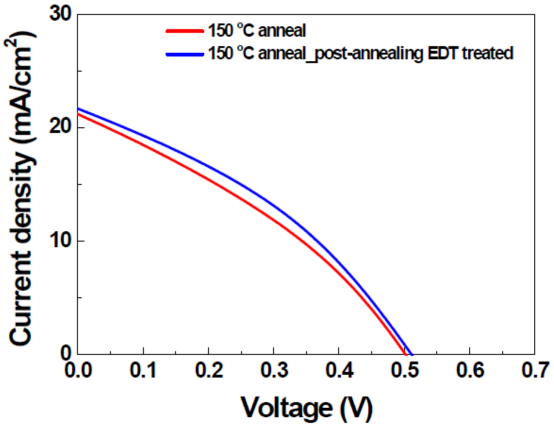

Figure 5-10. *J-V* curve of the devices using PbS film annealed at 150 ^{o}C and without or with post-annealing EDT treatment.

5.4 Conclusion

The thermal annealing effect on the performance characteristics of aTiO$_2$/PbS heterojunction solar cell was explored. TEM, EFM, and AFM analysis showed that mild annealing of the thin film solar cell at 150 ^{o}C under an inert atmosphere caused the intermixing of PbS QDs and TiO$_2$ nanoparticles and the formation of a DBH layer. An increase in the junction interface between PbS and TiO$_2$ was found to facilitate electron-hole separation. Annealing also improved the crystallinity of the PbS QDs and introduced a necking structure between adjacent QDs. As a result, the carrier transport at the PbS/TiO$_2$ interface became faster and the current density and conversion efficiency of the device was improved.

5.5 REFERENCES

1. Talapin, D. V.; Lee, J. S.; Kovalenko, M. V.; Shevchenko, E. V., Prospects of Colloidal Nanocrystals for Electronic and Optoelectronic Applications. *Chem. Rev.* **2010**, *110*, 389-458.

2. Tang, J. A.; Sargent, E. H., Infrared Colloidal Quantum Dots for Photovoltaics: Fundamentals and Recent Progress. *Adv. Mater.* **2011**, *23*, 12-29.

3. Talapin, D. V.; Murray, C. B., PbSe nanocrystal solids for n- and p-channel thin film field-effect transistors. *Science* **2005**, *310*, 86-89.

4. Hines, M. A.; Scholes, G. D., Colloidal PbS nanocrystals with size-tunable near-infrared emission: Observation of post-synthesis self-narrowing of the particle size distribution. *Adv. Mater.* **2003**, *15*, 1844-1849.

5. McDonald, S. A.; Konstantatos, G.; Zhang, S. G.; Cyr, P. W.; Klem, E. J. D.; Levina, L.; Sargent, E. H., Solution-processed PbS quantum dot infrared photodetectors and photovoltaics. *Nat. Mater.* **2005**, *4*, 138-142.

6. Nozik, A. J., Spectroscopy and hot electron relaxation dynamics in semiconductor quantum wells and quantum dots. *Annu. Rev. Phys. Chem.* **2001**, *52*, 193-231.

7. Nozik, A. J., Quantum dot solar cells. *Physica E* **2002**, *14*, 115-120.

8. Ellingson, R. J.; Beard, M. C.; Johnson, J. C.; Yu, P. R.; Micic, O. I.; Nozik, A. J.; Shabaev, A.; Efros, A. L., Highly efficient multiple exciton generation in colloidal PbSe and PbS quantum dots. *Nano Lett.* **2005**, *5*, 865-871.

9. Sukhovatkin, V.; Hinds, S.; Brzozowski, L.; Sargent, E. H., Colloidal Quantum-Dot Photodetectors Exploiting Multiexciton Generation. *Science* **2009**, *324*, 1542-1544.

10. Sambur, J. B.; Novet, T.; Parkinson, B. A., Multiple Exciton Collection in a Sensitized Photovoltaic System. *Science* **2010**, *330*, 63-66.

11. Semonin, O. E.; Luther, J. M.; Choi, S.; Chen, H. Y.; Gao, J. B.; Nozik, A. J.; Beard, M. C., Peak External Photocurrent Quantum Efficiency Exceeding 100% via MEG in a Quantum Dot Solar Cell. *Science* **2011**, *334*, 1530-1533.

12. Sargent, E. H., Solar Cells, Photodetectors, and Optical Sources from Infrared Colloidal Quantum Dots. *Adv. Mater.* **2008**, *20*, 3958-3964.

13. Klem, E. J. D.; MacNeil, D. D.; Levina, L.; Sargent, E. H., Solution processed photovoltaic devices with 2% infrared monochromatic power conversion efficiency: Performance optimization and oxide formation. *Adv. Mater.* **2008**, *20*, 3433-3439.

14. Koleilat, G. I.; Levina, L.; Shukla, H.; Myrskog, S. H.; Hinds, S.; Pattantyus-Abraham, A. G.; Sargent, E. H., Efficient, stable infrared photovoltaics based on solution-cast colloidal quantum dots. *Acs Nano* **2008**, *2*, 833-840.

15. Law, M.; Beard, M. C.; Choi, S.; Luther, J. M.; Hanna, M. C.; Nozik, A. J., Determining the Internal Quantum Efficiency of PbSe Nanocrystal Solar Cells with the Aid of an Optical Model. *Nano Lett* **2008**, *8,* 3904-3910.

16. Luther, J. M.; Law, M.; Beard, M. C.; Song, Q.; Reese, M. O.; Ellingson, R. J.; Nozik, A. J., Schottky Solar Cells Based on Colloidal Nanocrystal Films. *Nano Lett* **2008**, *8*, 3488-3492.

17. Law, M.; Luther, J. M.; Song, O.; Hughes, B. K.; Perkins, C. L.; Nozik, A. J., Structural, optical, and electrical properties of PbSe nanocrystal solids treated thermally or with simple amines. *J. Am. Chem. Soc.* **2008**, *130,* 5974-5985.

18. Luther, J. M.; Law, M.; Song, Q.; Perkins, C. L.; Beard, M. C.; Nozik, A. J., Structural, optical and electrical properties of self-assembled films of PbSe nanocrystals treated with 1,2-ethanedithiol. *ACS Nano* **2008**, *2*, 271-280.

19. Andras G. Pattantyus-Abraham, I. J. K., Aaron R. Barkhouse, Xihua Wang, Gerasimos Konstantatos, Ratan Debnath, Larissa Levina, Ines Raabe, Mohammad K. Nazeeruddin, Michael Gratzel, Edward H. Sargent, Depleted-Heterojunction Colloidal Quantum Dot Solar Cells. *ACS Nano* **2010**, *4*, 3374-3380.

20. Etgar, L.; Moehl, T.; Gabriel, S.; Hickey, S. G.; Eychmuller, A.; Gratzel, M., Light Energy Conversion by Mesoscopic PbS Quantum Dots/TiO2 Heterojunction Solar Cells. *ACS Nano* **2012**, *6*, 3092-3099.

21. Luther, J. M.; Gao, J. B.; Lloyd, M. T.; Semonin, O. E.; Beard, M. C.; Nozik, A. J., Stability Assessment on a 3% Bilayer PbS/ZnO Quantum Dot Heterojunction Solar Cell. *Adv. Mater.* **2010**, *22*, 3704-3707.

22. Gao, J. B.; Luther, J. M.; Semonin, O. E.; Ellingson, R. J.; Nozik, A. J.; Beard, M. C., Quantum Dot Size Dependent J-V Characteristics in Heterojunction ZnO/PbS Quantum Dot Solar Cells. *Nano Lett.* **2011**, *11*, 1002-1008.

23. Szendrei, K.; Gomulya, W.; Yarema, M.; Heiss, W.; Loi, M. A., PbS nanocrystal solar cells with high efficiency and fill factor. *Appl. Phys. Lett.* **2010**, *97*, 203501.

24. Klem, E. J. D.; Shukla, H.; Hinds, S.; MacNeil, D. D.; Levina, L.; Sargent, E. H., Impact of dithiol treatment and air annealing on the conductivity, mobility, and hole density in PbS colloidal quantum dot solids. *Appl. Phys. Lett.* **2008**, *92*, 212105.

25. Turyanska, L.; Elfurawi, U.; Li, M.; Fay, M. W.; Thomas, N. R.; Mann, S.; Blokland, J. H.; Christianen, P. C. M.; Patane, A., Tailoring the physical properties of thiol-capped PbS quantum dots by thermal annealing. *Nanotechnology* **2009**, *20*, 315604.

26. Baik, S. J.; Kim, K.; Lim, K. S.; Jung, S.; Park, Y. C.; Han, D. G.; Lim, S.; Yoo, S.; Jeong, S., Low-Temperature Annealing for Highly Conductive Lead Chalcogenide Quantum Dot Solids. *J. Phys. Chem. C* **2011**, *115*, 607-612.

27. Zhao, N.; Osedach, T. P.; Chang, L. Y.; Geyer, S. M.; Wanger, D.; Binda, M. T.; Arango, A. C.; Bawendi, M. G.; Bulovic, V., Colloidal PbS Quantum Dot Solar Cells with High Fill Factor. *ACS Nano* **2010,** *4*, 3743-3752.

28. Gao, J. B.; Jeong, S.; Lin, F.; Erslev, P. T.; Semonin, O. E.; Luther, J. M.; Beard, M. C., Improvement in carrier transport properties by mild thermal annealing of PbS quantum dot solar cells. *Appl. Phys. Lett.* **2013**, *102*, 043506.

29. Talapin, D. V.; Rogach, A. L.; Haase, M.; Weller, H., Evolution of an ensemble of nanoparticles in a colloidal solution: Theoretical study. *J. Phys. Chem. B* **2001**, *105*, 12278-12285.

30. Ridley, B. A.; Nivi, B.; Jacobson, J. M., All-inorganic field effect transistors fabricated by printing. *Science* **1999**, *286*, 746-749.

31. Lu, X. J.; Mou, X. L.; Wu, J. J.; Zhang, D. W.; Zhang, L. L.; Huang, F. Q.; Xu, F. F.; Huang, S. M., Improved-Performance Dye-Sensitized Solar Cells Using Nb-Doped TiO2 Electrodes: Efficient Electron Injection and Transfer. *Adv. Funct. Mater.* **2010**, *20*, 509-515.

32. Tang, J.; Brzozowski, L.; Barkhouse, D. A. R.; Wang, X. H.; Debnath, R.; Wolowiec, R.; Palmiano, E.; Levina, L.; Pattantyus-Abraham, A. G.; Jamakosmanovic, D.; Sargent, E. H., Quantum Dot Photovoltaics in the Extreme Quantum Confinement Regime: The Surface-Chemical Origins of Exceptional Air- and Light-Stability. *ACS Nano* **2010**, *4*, 869-878.

33. Johnston, K. W.; Pattantyus-Abraham, A. G.; Clifford, J. P.; Myrskog, S. H.; Hoogland, S.; Shukla, H.; Klem, J. D.; Levina, L.; Sargent, E. H., Efficient Schottky-quantum-dot photovoltaics: The roles of depletion, drift, and diffusion. *Appl. Phys. Lett.* **2008**, *92*, 122111.

34. Leatherdale, C. A.; Bawendi, M. G., Observation of solvatochromism in CdSe colloidal quantum dots. *Phys. Rev. B* **2001**, *63*, 165315.

35. Deng, B.; Zhong, S. L.; Wang, D. H.; Wang, S. S.; Zhang, T. K.; Qu, W. G.; Xu, A. W., High yield synthesis of matchstick-like PbS nanocrystals using mesoporous organosilica as template. *Nanoscale* **2011**, *3*, 1014-1021.

36. Huang, N. M.; Radiman, S.; Lim, H. N.; Yeong, S. K.; Khiew, P. S.; Chiu, W. S.; Kong, S. N.; Saeed, G. H. M., Synthesis and characterization of ultra small PbS nanorods in sucrose ester microemulsion. *Mater. Lett.* **2009**, *63*, 500-503.

37. Vogel, R.; Hoyer, P.; Weller, H., Quantum-Sized Pbs, Cds, Ag2s, Sb2s3, and Bi2s3 Particles as Sensitizers for Various Nanoporous Wide-Bandgap Semiconductors. *J. Phys. Chem.* **1994**, *98*, 3183-3188.

38. Lee, Y. L.; Lo, Y. S., Highly Efficient Quantum-Dot-Sensitized Solar Cell Based on Co-Sensitization of CdS/CdSe. *Adv. Funct. Mater.* **2009**, *19*, 604-609.

39. Lee, H.; Leventis, H. C.; Moon, S. J.; Chen, P.; Ito, S.; Haque, S. A.; Torres, T.; Nuesch, F.; Geiger, T.; Zakeeruddin, S. M.; Gratzel, M.; Nazeeruddin, M. K., PbS and US Quantum Dot-Sensitized Solid-State Solar Cells: "Old Concepts, New Results". *Adv. Funct. Mater*. **2009**, *19*, 2735-2742.

40. Girard, P., Electrostatic force microscopy: principles and some applications to semiconductors. *Nanotechnology* **2001**, *12*, 485-490.

41. Heim, T.; Lmimouni, K.; Vuillaume, D., Ambipolar charge injection and transport in a single pentacene monolayer island. *Nano Lett.* **2004**, *4*, 2145-2150.

42. Jiang, Y. P.; Qi, Q.; Wang, R.; Zhang, J.; Xue, Q. K.; Wang, C.; Jiang, C.; Qiu, X. H., Direct Observation and Measurement of Mobile Charge Carriers in a Monolayer Organic Semiconductor on a Dielectric Substrate. *ACS Nano* **2011**, *5*, 6195-6201.

43. Tang, J.; Kemp, K. W.; Hoogland, S.; Jeong, K. S.; Liu, H.; Levina, L.; Furukawa, M.; Wang, X. H.; Debnath, R.; Cha, D. K.; Chou, K. W.; Fischer, A.; Amassian, A.; Asbury, J. B.; Sargent, E. H., Colloidal-quantum-dot photovoltaics using atomic-ligand passivation. *Nat. Mater.* **2011**, *10*, 765-771.

44. Bonanos, N.; Pissis, P.; Macdonald, J. R., Impedance Spectroscopy of Dielectrics and Electronic Conductors, in: *Characterization of Materials*, Second Edition, John Wiley & Sons, **2012**.

45. Zaban, A.; Greenshtein, M.; Bisquert, J., Determination of the electron lifetime in nanocrystalline dye solar cells by open-circuit voltage decay measurements. *Chemphyschem* **2003**, *4*, 859-864.

46. Metzger, W. K.; Wanlass, M. W.; Ellingson, R. J.; Ahrenkiel, R. K.; Carapella, J. J., Auger recombination in low-band-gap n-type InGaAs. *Appl. Phys. Lett.* **2001**, *79*, 3272-3274.

47. Ding, B.; Lee, B. J.; Yang, M. J.; Jung, H. S.; Lee, J. K., Surface-Plasmon Assisted Energy Conversion in Dye-Sensitized Solar Cells. *Adv. Energy. Mater.* **2011**, *1*, 415-421.

6.0 CONCLUSION REMARKS AND FUTURE DIRECTIONS

Semiconductor nanoparticles (NPs) are a promising photovoltaic material for next-generation solar cells as discussed above, because of their size-tunable energetics, multiple exciton generation, solution-processibility, etc. The commercialization of NP photovoltaics will be a slow process, however; because there is a still wide gap between the laboratory discovery and the real world applications. This process is not surprising as many revolutionary technologies have experienced this stage before they reach commercialization. As a good sign, recently numerous startup companies have joined the race for NP devices and applications, such as QD vision. It suggests that the unique features of the NPs can not only attract scientific curiosity, but they can also be potentially profitable. The great interest for the NPs in both academia and industry will certainly accelerate the development of the NP-based applications. In the meantime, some scientific challenges need to be addressed by researchers, including 1) collective phenomena of the NP assemblies; 2) surface chemistry of the NPs; and 3) photo-induced charge generation, separation, and transfer processes in the NP and the NP-based devices.

This thesis has extensively explored those challenging areas by studying the electronic energetics, charge transfer kinetics, and photovoltaics for the semiconductor NP assemblies and devices. Chapter 2 shows that the electronic coupling between NPs and conductive substrates can largely alter the energetics of the NP. This result suggests that the previous knowledge obtained for isolated NPs may not be entirely accurate for use in NP assemblies and devices, in which the NP interacts with other components and exhibits collective electronic features. In addition, we found that the lifetime of excited electrons in the assembly is highly sensitive to the density of trap states, which can be manipulated by the choice of surface ligands. For future directions, we are interested in studying the electronic coupling between the NP and different substrates other than Au. This study may explain the mechanism for the HOMO-pinning effect by revealing the relation between the pinning position and the metal work function.

Chapter 3 demonstrates how the energy architecture can influence the charge transport and photocurrent generation in a model photoelectrochemical cell and a real photovoltaic device. Photocurrent was used as a simple tool to study how the energy level alignments affect the charge transfer directionality and efficiency. The experiments with the photoelectrochemical cell obtained valuable information for the design of a real photovoltaic device, while using a minimum amount of materials and time. This work provides an interesting strategy to optimize the energy alignments and architectures for the devices by simply testing them first in a photoelectrochemical cell.

The charge transfer study in Chapter 4 suggests a strategy for enhancing the charge separation in hybrid solar cells by orienting an internal electric field with the donor-acceptor energy offset. This strategy may offer some new ideas for synthesizing polymers (side chains) and NP ligands that have a right dipole moment at their donor-acceptor interface. This dipole moment can work with the donor-acceptor energy offsets as the charge separation "engine" for the hybrid bulk heterojunction devices. For future directions, we want to explore other interfacial factors which can also affect the charge separation and recombination kinetics. For instance, several researchers have reported that chiral molecules, such as DNA, are highly spin-selective; and thus they are conductive for electrons with one spin direction, but resistant for electrons with the other spin direction. For a hybrid polymer/NP system with a chiral polymer side chain and a chiral NP ligand, it is very interesting to see how different chirality combinations can affect the charge transfer rate between the polymer and the NP.

What exactly can thermal annealing do for a NP-based solar cell? Chapter 5 addresses this question by annealing a PbS-NP/TiO_2 depleted heterojunction device at different temperatures and monitoring the micro-structural change of the heterojunction. This work shows that thermal annealing at an optimal temperature can cause the intermixing of p-type and n-type materials at the interface. This intermixing increases the charge-separating area and thus enhances the charge separation efficiency. For future directions, we are interested in studying how to use surface plasmon to enhance the absorption of PbS NPs in a similar device. By using Au/SiO_2 core-shell plasmonic nanostructures, our preliminary experimental and simulation results show that embedding the Au/SiO_2 nanostructures into the PbS-NP film in a depleted heterojunction cell can improve the power conversion efficiency by ~ 24%. This enhancement may be attributed to both localized surface plasmon and enhanced light scattering resulting from the Au/SiO_2 nanostructures.

In summary, the studies in this thesis provide some insights about the photophysics of semiconductor NPs and their electronic interactions with metals, surface ligands, or conjugated polymers. The important findings may help other researchers to better understand the fundamental physics for semiconductor nanoparticles.

APPENDIX A

Supporting information for Chapter 2

In Figure A1, Panel A shows that the LEPET signal increases as the NP incubation time increases from 10 min to 3 h, namely, increasing the M-NP coverage on Au/DT. This result confirms that these photoelectron kinetic energy distributions are from the NPs in the assemblies. Panel B has all spectra in Panel A rescaled to demonstrate that varying the NP coverage does not alter the high energy cut-off of the spectra, namely, the HOMO energy. However, the little change in lower kinetic energy cut-off indicates the coverage does alter the work function of the NP assemblies.

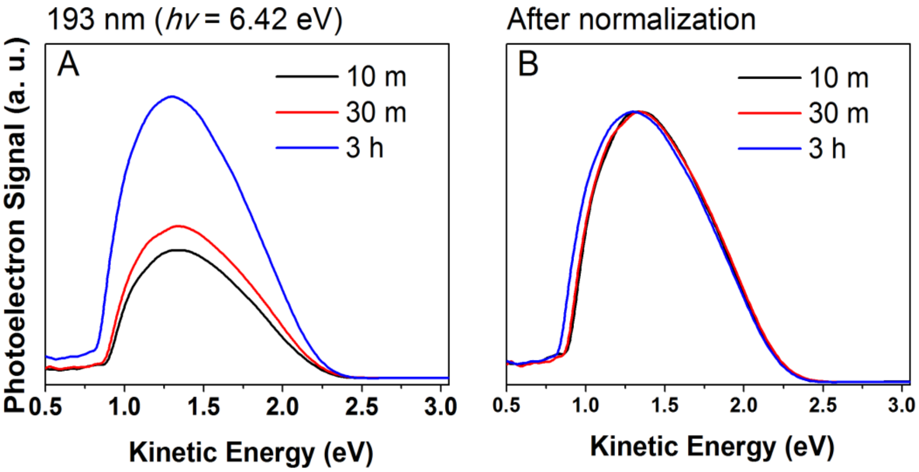

Figure A1. Panel A shows that the LEPET signals increase with the M-NP incubation time from 10 m to 3 h. Panel B has all the spectra in panel A rescaled to the same height. The signal of Au/DT has been subtracted from all the spectra here.

Figure A2 shows the TPPE spectra for the assemblies of Au/DT/NP for three sizes of NPs. The peak energy in the TPPE spectra is generally assigned to the LUMO. However, the peak observed at a kinetic energy of about 1.0 eV is not the LUMO of the NPs, because it is neither consistent with the LUMO energy calculated from the HOMO energy and the optical bandgap, nor is it correlated with the NP size.

The kinetic energy (E_k) of photoelectrons ejected from the LUMO is, $E_k = hv - E_b$, where hv is the second photon energy, and E_b is the binding energy of the LUMO. Based on this equation, one expects that the peak of the LUMO should shift one-fold with the change of the second photon energy. However, as shown in Figure A2, the peak obtained does not shift with the second photon energy, and it occurs at almost the same kinetic energy for all three sizes of the NPs. Thus, this peak is not the LUMO level, and it is likely caused by the secondary electrons produced by the laser.

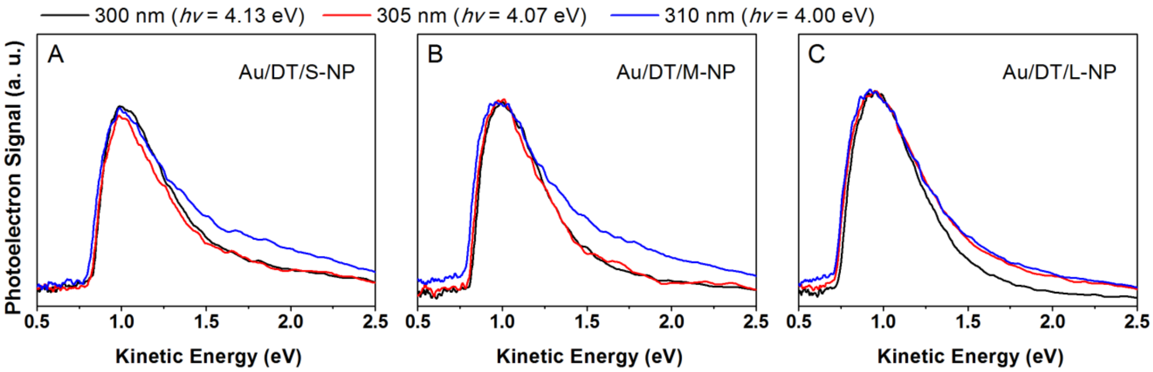

Figure A2. The TPPE spectra for Au/DT/S-NP (A), Au/DT/M-NP (B), and Au/DT/L-NP (C) at three excitation wavelengths of 300 nm (black), 305 nm (red) and 310 nm (blue).

Figure A3 compares the TPPE spectra between the assemblies of Au/DT/NP and Au/DT/NP/DT for three sizes of the CdTe NPs. These spectra were collected at three different wavelengths. The data show that the ligand exchange from TDPA to DT introduced a high kinetic energy shoulder in the TPPE spectra that corresponds to the photoelectrons ejected from the LUMO of the NPs by the second photon.

The energy distance (ΔE) between the LUMO and the Fermi level is calculated as: $\Delta E = \Phi - (hv - \Delta E_k)$. Φ is the work function measured from LEPET, and it is equal to the difference between the photon energy used in LEPET and the width of the LEPET spectra; hv is the second photon energy in TPPE; and ΔE_k is the kinetic energy difference between the peak energy and the low energy cut-off in the spectrum of TPPE.

The high surface coverage of the L-NPs make its low kinetic energy peak much more dominating in the TPPE spectrum than that in case of the S- or M-NPs, which have a lower surface coverage than the L-NPs. This fact leads to a less well-defined high kinetic energy shoulder for the L-NPs than that for the S- or M-NPs. Thus, the subtraction of the low kinetic energy peak results in a narrower LUMO distribution for the L-NPs than that for the S- or M-MPs, as shown in Figure 2.3C.

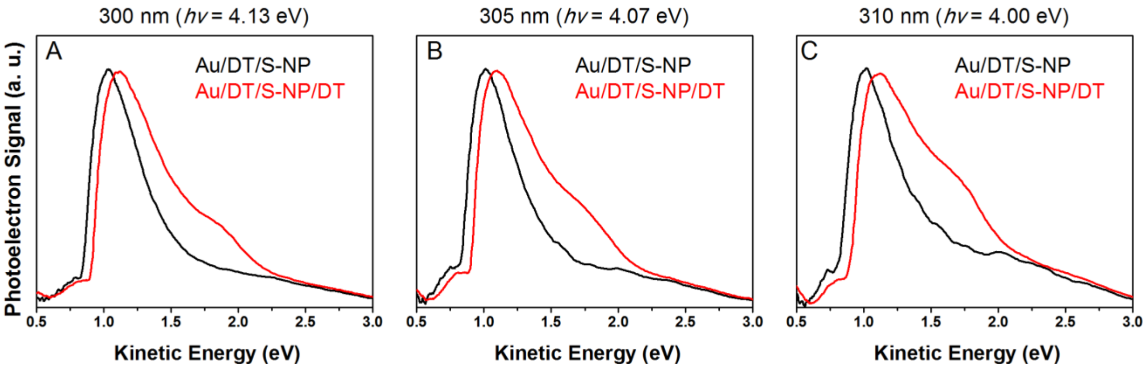

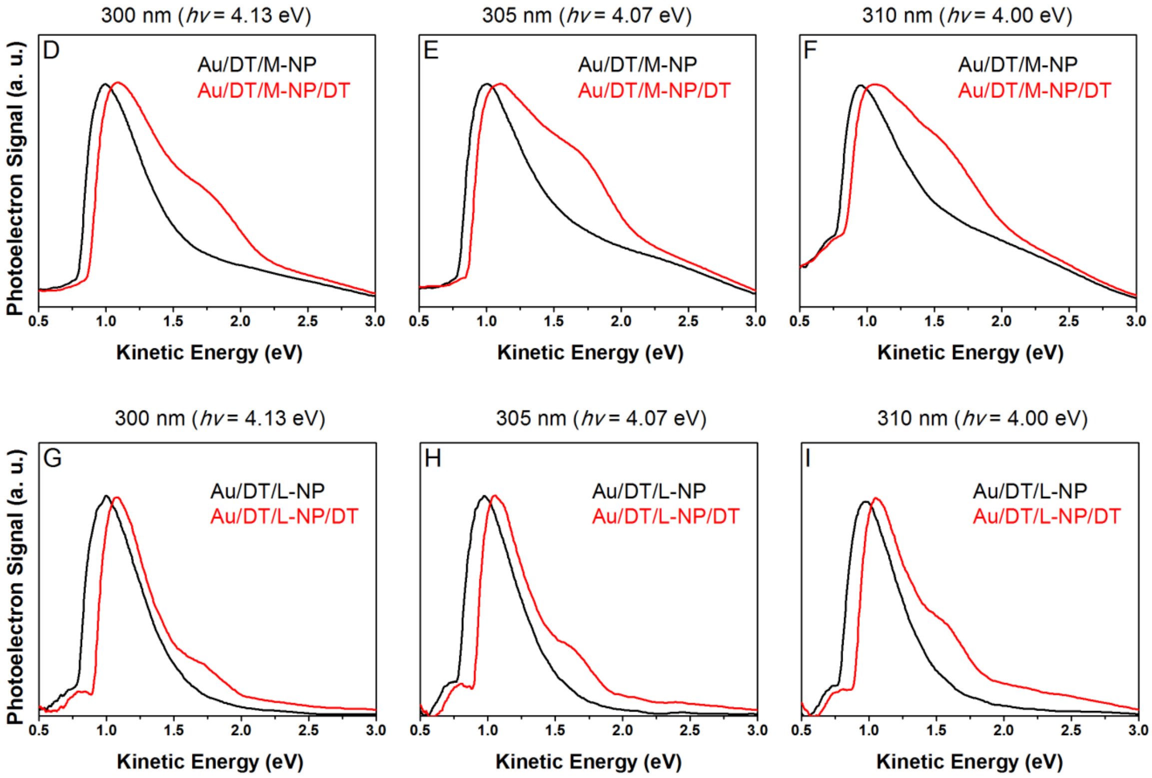

Figure A3. Panels A to C compare the TPPE spectra for the assemblies of Au/DT/S-NP (black) and Au/DT/S-NP/DT (red) collected at a wavelength of 300 nm (left), 305 nm (middle), and 310 nm (right). Correspondingly, Panels D to F and Panels G to I are the spectra for the assemblies with M-NP and L-NP, respectively.

The surface photoluminescence (PL) measurements on the assemblies of Au/DT/NP show that the fluorescence for all sizes of NPs was completely quenched. Figure A4 shows the surface PL spectra for the assemblies of Au/DT/NP/DT after replacing TDPA with DT. Interestingly, all NP assemblies show PL after this treatment. This result indicates that presumably by removing the surface states the DT ligands can also enhance the PL yield for the NPs.

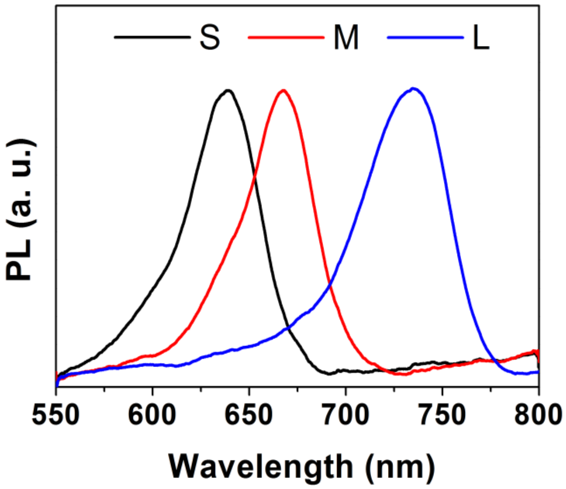

Figure A4. This figure shows the normalized surface PL spectra for three different assemblies, Au/DT/S-NP/DT (black), Au/DT/M-NP/DT (red), and Au/DT/L-NP/DT (blue) after the ligand exchange.

Figure A5 compares the background-subtracted LEPET spectra for the assemblies of Au/DT/NP and Au/DT/NP/DT. The data show that the attachment of the second layer of DT does not significantly alter the energies of the HOMO; namely, the HOMO level for all sizes of NPs remains pinned at 0.80 ± 0.05 eV below the Fermi level. However, the DT molecules do change the low energy cut-off of the spectra and the width of the spectra by about 0.1 eV. Because the work function (Φ) is equal to the difference between the photon energy used in LEPET and the width of the spectra, thus the work function of the assemblies is changed from 4.2 ± 0.1 eV to 4.3 ± 0.1 eV after replacing the TDPA with the DT.

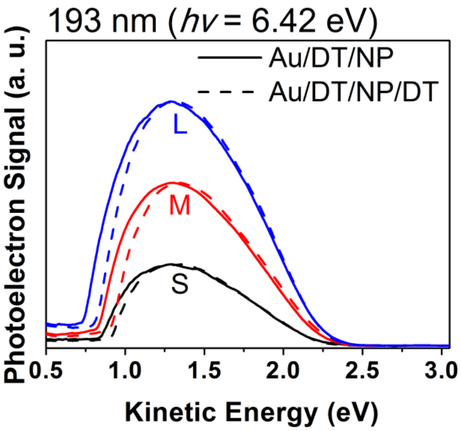

Figure A5. This figure compares the LEPET spectra of the Au/DT/NP and Au/DT/NP/DT for all sizes of NPs. The assemblies of Au/DT/NP are shown as the solid lines, and those of Au/DT/NP/DT are shown as the dashed lines.

Figure A6 shows the voltammetry results for the three sizes of CdTe NPs that were originally synthesized in the aqueous phase with a water-soluble thiol ligand (3-Mercaptopropionic acid, MPA). Compared to the results in Figure 6, these data indicate that the thiol ligand completely removed the peak O1 which is assigned to be from the trap states. This observation is consistent with the view that thiol ligands suppress the interband surface states of the CdTe NPs. In addition, the potential of the only oxidation peak observed in Figure A6 agrees with that of Peak O2 observed in Figure 2.6. This agreement suggests that peak O2 is caused by the oxidation of the NP valence band.

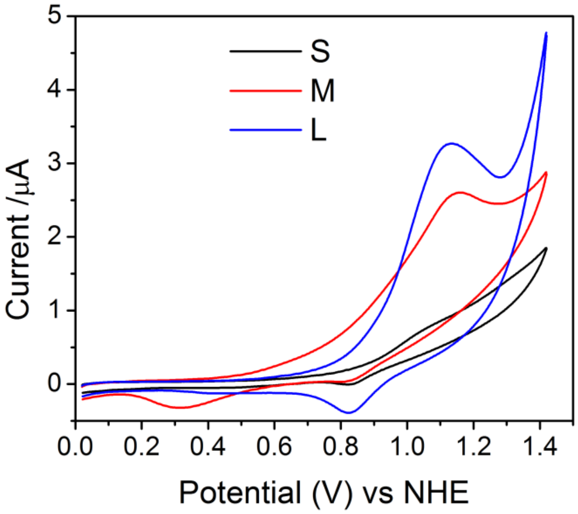

Figure A6. Voltammograms of the three sizes of MPA-CdTe NPs immobilized on the Au/DT electrode. The measurement was performed in 0.1 M aqueous phosphate buffer solution (pH = 3).

Figure A7 only plots the oxidation wave of the voltammograms shown in Figure 2.6. The dash lines are the simulated base lines which will be subtracted from each corresponding oxidation wave. The subtraction results are shown as the solid lines in Figure 2.7. This purpose of this subtraction is to minimize the charging current influence on the shape of the oxidation peaks, and to achieve a good Gaussian fitting to the oxidation peak O1.

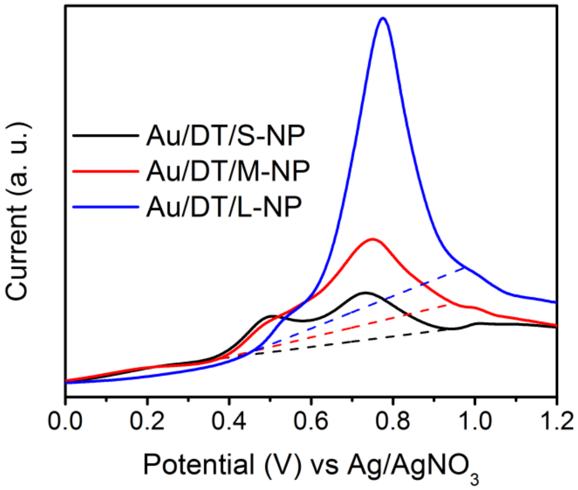

Figure A7. Compared to Figure 2.6, this figure only plots the oxidation wave of the voltammogram for the assembly of Au/DT/S-NP (black), Au/DT/M-NP (red), and Au/DT/L-NP (blue). The dash lines are the simulated baselines that will be subtracted from the oxidation wave to extract peak O1 and O2.

Figure A8 shows photocurrent density-voltage (*J*-V) characteristics for the assemblies with different NP incubation times, from 0.5 h to 3h, and presumably different NP surface coverage on Au. These data show that 1) the photocurrent increases as the NP incubation time increases from 0.5 h to 3 h; and 2) with the same incubation time, the photocurrent for the Au/DT/M-NP/DT assemblies (dash lines) are at least four times higher than that for the corresponding Au/DT/M-NP assemblies (solid lines).

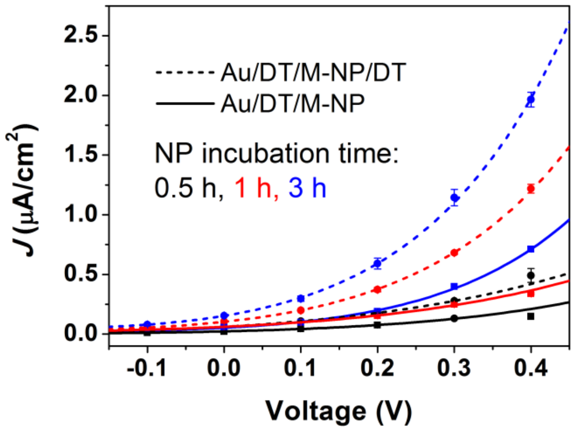

Figure A8. This figure shows photocurrent-voltage (*J*-V) characteristics of Au/DT/M-NP (solid lines, squares) and Au/DT/M-NP/DT (dashed lines, circles) for different NP incubation times (black is 0.5 h, red is 1 h, and blue is 3 h). Lines connecting points serve as a guide for the eyes. Most error bars are smaller than the symbol.

In Figure A9, the dark current density (black squares) for the assembly of Au/DT/M-NP and Au/DT/M-NP/DT was rescaled to have the same value. The change to the dark current density was also applied to the corresponding light-on current density. The red and blue squares are the light-on current density for the assembly of Au/DT/M-NP and Au/DT/M-NP/DT, respectively. The difference between the dark current density and the light-on current density is the photocurrent density, which is shown as the red and blue triangles. It is apparent that the photocurrent density is much smaller than the dark current density, because only a monolayer of the NP was attached to the electrode. This fact is also the reason why the difference in the light-on current density is so small between the Au/DT/M-NP and Au/DT/M-NP/DT.

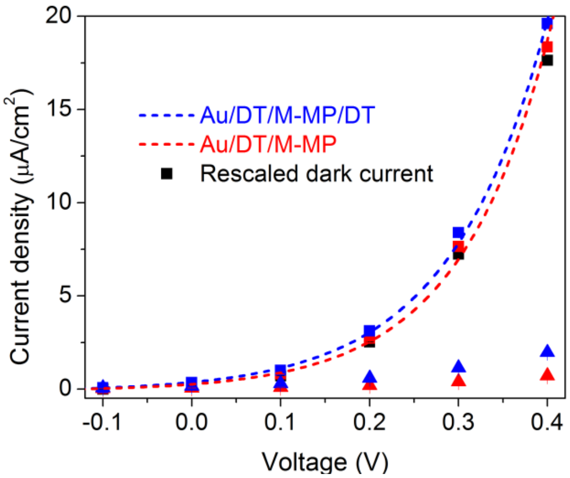

Figure A9. The black squares are the rescaled dark current density. The red and blue squares are the light-on current density for the assembly of Au/DT/M-NP and Au/DT/M-NP/DT, respectively. Two dash lines are the fitting to the corresponding light-on current density. The red and blue triangles are the photocurrent density for the assembly of Au/DT/M-NP and Au/DT/M-NP/DT.

In Figure A9, the *J*-*V* characteristics of the light-on current density for the two assemblies were fitted by a simple Schottky diode model (red and blue dash lines), namely:

$$J = J_o\,[\exp\left(\frac{qV}{nkT}\right) - 1] - J_L$$

in which,

$$J_o = A^{*}T^{2}\exp\left(\frac{-q\Delta\phi}{kT}\right)$$

and,

$$A^{*} = \frac{4\pi q m^{*} k^{2}}{h^{3}}$$

where, J_o is the saturation current density, n is the ideality factor, J_L is the photocurrent density, A^{*} is the Richardson constant, $\Delta\phi$ is the Schottky barrier height, $m^{*}$is the electron effective mass, T is the temperature, k is the Boltzmann constant, h is the Planck constant, and q is the elementary charge.

The fitting results are listed in Table A1. Based on the saturation current density (J_o) extracted from the fitting, the Schottky barrier height ($\Delta\phi$) for the two assemblies was calculated. The data show that ligand exchange from TDPA to DT slightly lowered the barrier height for electron transfer from the NP to the Au electrode. This fact may explain why the photocurrent of Au/DT/M-NP/DT is higher than that of Au/DT/M-NP. Note that the ideality factor (n) for the two assemblies is bigger than 2. This may be caused by the trap-state-assisted charge recombination in the assemblies, which has also been observed for several amorphous bulk semiconductors.

Table A1. The fitting results for Figure A9.

	$J_o(\mu A/cm^2)$	n	$J_L(\mu A/cm^2)$	$\Delta\phi\ (V)$
Au/DT/M-NP	0.376	3.99	-0.260	0.744
Au/DT/M-NP/DT	0.509	4.24	-0.368	0.736

The two equations generated by fitting the LUMO energy to a power law for the CdSe and CdTe NPs ,as shown in Figure 2.10. d (nm) is the diameter of the NPs.

For CdSe: $\mathrm{LUMO\ energy} = -3.80 + 1.34\mathrm{d}^{-1.11}$

For CdTe: $\mathrm{LUMO\ energy} = -3.50 + 11.16\mathrm{d}^{-2.89}$

APPENDIX B

Supporting information for Chapter 4

Synthesis of (-)PDPPPV. Poly(potassium 1,4-diketo-2,5-bis(4-sulfonylbutyl)-3,6-diphenyl-pyrrolo(3,4-c)pyrrole-alt-divinyl-1,4-bis(ethyloxy)benzene), denoted as (-)PDPPPV, was synthesized by Heck-coupling of monomer **(5)** with monomer **(9)**, as illustrated in Figure B1.

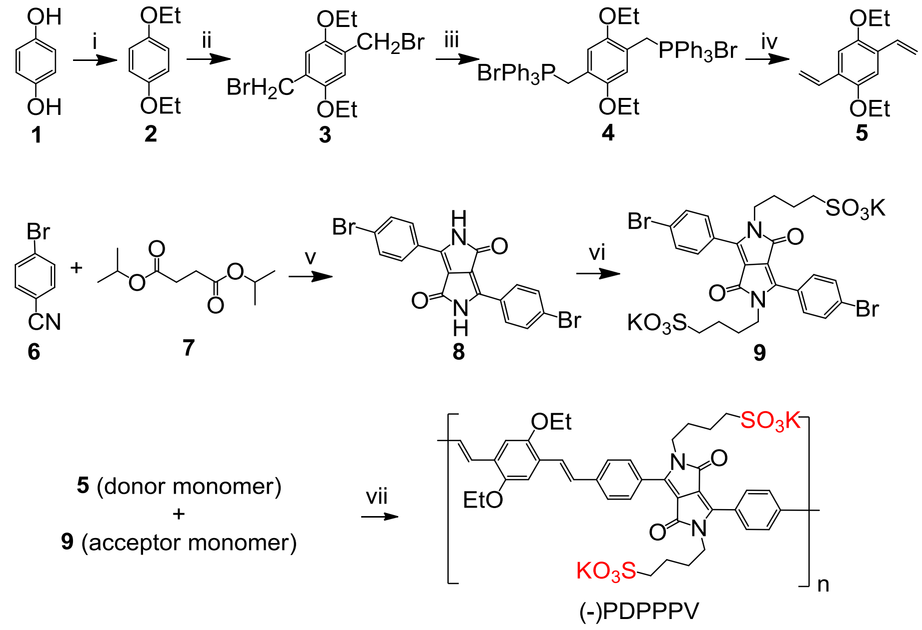

Figure B1. Synthetic route of (-)PDPPPV: (i) NaOH, DMSO, EtBr; (ii) NaBr, HOAc, H_2SO_4, $(CH_2O)n$; (iii)PPh_3, toluene; (iv) CH_2Cl_2, HCHO; (v) Na, tert-amylalcohol, $FeCl_3$, HOAc; (vi) t-BuOK, DMF, 1,4-butane sultone; (vii) P(o-tolyl)$_3$, Pd(OAc)$_2$, NEt_3, DMSO, H_2O.

Monomer 5. Under an argon atmosphere, compound **4** (2,5-diethoxy-1,4-xylylene-bis(triphenyl phosphonium bromide)) (6.5748 g, 7.5 mmol) was stirred at 0 °C in dichloromethane (100 mL) and formaldehyde (30 mL), to which a 25 mL aqueous solution of

NaOH (20 wt %) was added drop-wise over a time period of 1 h, and the reaction mixture was stirred for 24 h. Afterward phase separation was allowed to occur and the aqueous layer was extracted. The resultant non-aqueous layer was dried with anhydrous sodium sulfate, and then the solvent was removed by rotary evaporation. The residue obtained afterward was purified by recrystallization in ethanol to yield pale yellow crystal. Yield: 1.1526 g, 70.4 %. ^{1}H NMR ($CDCl_3$, 300 MHz): δ (ppm) 1.43 (t, $-CH_3$, 6H), 4.04 (q, $O-CH_2$, 4H), 5.26 (d, vinyl-H(terminal), 2H), 5.73 (d, vinyl-H(terminal), 2H), 7.00 (s, Ar-H, 2H), 7.00-7.10 (dd , vinyl-H, 2H). IR (KBr, cm^{-1}): 3088 (m, ν(=C-H)), 2978,2926 (vs, ν_{as}($-CH_3$, $-CH_2-$)), 2876 (vs, ν_s($-CH_3$, $-CH_2-$)), 1620-1474 (s, ν($Ar_{C=C}$)), 1391 (s, δ($-CH_3$)), 1271 (s, ν($-CH_3$)), 1205 (vs, ν(C-O)), 910 (s, γ(=C-H)).

Monomer 9. Under an argon atmosphere, compound **8** (4.46 g ,10 mmol) and potassium *t*-butoxide (1.76 g, 22 mmol) were heated at 60 °C in dry DMF (150 mL), and 1,4-butane sultone (3.1 mL, 30 mmol) was slowly added. The reaction mixture was stirred at 90 ^{o}C for 12 h, and then it was poured into ethanol (1L) to obtain a precipitate that was collected by filtration and redissolved in hot water. The resultant water solution was filtered, concentrated, and dried under vacuum to give an orange-red solid. Lastly the product was purified by recrystallization in an aqueous solution of potassium chloride (50g/L) and dried under vacuum at 120 ^{o}C for 24 h to obtain a red-brown powder. Yield: 1.55 g, 26 %. ^{1}H NMR (D_2O, 300 MHz): δ (ppm) 1.49 (m, 8H, methylene), 2.69 (t, $S-CH_2$, 4H), 3.67 (t, $N-CH_2$, 4H), 7.44 (d, DPP aromatic H, 4H), 7.60 (d, DPP aromatic H, 4H). IR (KBr, cm^{-1}): 2937 (vs, ν_{as}($-CH_3$, $-CH_2-$)), 2868 (vs, ν_s($-CH_3$, $-CH_2-$)), 1676 (s, ν(C=O)), 1605,1551 (s, ν($Ar_{C=C}$)), 1369 (vs, ν(C-N)), 1184,1045,1007 ($R-SO_3^-M^+$), 735 (w, δ($-(CH_2)_n-$)).

(-)PDPPPV. Under an argon atmosphere, monomer **5** (0.2183 g, 1 mmol), monomer **9** (0.7946 g, 1 mmol), palladium(II) acetate (0.0135 g, 0.06 mmol), tri(o-tolyl)phosphine (0.0730 g, 0.24 mmol), and triethylamine (5 mL) were placed in a three-neck round-bottom flask with H_2O (3 mL) and dimethylsulfoxide (8 mL). The reaction mixture was allowed to stir at 100 ^{o}C for 18 h and subsequently cooled and then filtered. The filtrate was poured into the mixed solvent (ethyl ether/acetone/methanol =5/4/1), after which a precipitate was formed and isolated by filtration. It was then re-dissolved in deionized water (10 mL). The resultant solution was dialyzed in deionized water for three days using a 4kD MWCO cellulose membrane (*Spectra/Por* Cellulose Ester Membrane). Finally the solvent was removed by rotary evaporation and the crude product was further dried under vacuum with P_2O_5 at 50 ^{o}C for 2 days to obtain a dark purple powder. Yield: 0.4126 g, 48.47%. ^{1}H NMR (D_2O, 300 MHz): δ (ppm) 1.37-1.47 (-CH_3 and -CH_2-), 2.59-2.75 (S-CH_2), 3.65 (N-CH_2), 3.96 (O-CH_2), 7.22-7.57 (vinyl-H and DPP aromatic H). IR (KBr, cm^{-1}): 3045 (m, ν(=C-H)), 2930(νs, ν_{as}(-CH_3, -CH_2-)), 2870 (νs, ν_s(-CH_3, -CH_2-)), 1664 (s, ν(C=O)), 1593,1541 (s, $\nu(Ar_{C=C})$), 1391 (s, δ(-CH_3)), 1367 (νs, ν(C-N)), 1186,1041 (R-$SO_3^-M^+$), 725 (w, $\delta(-(CH_2)_n-)$).

Synthesis of (+)PDPPPV. Poly(1,4-diketo-2,5-dipropyl-3,6-diphenyl-pyrrolo(3,4-c)pyrrole-alt-divinyl-1,4-bis(2-(N,N,N-triethylaminium)ethoxy)benzene bromide), namely, (+)PDPPPV, was synthesized by Heck-coupling of monomer **2** and monomer **8**, as shown in Figure B2. Note that the compound labels here should not be confused with those for (-)PDPPPV.

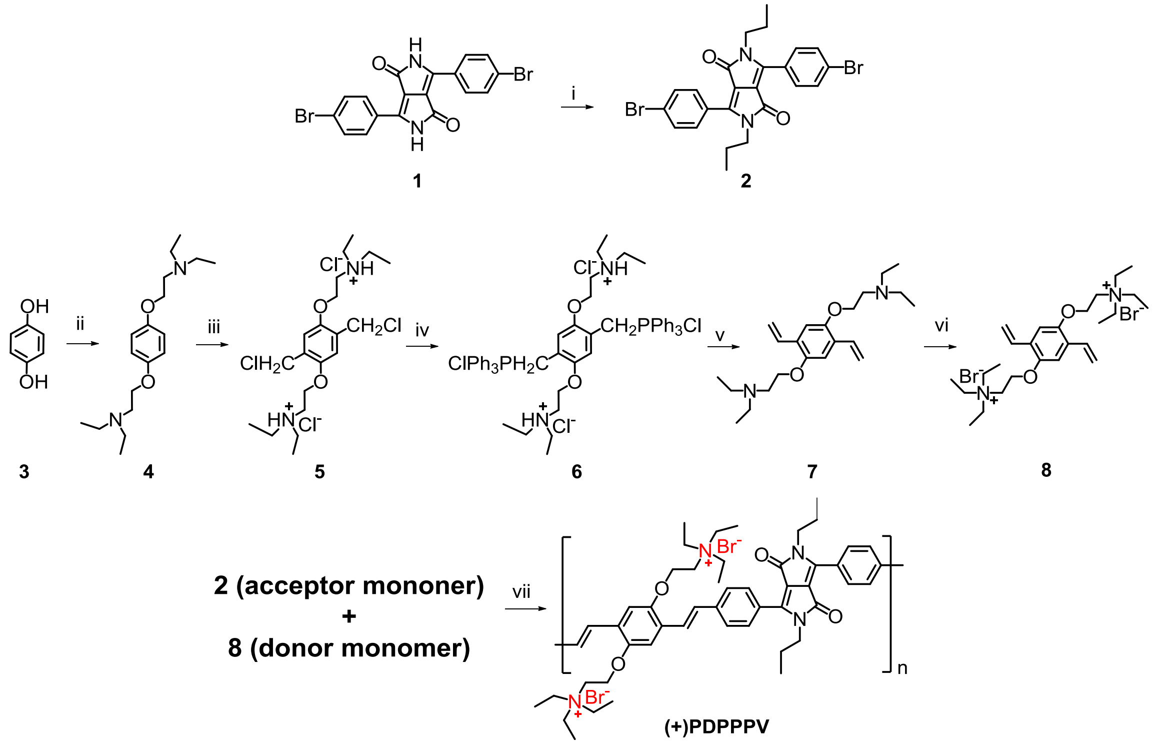

Figure B2. The synthesis for (+)PDPPPV. (i) t-BuOK, NMP, 1-iodopropane; (ii) K_2CO_3, acetone, 2-chlorotriethylamine hydrochloride; (iii) HCl, HCHO, dioxane; (iv) PPh_3, H_2O, DMF; (v) NaOH, HCHO; (vi) EtBr, acetone; (vii) P(o-tolyl)$_3$, Pd(OAc)$_2$, NEt_3, DMSO.

Monomer 2. Under an argon atmosphere, compound **1** (1,4-diketo-3,6-bis(4-bromophenyl)pyrrolo[3,4-c]pyrrole) (0.892 g, 2 mmol), potassium tert-butoxide (0.494 g, 4.4 mmol), and anhydrous 1-methyl-2-pyrrolidinone (15mL) were heated at 60 °C. 1-iodopropane (2.04g, 12mmol) was added slowly and the mixture was stirred at 60 °C for 24 h. After cooling to room temperature, 25 mL of toluene was added to the reaction mixture, which was then washed with water to remove the NMP. The solution was concentrated by using a rotary evaporator. The crude product was purified by column chromatography on silica using dichloromethane as the eluent, and the final product was an orange powder. Yield: 0.221 g, 21%. 1H NMR (400 MHz, CDCl3): δ (ppm) 7.72 – 7.64 (m, 8H), 3.74 – 3.67 (m, 4H), 1.59 (dd, J = 15.0, 7.5 Hz, 4H), 0.85 (t, J = 7.4 Hz, 6H).

Monomer 8. Under an argon atmosphere, compound **7** (1,4-Bis[N,N-diethylamino]-1-oxapropyl]- 2,5-divinyl-benzene benzene) (crude product, 2.095 g) , bromoethane (2 g), and acetone (10 mL) was stirred and heated for two days to obtain a white precipitate. The solid was filtered, washed with bromoethane and hot acetone repeatedly, and finally dried under vacuum to obtain a white powder. Yield: 714 mg, 43% (6→8, 2 steps total yield). 1H NMR (300 MHz, D2O): δ (ppm) 7.22 (s, 2H), 7.02 (dd, J = 17.7, 11.2 Hz, 2H), 5.85 (d, J = 17.7 Hz, 2H), 5.41 (d, J = 11.3 Hz, 2H), 4.53 – 4.43 (m, 4H), 3.81 – 3.72 (m, 4H), 3.46 (q, J = 7.2 Hz, 12H), 1.35 (t, J = 7.2 Hz, 18H).

(+)PDPPPV. Under an argon atmosphere, monomer **8** (115.7 mg, 0.2 mmol), monomer **2** (106 mg, 0.2 mmol), palladium(II) acetate (2.8 mg, 0.012 mmol), tri(o-tolyl)phosphine (14.6 mg, 0.048 mmol), and triethylamine (2 mL) were placed in a three-neck round-bottom flask with dimethylsulfoxide (8 mL). The reaction mixture was stirred at 80 ˚C for 6 h; then the mixture was poured into a mixed solvent (ethyl ether/acetone/methanol=5/4/1). A precipitate was formed and isolated by filtration. The crude product was dried under vacuum to obtain a dark purple powder. 1H NMR (400 MHz, DMSO-d6): δ (ppm) 7.96-7.36 (vinyl-H and phenyl-H), 4.60-4.50 (O-CH_2-), 3.89-3.47 (N-CH_2-), 1.48-1.31 (-CH_2-), 1.05-0.78 (-CH_3).

Molecular weight determination for PDPPPV copolymers. Table B1 shows the molecular weight results for the two PDPPPV copolymers determined by using gel permeation chromatography (GPC) and polyethylene oxides as a standard in either DI water or DMSO. The solvent was selected based on the polymer's solubility in order to reach a concentration required to obtain reasonable signal intensity and reproducible results. It has been reported that accurate determination of the molecular weight for these copolymers is problematic, because its self-aggregation leads to an overestimation of the molecular weight. For example, the (-)PDPPPV has a Mn of 25,700 and a Mw of 266,400. A high polydispersity index (Mw/Mn) suggests a large size distribution, which is likely caused by the polymer self-aggregation. Note that the GPC measurements required a relatively high polymer concentration (~ 1 mg/ml), which is about 300 times higher than that used in the spectroscopic measurements. Figure B4A shows absorbance spectra for these two copolymers and does not indicate features of aggregation. Thus, the self-aggregation does not pose a serious problem for the charge transfer studies at low concentrations in solution.

Table B1. The GPC results for the molecular weight of the two PDPPPV copolymers.

Polymer	**M_w**	**M_n**	**PDI (M_w/M_n)**	**Solvent**
(-)PDPPPV	266,400	25,700	10.4	0.1 M Na_2SO_4 aqueous solution at 30 ˚C
(+)PDPPPV	58,500	24,200	2.4	DMSO at 80 ˚C

Synthesis of anionic and cationic CdTe nanoparticles. CdTe nanoparticles (NPs) (~ 5 nm in diameter, see Figure B3) were originally synthesized in octadecene at 280 ˚C by the hot-injection method with oleic acid (OA) as the capping ligand. The OA-CdTe NPs were ligand-exchanged in an aqueous solution of $CdCl_2$/2-(dimethylamino) ethanethiol hydrochloride (DEA) to obtain water-soluble, highly fluorescent, and cationic DEA-CdTe NPs ((+)NPs). Anionic CdTe NPs ((-)NPs) were prepared by using 3-mercaptopropionic acid (MPA) in the ligand exchange, instead of DEA. MPA-CdTe and DEA-CdTe NPs have very similar absorption spectra with that of the parent OA-CdTe NPs, as shown in Figure B4B.

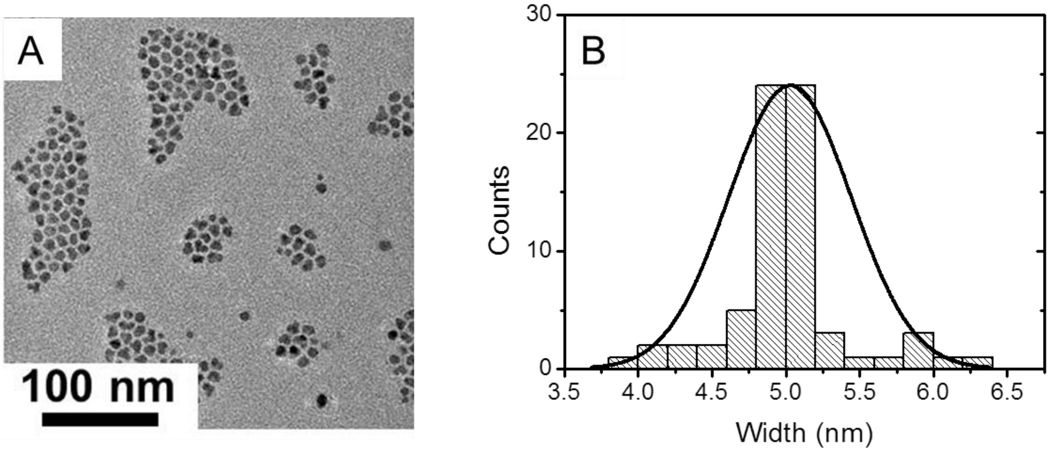

Figure B3. Panel A shows a TEM image for the OA-CdTe NPs used in this study. Panel B shows the size distribution for the OA-NPs obtained by using Image J software to analyze more than 60 NPs.

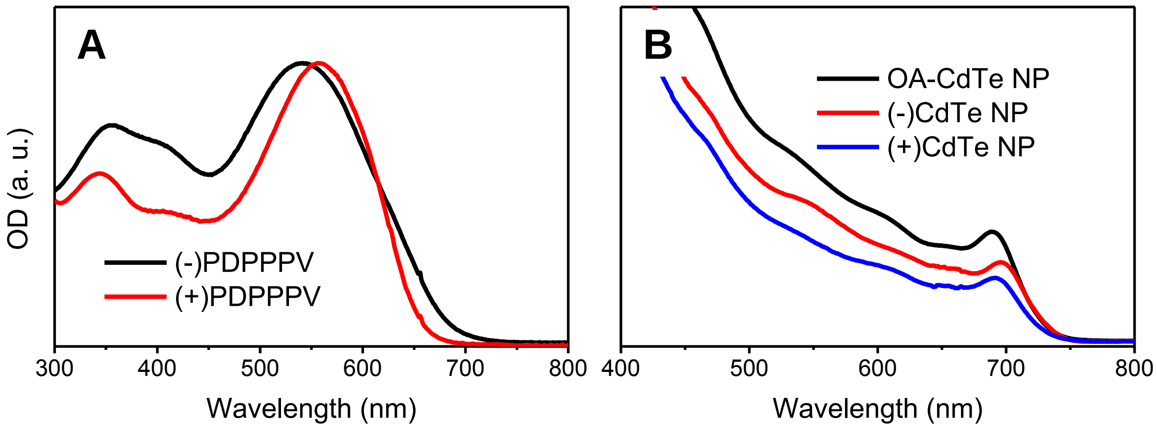

Figure B4. Panel A compares the steady-state absorption spectra for (-)PDPPPV and (+)PDPPPV. Panel B compares the steady-state absorption spectra for the parent OA-CdTe NPs and (-)/(+) CdTe NPs.

Cyclic Voltammetry. A three-electrode electrochemical cell was used to determine the energetics of the NPs and polymers. Films of the NPs and polymers were drop-cast from their aqueous solution onto a glassy carbon electrode. The electrochemical cell also included a Pt counter electrode and a Ag/AgNO$_3$ reference electrode (0.1 V vs. Fc/Fc$^+$), to which the potential is referenced. The electrolytes were an acetonitrile solution with 0.1 M tetrabutylammonium hexafluorophosphate (TBAPF$_6$).

Because the oxidation onset can be directly related to the charge transfer with the valence band edge, cyclic voltammetry (CV) was used to determine the band edge position for the CdTe NPs and PDPPPV copolymers. Figure B5 shows the CV results for (+)/(-) PDPPPV copolymers, (+)/(-) CdTe NPs, and a control polymer, poly[5-methoxy-2-(3-sulfopropoxy)-1,4-phenylenevinylene] (denoted as (-)PPV). As described previously,[18] the onset oxidation potentials can be used to place the valence band edges for these materials and they are found to be at -5.50 ± 0.1 eV for CdTe NPs, -5.10 ± 0.1 eV for PDPPPV copolymers, and -5.60 ± 0.1 eV for (-)PPV. Errors were determined from the standard deviation of the data obtained from three separated measurements. If one uses their optical bandgap calculated from the absorption spectrum and the electrochemical valence band edge value to estimate the conduction band edge, then we obtain the energy level diagram shown in Figure 5D. This energy level predicts that 1) a type-II (donor-acceptor) heterojunction is formed between the PDPPPV copolymers and CdTe NPs; and 2) a type-I heterojunction is formed between the (-)PPV and CdTe NPs.

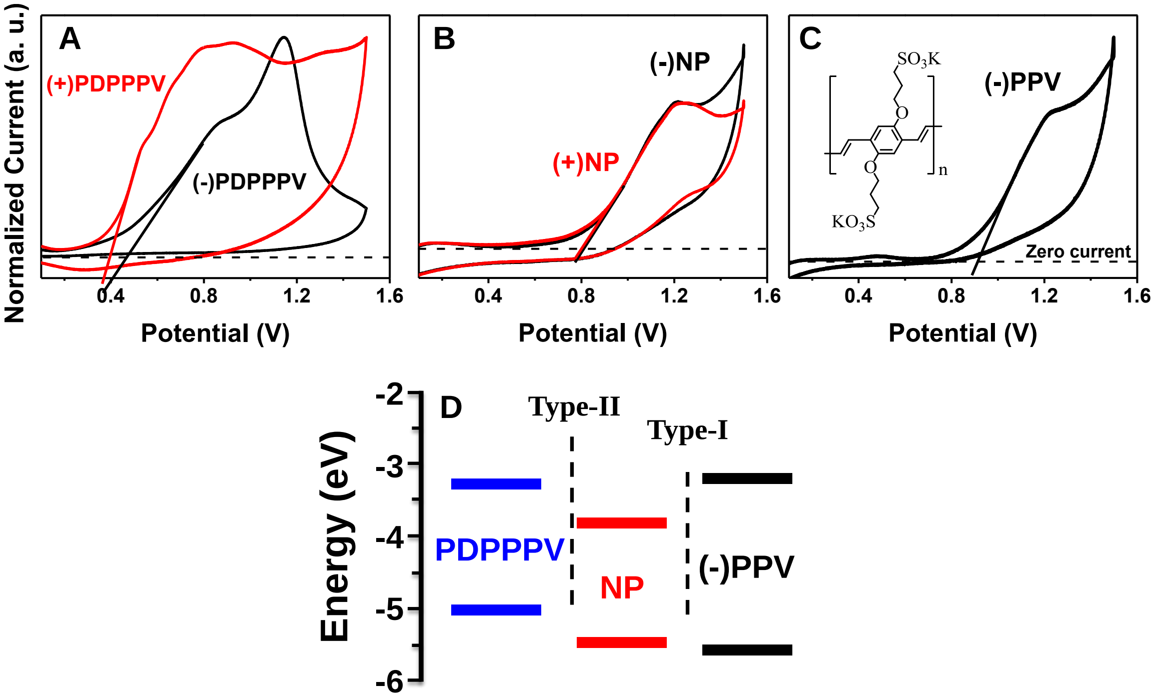

Figure B5. Panels A to C show cyclic voltammograms for (+)/(-) PDPPPV copolymers, (+)/(-) CdTe NPs, and (-)PPV. The background from the electrolytes has been subtracted from all voltammograms shown here. The dashed line marks the position of zero current in each panel. The crossing point between the zero current and onset tangent gives the oxidation onset potential. Panel D shows an energy diagram with the final CV results for all samples.

Dynamic light scattering (DLS) and Zeta-potential measurements. DLS measurements were performed on solutions of the NP/polymer assemblies at room temperature in a 90° geometry and analyzed by using particle sizing software with a 532 nm laser (Brookhaven Instrument Co.). Zeta-potential measurement were performed on the same instrument at room temperature with an electrical field strength of 10 V/cm by using a Zeta Plus potential analyzer.

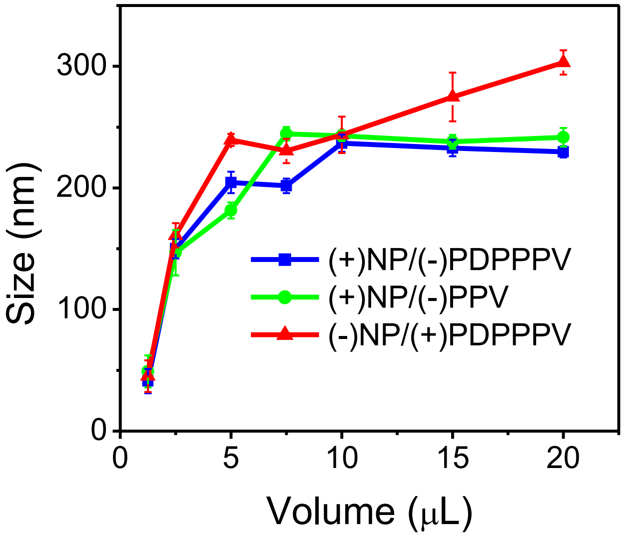

Figure B6. The aggregation size measured by dynamic light scattering for the three CP/NP combinations.

Table B2. Zeta-potential values for the polymers and NPs involved in this study.

Polymers	Zeta-potential (mV)	NPs	Zeta-potential (mV)
(-)PDPPPV	-36.24 ± 1.34	(-)NP	-24.59 ± 2.92
(+)PDPPPV	36.91± 2.31	(+)NP	20.45 ± 3.28
(-)PPV	-27.81 ± 1.22		

PL quenching. Steady-state absorption and emission spectra were measured by an Agilent 8453 spectrometer and a Horiba J-Y Fluoromax 3 fluorescence spectrophotometer. Steady-state photoluminescence quenching measurements were carried out while continuously adding 0.05 wt% aqueous polymer solution (20 μL in total) into a 3 mL NP phosphate buffer solution (pH=7). The optical density (OD) is ~ 0.1 for both NP and PDPPPV at their absorption peaks after titration, which corresponds to a NP/polymer molar ratio of 3 to 1.

The time-resolved fluorescence data were collected using the time-correlated single photon counting (TCSPC) method. The instrument response function was measured using a sample of colloidal $BaSO_4$. The samples were excited at 660 nm using a dye laser (DCM) at a 1 MHz repetition rate, and fluorescence counts were collected until 6000 counts in the peak channel for each sample. Experiments were also performed with a 300 kHz repetition rate, at which the lifetime values were found to be nearly identical to those collected at a 1 MHz repetition rate in all the systems studied. The kinetics were extracted by fitting the fluorescence decay curves by using a FAST lifetime distribution software.

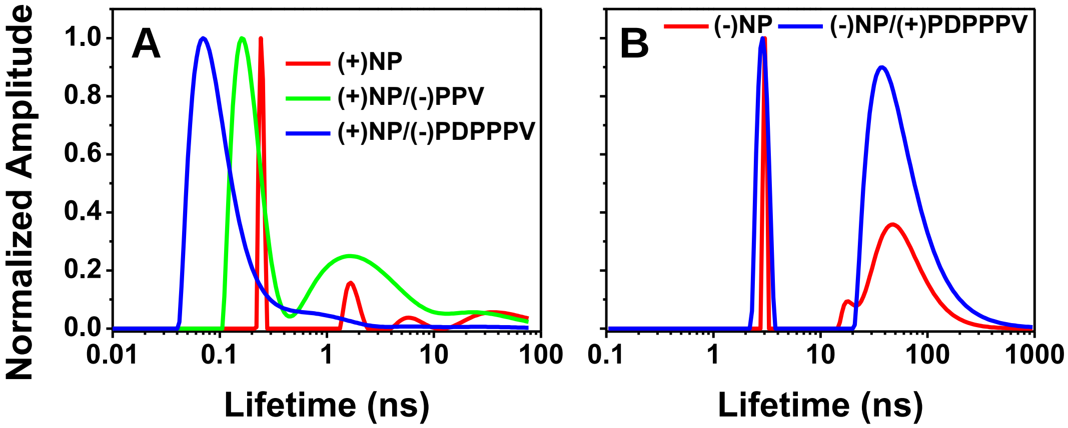

Figure B7. Lifetime distribution fitting for the PL decays shows in Figure 3D and Figure 5B.

Ultrafast Transient absorption spectroscopy. Ultrafast transient absorption spectroscopy measurements were carried out in Notre Dame Radiation Lab by using a Clark-MXR 2010 Ti:sapphire laser system (775 nm, 1 mJ pulse^{-1}, full width at half maximum of 130 fs, and 1 kHz repetition rate) equipped with a CCD spectrograph (Ocean Optics, S2000-U-UVvis). Five percent of the fundamental was used to generate a probe pulse, while 95% of the laser beam was utilized by a second harmonic generator to produce a pump laser pulse (387 nm).

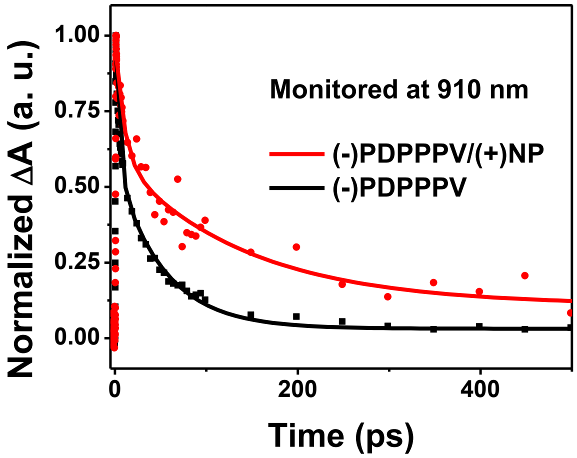

Figure B8. This figure compares the fitted kinetic traces monitored at 910 nm for the (-)PDPPPV-only and (-)PDPPPV/(+)NP samples.

Spectroelectrochemistry. The measurement was performed with a drop-cast (-)PDPPPV thin film on an ITO working electrode in a three-electrode spectroelectrochemical cell that has a Au wire counter electrode and a Ag/Ag^+ reference electrode. The voltage was applied by a CHI 618B potentiostat, and the spectra were collected on an Agilent 8453 spectrometer.

APPENDIX C

Supporting information for Chapter 5

Figure C1 shows the voltammetry result for the PbS QDs whose optical band gap is 1.67 eV and 1.32 eV, respectively. The oxidation onset of the CV curve gives the valence band edge of the PbS QDs. The absolute energy for the reference electrode (Ag/$AgNO_3$) was measured as 4.7 eV. Thus, the valence band edge energy of the QDs is calculated by adding 4.7 eV to the oxidation onset energy. In addition, the conduction band edge is determined by a sum of the valence band edge energy and the optical band gap.

The dashed lines in the CV curves show that the oxidation onset of QD (Eg = 1.67 eV) is 0.50 eV, and that of QD (Eg = 1.32 eV) is 0.33 eV. As a result, the valence band edge is -5.20 eV for smaller PbS QDs and -5.03 eV for bigger PbS QDs, and the subsequent conduction band edge is -3.5 eV and -3.7 eV, separately.

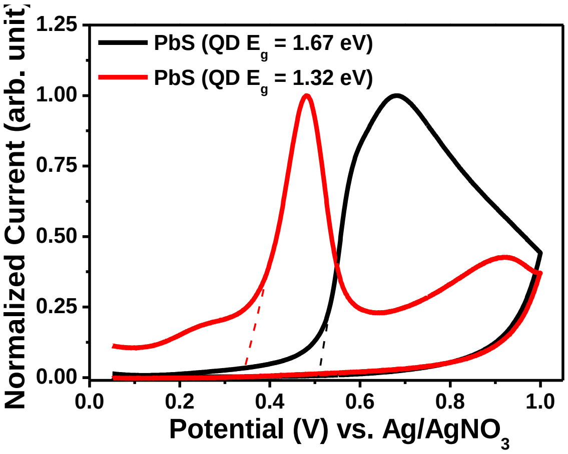

Figure C1. Cyclic voltammogram results for PbS QDs with an optical band gap of 1.67 eV and 1.32 eV, separately.

Figure C2 reveals the large scale TEM and HRTEM images of bigger PbS QDs, whose optical band gap is 1.32 eV. From the large scale TEM, the size distribution of the QDs is counted as 3.6 ± 0.3 nm.

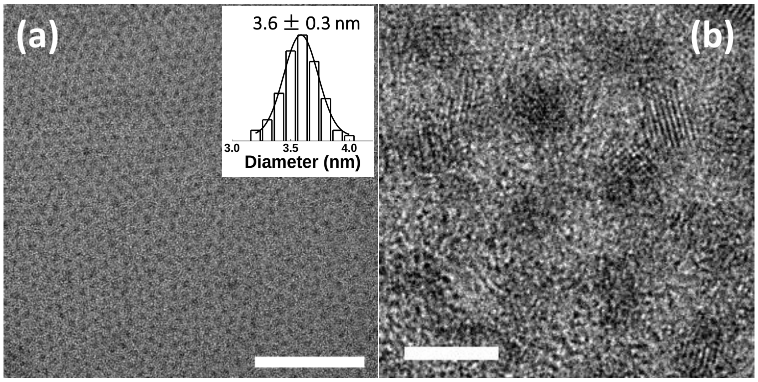

Figure C2. (a) Large scale TEM and (b) HRTEM images of PbS QDs (E_g = 1.32 eV) on a Cu grid. The insert scale bar in (a) is 50 nm and (b) is 5 nm.

Figure C3 shows the PbS film deposited on silicon substrate via a layer-by-layer dipping method. In each dipping cycle, the fresh layer was merged into EDT/acetonitrile solution for ligand exchange. Typically, after a fourteen cycle deposition, the thickness of the PbS film is around 200 nm.

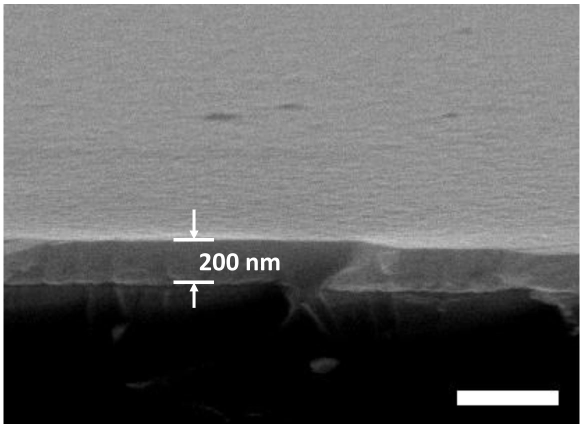

Figure C3. PbS QDs film deposited on silicon substrate via a layer-by-layer dipping method. The thickness of the film is around 200 nm. Insert scale bar is 500 nm.

Figure C4 shows the equivalent circuit of the solar device, in which a current source, a diode and a shunt resistance (R_{SH}) are connected in parallel. In addition, another series resistance (R_S) is added to the circuit as well. The direction of each current flow is drawn in the circuit. Finite value of R_{SH} reveals a presence of the current leakage and higher value of R_S corresponds to a reduction of charge mobility in the device.

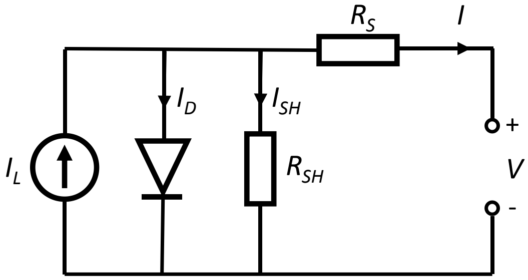

Figure C4. The equivalent circuit of the solar device.

The EDS mapping of the unannealed sample is shown in Figure C5. The distribution of S and Ti at the TiO_2/PbS interface clearly shows that no PbS QDs diffuse into the TiO_2 mesoporous layer, and only a plain heterojunction is built at the TiO_2/PbS interface.

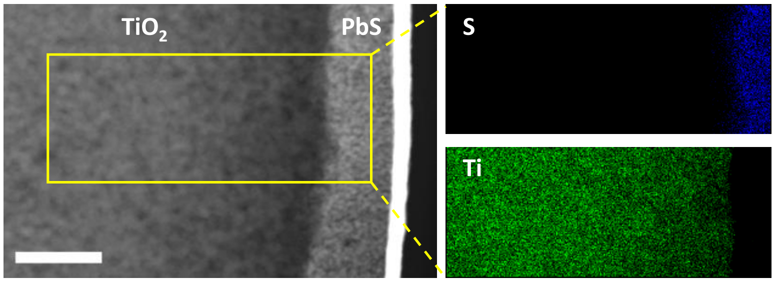

Figure C5. HADDF image and EDS mapping of unannealed sample. The insert scale bar is 200 nm.

Figure C6 shows that the device using bigger QDs (E_g = 1.32 eV) has a lower carrier lifetime (τ) than the device using smaller QDs. After annealing the PbS film with E_g of 1.32 eV at 150 °C for 10 min in Ar gas, τ is reduced. A decrease in τ by the thermal annealing is also observed in the device using smaller PbS QDs (E_g = 1.67 eV).

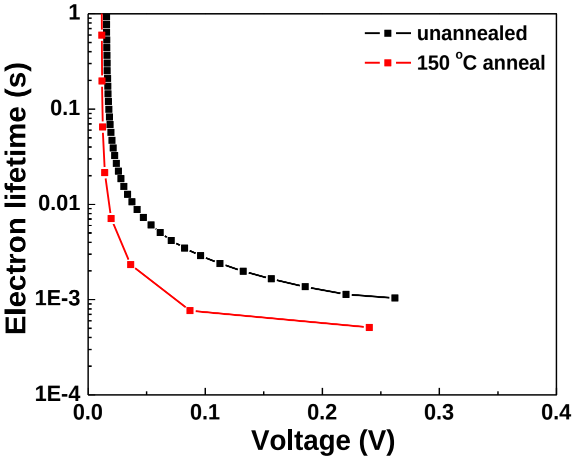

Figure C6. Electron lifetime of the devices using PbS films (QD E_g = 1.32 eV) with and without annealing.

APPENDIX D

Publication list of the thesis author

(1) Wang, Y.; Liu, K.; Mukherjee, P.; Hines, D. A.; Santra, P.; Shen, H. Y.; Kamat, P.; Waldeck, D. H., Driving charge separation for hybrid solar cells: photo-induced hole transfer in conjugated copolymer and semiconductor nanoparticle assemblies. *Physical Chemistry Chemical Physics* **2014,** 16 (11), 5066-5070

(2) Bloom, B. P.; Zhao, L.-B.; Wang, Y.; Waldeck, D. H.; Liu, R.; Zhang, P.; Beratan, D. N., Ligand-Induced Changes in the Characteristic Size-Dependent Electronic Energies of CdSe Nanocrystals. *The Journal of Physical Chemistry C* **2013,** 117 (43), 22401–22411.

(3) Song, C.; Wang, Y.; Rosi, N. L., Peptide-Directed Synthesis and Assembly of Hollow Spherical CoPt Nanoparticle Superstructures. *Angewandte Chemie International Edition* **2013**, 52 (14), 3993-3995.

(4) Wang, Y.; Wang, L.; Waldeck, D. H., Electrochemically Guided Photovoltaic Devices: A Photocurrent Study of the Charge Transfer Directionality between CdTe and CdSe Nanoparticles. *Journal of Physical Chemistry C* **2011**, 115 (37), 18136-18141.

(5) Wang, Y.; Xie, Z.; Gotesman, G.; Wang, L.; Bloom, B. P.; Markus, T. Z.; Oron, D.; Naaman, R.; Waldeck, D. H., Determination of the Electronic Energetics of CdTe Nanoparticle Assemblies on Au Electrodes by Photoemission, Electrochemical, and Photocurrent Studies. *The Journal of Physical Chemistry C* **2012**, 116 (33), 17464-17472.

(6) Yang, D.; Wang, Y.; Zhang, D.; Liu, Y.; Jiang, X., Control of the morphology of micro/nanostructures of polycarbonate via electrospinning. *Chin. Sci. Bull.* **2009**, 54 (17), 2911-2917

(7) Yang, D. Y.; Niu, X.; Liu, Y. Y.; Wang, Y.; Gu, X.; Song, L. S.; Zhao, R.; Ma, L. Y.; Shao, Y. M.; Jiang, X. Y., Electrospun Nanofibrous Membranes: A Novel Solid Substrate for Microfluidic Immunoassays for HIV. *Advanced Materials* **2008**, 20 (24), 4770